Superparamagnetic iron oxide nanoparticles for imaging and drug delivery

Inauguraldissertation

zur

Erlangung der Würde eines Doktors der Philosophie

vorgelegt der

Philosophisch-Naturwissenschaftlichen Fakultät

der Universität Basel

von

Emre Çörek

Basel, 2020

Genehmigt von der Philosophisch-Naturwissenschaftlichen Fakultät
auf Antrag von

Prof. Dr. Jörg Huwyler (Erstbetreuer)
Prof. Dr. Alex Odermatt (Zweitbetreuer)
Prof. Dr. Gert Fricker (Externer Experte)

Basel, den 21. April 2020

Prof. Dr. Martin Spiess (Dekan)

"Mankind's enemy is ignorance; the enemy of ignorance is education."

"Science is the most reliable guide in life."

-Mustafa Kemal ATATÜRK

CHAPTER 1: SUMMARY

In the past years, nanoparticle usage and research increased enormously in different fields, especially in the clinical sciences for drug delivery and imaging. Selection of the most suitable type of nanoparticle is not always easy because of a broad material variety and different physicochemical characteristics. Depending on the purpose, the safe usage of nanoparticles *in vivo* needs to be ensured first to predict and eliminate unwanted effects like agglomeration, loss of function, immune system responses (i.e. inflammation), or toxicity after intravenous application. To guarantee the safe usage of nanoparticles, there are various hazard evaluation strategies for different scenarios for example for nanomedicines. Drug delivery with nanomedicines has advantages like increased absorbability, increased *in vivo* half-life, and decreased drug dosage needs to reach the same therapeutic effect. Amongst others, superparamagnetic iron oxide nanoparticles (SPIONs) and liposomes are already used as medicinal nanoparticles and are approved from the US Food and Drug Administration (FDA). Examples are Feraheme®, which is a ferumoxytol injection for iron deficiency treatments and Doxil®, a liposomal doxorubicin hydrochloride chemotherapy drug. SPIONs are also used as contrast agents because of their high-dense core and the possibility to synthesize very small diameters below 10 nm, which can even penetrate into smallest fenestrations of i.e. the kidneys. This work is divided into two main parts:

Part one was the analysis of different nanoparticle safety evaluation strategies to propose a new hazard evaluation guideline for intravenously applied nanoparticles. This was part of the NanoREG II European Union's Horizon 2020 research and innovation program under grant agreement 646221.

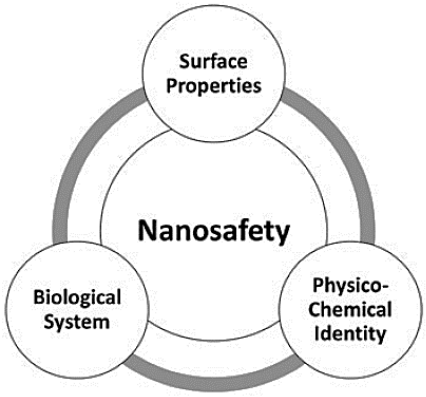

Part two started with the synthesis and physicochemical characterization of hybrid nanoparticles made out of SPION cores and liposome coatings. The coatings were differently modified with additions like polyethyleneglycol for increased *in vivo* half-life or folic acid for renal targeting. Injected into zebrafish *(Danio rerio)* embryos, their biodistribution and toxicity was analyzed. Various methods like confocal laser scanning microscopy and synchrotron X-ray radiation micro-computed phase-contrast tomography were used and compared with each other. Finally, those hybrid nanoparticles were manipulated *in vivo* with external magnets to increase phagocytic uptake and also with electromagnetic fields and acoustic waves for controlling the nanoparticles *in vivo* in terms of agglomeration and rotation.

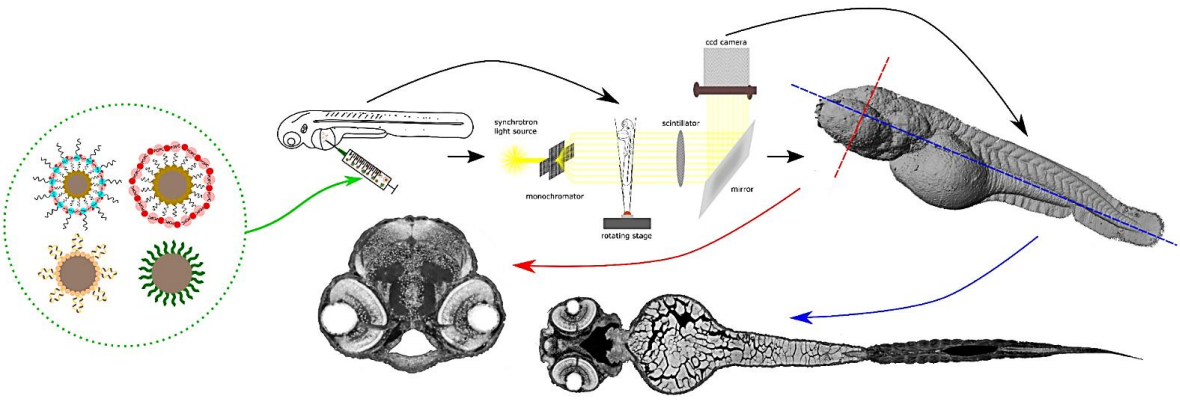

CHAPTER 2: INTRODUCTION

I. NANOMATERIALS

The history of nanoscience started in the 19th century with Michael Faraday[1]. He was investigating the optical properties of gold and silver colloids and found out in 1857, that there is a size-dependent color change of “colloidal ruby gold”. The particle solutions were changing their color depending on their size or shell thickness. This phenomenon was already used since the 4th century by Romans to make dichroic glass[2]. It continued in the 9th century with lustre pottery, ceramic glazes containing copper, silver and other nanoparticles firstly used by the Islamic world in Mesopotamia[3]. Also European cathedrals made use of vibrant stained glass windows in the 10th century, containing gold chloride and other metal oxides and chlorides for coloring[4].

The breakthrough in visualization of those nanoparticles was the invention of the first transmission electron microscope in 1931[5]. With this development, it was possible to magnify structures up to one million times compared to up to 2000 times with a light microscope and herewith the possibility to see nanostructures and even atoms was given[6].

DESCRIPTION OF NANOMATERIALS

Nanoparticles are not only man-made but did exist in nature already (Figure 1)[7]. As a first group, natural nanoparticles consist of different materials such as small molecular breakdown products (i.e. humic matter), organic compounds and (oxyhydr)oxides generated during the chemical and physical decomposition of rocks containing iron (Fe), manganese (Mn) and aluminum (Al) and aluminosilicates[8]. Also

dust storms[9], volcanic eruptions[10], forest fires[11], and ocean water evaporation[12] are generating enormous amounts of naturally occurring nanoparticles like carbon black and salt aerosols[13]. The second group are the engineered nanoparticles. A lot is produced during the daily live by transportation (diesel and engine exhaust)[14], industrial operations, and charcoal burning. Also cigarette smoke[15] and building demolition[16] can lead to nanoparticle production like carbon nanotubes (CNTs), lead, glass, and respirable asbestos fibers[13]. Biomedical and healthcare products also contain synthetic nanoparticles made of titanium dioxide in sunscreens[17] or silver nanoparticles in deodorants and food storage containers[18]. As a third group, nanostructures are also present as biological organisms like viruses, nanobacteria, algae, fungi, yeast, and bacterial spores[13].

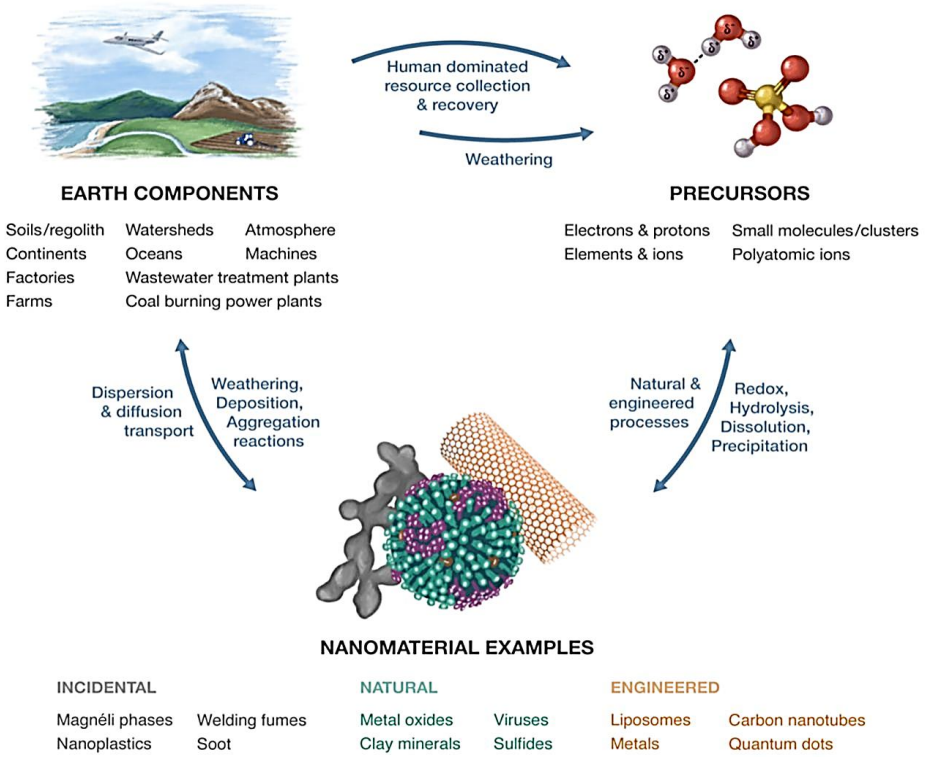

Figure 1 - Overview of nanomaterials and their cycle. Production is either naturally or man-made and is reversible between the groups of earth components, precursors, and nanomaterial examples (changed from[19]).

DEFINITION OF NANOPARTICLES (SUMMARIZED FROM THE ISO DEFINITION[20])

Nano-objects are defined by the International Organization of Standardization (ISO) as “objects with one or more external dimensions in the nanoscale, (…) which covers a length range approximately from 1 nm to 100 nm”. Those nano-objects are divided into three main groups, the nanoparticles (3 external dimensions in the nanoscale), nanofibers (2 external dimensions in the nanoscale), and nanoplates (1 external dimension in the nanoscale). Also, the term “primary-particle” is used to define the original source particle which can build agglomerates (“collection of weakly or medium strongly bound particles where the resulting external surface area is similar to the sum of the surface areas of the individual components”) or aggregates (“particle comprising strongly bonded or fused particles where the resulting external surface area is significantly smaller than the sum of surface areas of the individual components”).

TYPES OF NANOPARTICLES

Depending on their size, shape, material, and physicochemical properties, nanoparticles are classified into different groups. Those are carbon-based nanoparticles including fullerenes and carbon nanotubes, metal nanoparticles made out of alkali or noble metals like rubidium oxide or gold, ceramics nanoparticles which are non-metallic and inorganic, semiconductor nanoparticles with metallic and non-metallic characteristics at the same time, organic and capsule- or sphere-shaped polymeric nanoparticles, spherical lipid-based nanoparticles with a typical size range between 10 to 100 nm, quantum dots made out of nanocrystals of semiconducting materials, and nanocarriers which can be used as e.g. drug carriers. Also, all types of hybrids of those nanoparticles exist[21–23]. In this work, we will focus on nanoparticles

used in clinical sciences, especially SPIONs, liposomes, and their hybrid nanoparticles for drug delivery, targeting and imaging.

METAL NANOPARTICLES

Metal nanoparticles consist of a dense metal core and are typically spherical. They can be made of alkali or noble metal(oxide)s. One example are SPIONs with a broad application field and are produced by e.g. liquid phase methods or thermal decomposition, both of them allowing precise size control and result in narrow size distributions[24,25]. One of the first and easiest methods to produce iron oxide nanoparticles is the co-precipitation. It is the reduction of iron 2^+ and 3^+ oxide salts in an alkaline environment with help of stabilizing agents like citric acid, which was already described in the 80s[26,27]. These SPIONs can then be further modified i.e. by coating them with oleic acid to introduce hydrophobic characteristics for further usage in organic solvents like ethanol or chloroform[28]. In medicine, they are interesting because of their properties such as superparamagnetism and high field irreversibility, that allows to agglomerate the SPIONs in specific regions by an external magnetic field i.e. for targeting. After the field is removed, the SPIONs no longer show magnetic behavior[29]. The combination of external magnetic fields and magnetic drug delivery agents was first mentioned in the 1970s by Freeman et al.[30]. Since then, they are also used as contrast agents for visualization of labelled cells by magnetic resonance imaging (MRI)[31], targeting and contrast enhancement of breast cancer[32], and simultaneous imaging and chemotherapy (theranostics)[33]. They can also be used medicinal i.e. as SPIONs capped with vitamin C for oral treatment of iron deficiency anemia to increase the hemoglobin concentration effectively[34] or for intravenous anemia treatment of chronic kidney disease (CKD) with ferumoxytol (Table 1)[35–37].

Table 1 – Clinically approved SPIONs by the US Food and Drug Administration (FDA) with names, material and functionality, application and indication, and the approval date (copied from[38])

Name	Material/functionality	Application/indication	Approval date
Feridex I.V.®; Endorem®	Iron oxide nanoparticles (coated with dextran) Magnetic-field responsive for MRI imaging	Imaging of liver lesions	FDA approved (1996). Discontinued (2008)
Resovist®; Cliavist	Iron oxide nanoparticles (coated with carboxydextran) Magnetic-field responsive for MRI imaging	Imaging of liver lesions	EMA approved (2001). Discontinued (2009)
Gastromark™; Lumirem®	Iron oxide nanoparticles (coated with silicone) Magnetic-field responsive nanoparticles for MRI imaging	Enhance bowel imaging (oral administration)	FDA approved (1996). Discontinued (2012)
Ferumoxtran-10; Combidex®; Sinerem®	Iron oxide nanoparticles (coated with dextram) Magnetic-field responsive for MRI imaging	Lymph node metastases imaging	Approved in some European countries. Application withdrawn from EMA (Sinerem 2007). Application withdrawn from FDA (2005)
Ferahcme®; Ricnso®; Ferumoxytol	Iron oxide nanoparticles (coated with polyglucose sorbitol carboxymethylether)	Treatment of iron deficiency in adults with chronic kidney disease	FDA approved (2009)

LIPID NANOPARTICLES

Lipid nanoparticles have the advantage to be the least toxic of all nanoparticles *in vivo* and are used for DNA/RNA or drug delivery by encapsulation[39]. Field of applications are i.e. immunotherapy in cancer treatment for antitumor immune response[40], neurological disorders like Parkinson's disease (PD) or multiple sclerosis (MS)[41], or even for non-invasive brain targeting by by-passing the blood-brain barrier (BBB)(Table 2)[42]. One of the first liposome-encapsulated drug formulations containing Doxorubicin was already mentioned in the 80s for cancer treatment with lesser side effects than the administered free drug which is also known as Adriamycin due to the discovery at the Adriatic Sea[43,44]. It was the first clinically approved drug by the US Food and Drug Administration (FDA) named Doxil® in 1995[45]. Advantages of liposome-encapsulated Doxorubicin are i.e. increased half-life in blood circulation, protection from the reticuloendothelial system (RES) by pegylation, higher loading capacities, and passive targeting of the tumors by the enhanced permeability and retention (EPR) effect[45]. Liposomes are drug-loaded by transmembrane gradients,

so called remote loading, which enabled production of liposomal formulations like Doxil®. It enables the possibility to have enough liposomal drug-loads for therapeutic effects[46]. Liposomes with a typical average size of 100 nm contain an aqueous core and an outer lipid shell consisting of phospholipids, ideal for hydrophilic drug loading with i.e. paclitaxel, cisplatin or doxorubicin while hydrophobic drugs are entrapped in the outer lipid bilayer shell[47]. Synthesis of liposomes can be done with different techniques like the microfluidic hydrodynamic focusing (MHF) approach, in which the lipids and hydrophobic substances are dissolved in an organic solvent (i.e. alcohol) and the hydrophilic substances in water or phosphate-buffered saline (PBS)[48]. In a Y-shaped mixing chamber (i.e. with the automated mixing platform NanoAssemblr™), those two phases are mixed together and because of the "self-assembly", liposomes are formed[49]. During this process, the size, polydispersity index (PDI) and transfection efficiency of the liposomes can be reproducibly controlled with the total flow rate (TFR) and the flow rate ratio (FRR) between the two phases[49,50].

Table 2 – Liposomal formulations which are either under clinical evaluation or already on the market (changed from[51])

Product	Formulation	Application	Company	Status
AmBisome®	Liposomal amphotericin B	Fungal infections	Astellas Pharma/Gilead Sciences	Marketed
Abelcet®	Lipidic amphotericin B	Fungal infections	Sigma-Tau Pharmaceuticals	Marketed
Doxil®/ Caelyx®	PEGylated liposomal doxorubicin	Kaposi's sarcoma; metastatic breast & ovarian cancers	Janssen Pharmaceuticals	Marketed
DaunoXome®	Liposomal daunorubicin	HIV-associated Kaposi's sarcoma	Galen Ltd.	Marketed
DepoCyt®	Liposomal cytarabine	Lymphomatous meningitis	Sigma-Tau Pharmaceuticals	Marketed
DepoDur®	Liposomal morphine	Pain treatment	Pacira Pharmaceuticals	Marketed
Myocet®	Liposomal doxorubicin	Metastatic breast cancer	Cephalon Inc. (EU)/ Sopherion Therapeutics (US, CAN)	Marketed (EU)
Visudyne®	Liposomal verteporfin	Age-related macular degeneration (AMD)	Novartis AG/ QLT Inc. (US)	Marketed
ARIKACE®	Inhaled liposomal amikacin	*Pseudomonas* lung infections in cystic fibrosis	Insmed Inc.	Phase 3 (EU, CAN)
MM-398 (PEP02)	Liposomal irinotecan	Metastatic pancreatic cancer	Merrimack Pharmaceuticals, Inc.	Phase 3 NCT01494506*
ThermoDox®	Heat-sensitive liposomal doxorubicin	Primary liver cancer	Celsion Corp.	Phase 3 NCT00617981*

*ClinicalTrials.com identifier

COMBINATION OF METAL AND LIPID NANOPARTICLES (HYBRID NANOPARTICLES)

For increasing application possibilities and combining multiple properties, different types of nanoparticles can be combined to so called “hybrid nanoparticles” (Figure 2)[52]. One example is a combination between metal dense-core nanoparticles (i.e. SPIONs) within a phospholipid outer shell/coating (liposomes). They are able to transport hydrophilic or hydrophobic drugs and have at the same time the possibility to be magnetically manipulated i.e. for targeting or imaging *in vivo*[53–55]. It is possible to induce hyperthermia at the target location by an alternating current (AC) magnetic field (AMF) to locally destroy tumors or for heat induced drug release[56–58]. One example of such hybrid nanoparticles are pegylated SPIONs with incorporated Doxorubicin in the polymeric shell which were effective in detecting Lewis lung carcinoma and delivering efficient amounts of the drug to the target for successful applied theranostics[59].

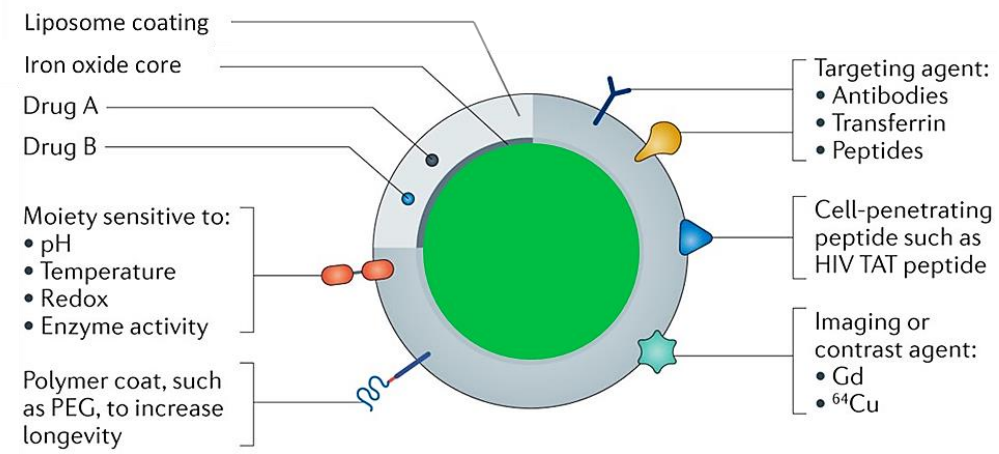

Figure 2 – Example of a hybrid nanoparticle with an inorganic core (SPION) and a lipid coating with various possible modifications. Lipophilic and hydrophilic drugs can be loaded, liposomes can be modified to be pH- or temperature sensitive, pegylated for shielding, and targeting agents can be added (changed from[60])

NANOPARTICLE SAFETY AND GUIDELINES

Various information and guidelines are existing to guarantee the safety of nanoparticles for medicinal usage for therapeutic, diagnostic or theranostic purposes[61]. Especially their different behavior compared to corresponding bulk materials makes it impossible to treat and regulate them the same way[62–64]. Talking about a general safety for all nanoparticles is difficult because of their broad application field with many different types[65]. But nevertheless, the topic is discussed in many publications and guidelines, even in the European Union nanoparticle regulatory approach called NanoREG[66–72]. This chapter will focus on intravenously (IV) applied nanoparticles used in clinical sciences. A lot of nanoparticles for medicinal usage are liposome-based with more than 12 already in the market and more than 20 still in the clinical phase (Table 2)[73]. One of the major problems is the long-term storage of these drugs because of physicochemical destabilization in aqueous solutions. The preferred method therefore is the lyophilization which ensures the long-term stability compared to other methods[74]. Also, more and more SPIONs are used for drug delivery, imaging and theranostics (Table 1)[38]. After IV injection, the nanoparticles immediately interact with the biological environment[75]. A biological coating of biomolecules, which are present in the blood plasma, will form around the particles, the so-called protein corona[76]. This can affect the nanoparticle behavior *in vivo*[77]. Therefore it is essential to characterize the nanoparticles additionally in a solution containing 10 % fetal bovine serum[78]. This will ensure, that the drug release, biodistribution, toxicity, intracellular uptake, immunological response, and *in vivo* targeting will not change after IV administration[76]. Further information and proposed techniques to ensure the safety of IV administered nanoparticles is explained by the following pages based on the review from Cörek et al.[79]:

Nanotoxicology is a very complex topic without defined standard testing protocols which are accepted from regulatory authorities. To solve this problem, more and more testing strategies were proposed in the last years to improve the time and money consuming case-by-case evaluations. These strategies are mainly focused on inhalation or oral administration but not on IV administration on purpose. Therefore, ensuring the safe usage of those nanoparticles is essential, especially to fill the existing gap in terms of nano-specific regulation and safety assessment for medical candidates. The term nanosafety is an interaction between the biological system, surface properties, and physicochemical properties of the nanoparticles. This hazard evaluation strategy for nanomedicines (HES) is an approach with three tiers (Figure 3). Based on the physicochemical properties (tier 1) and nanoparticle interactions (tier 2), the hazard assessment (tier 3) can be created. This helps at the end in the decision and prediction process.

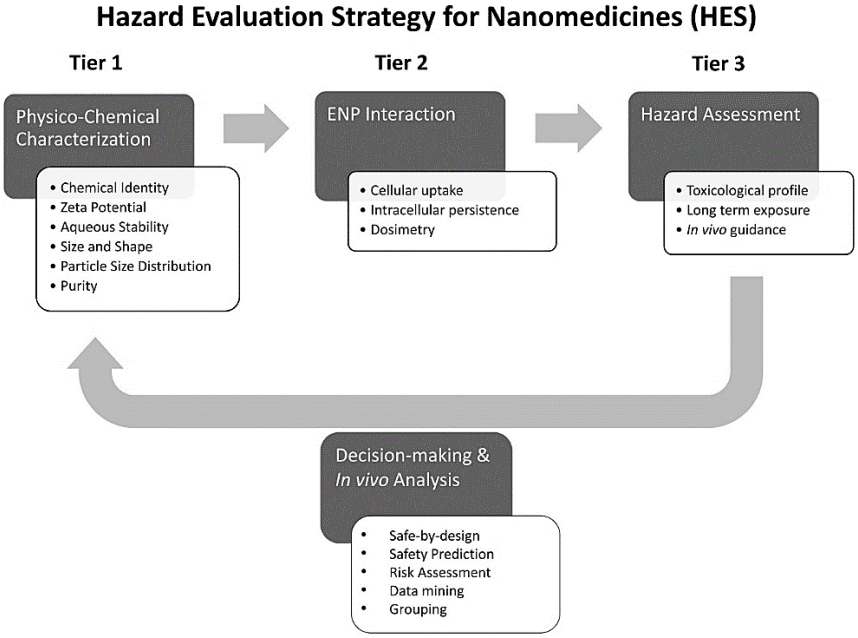

Figure 3 - Proposed hazard evaluation strategy from Cörek et al.[79] with different tiers to characterize and group nanoparticles in different hazard groups depending on their characteristics. Depending on the outcomes, those nanoparticles are declared as safe to use as IV applications.

To ensure the international availability, standardized testing protocols from the European Nanomedicine Characterization Laboratory (EUNCL) are used. The first tier serves as a starting point before continuing with *in vitro* toxicity testings to collect information like the zeta potential, aqueous stability, shape, size, contamination, and size distribution. This step-by-step approach shows, if the candidate is qualified to continue as an injectable nanoparticle to tier 2 or fails because of i.e. contamination that cannot be cleared by purification.

To find out the interactions of injectable nanoparticles in tier 2, cellular uptake and intracellular persistence is measured and based on the results, the particles are grouped in four different categories. Ideally, the cellular uptake is determined by combining qualitative and quantitative methods like confocal laser scanning microscopy (CLSM) together with flow cytometry. The administered dose and the incubation times are important values which should be considered. The corresponding cell types are chosen based on first contact after injection which are likely to be endothelial cells. The persistence is determined with the same cell types by looking on the intracellular degradation level after defined periods of time, i.e. by electron microscopy.

After categorizing the nanoparticles, further testings are done in tier 3 based on the respective category. Those are set up with eight different assays (complement activation, platelet aggregation, hemolysis, oxidative stress, cell viability, phagocytosis, inflammation, and DNA damage) with increasing amounts from category one to four because of possible increasing interaction chains *in vivo* with increasing uptake and persistence (Figure 4). Nevertheless, those categories don’t necessarily define the toxicity. But the possibility of more/longer interactions also increases the risk, which needs to be determined and evaluated.

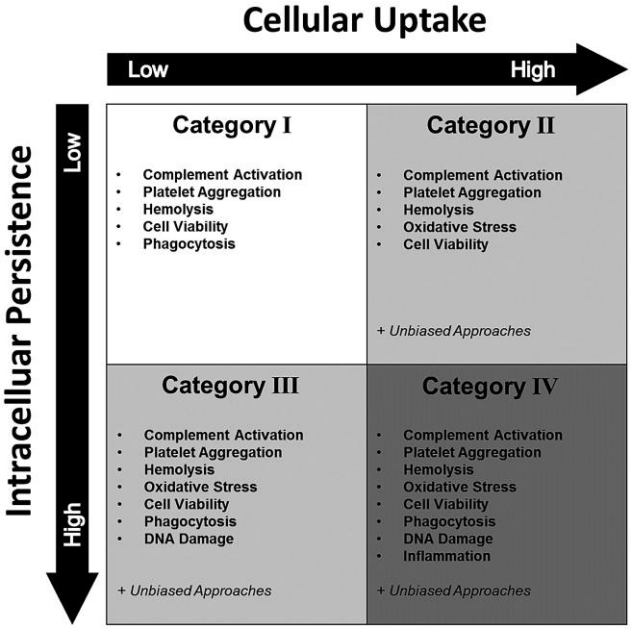

Figure 4 – Tier 3 of the HES approach with different hazard assessment tests based on the four categories the nanoparticles entered after tier 2. The categories are defined by high/low intracellular persistence and cellular uptake of the nanoparticles (copied from[79]).

At the end of the day, this approach is an example of a concept which is easy and robust to apply, reduces costs, and is completely application-oriented. It fastens up and standardizes preclinical safety evaluations, reduces *in vitro* testings by pre-selecting relevant candidates, promotes the 3R principles, identifies off-target effects *in vivo*, and finally helps grouping of nanoparticles. This will help researchers and developers during product design and will lead a step further to much needed standardized safety testing strategies for the future.

II. ZEBRAFISH (*DANIO RERIO*)

First scientific recordings of *Danio rerio* were made in 1822 from the naturalist Francis Hamilton. He described them as beautiful but not from value[80]. *Danio rerio* live in South Asia in India, Pakistan, Nepal up to the Southern Himalayas in the North[81]. Found in fresh water i.e. rivers, channels, and small streams, they can survive in a

broad temperature and pH-range affecting their mutations and breeding time[82]. Inbred zebrafish can live in average 3.5 years, with oldest individuals living up to 5.5 years[83]. Today it is known, that zebrafish have together with humans and mouse the best genome sequence assembly and gene annotation of all vertebrates with almost 70 % orthologues with human genes[84,85]. *Danio rerio* belongs to the class of *Actinopterygii* and their subclass *Teleostei* which are part of the *Cyprinidae* family[86]. This *Danio* genus contains more than 40 different fish together with *Danio rerio* as an important vertebrate model for biomedical research[87].

ANATOMY AND HISTOLOGY

Danio rerio have many anatomical and physiological properties in common with vertebrates including humans[88]. Their maximal length is up to 40 mm and they have a “fusiform and laterally compressed body shape with a terminal oblique mouth directed upwards”[81]. They express different types of dark blue lateral stripes, a typical phenotypic trait of this genus[89]. Three types of pigment cells are included in their color pattern, dark blue melanophores, gold xanthophores and iridescent iridophores[90]. There are various genetically modified strains with different phenotypes and characteristics such as the so called “casper”, a strain where the zebrafish are completely transparent because of a melanocyte and iridophore lack[91]. Compared to mammals, zebrafish have no medullary cavity so the hematopoiesis takes place in the interstitium of their kidneys[92]. Sinuses are lined with endothelial cells which are filtering the blood and adding new blood cells into the circulation[93]. The blood consists of erythrocytes for oxygen transport and thrombocytes for blood clotting[94]. Leukocytes play an important role for the immune system, which are consisting of neutrophilic and eosinophilic granulocytes[95]. Neutrophils are similar to the mammalian neutrophils but eosinophils differ and the question if they have a similar

function is not clear[96]. Around five to 15 % of the leukocytes are consisting of monocytes which are similar to mammalian monocytes and will develop into macrophages mainly in the kidney and spleen region of adult zebrafish[97]. The spleen and kidneys of zebrafish are the main filtering organs because like other teleosts, they don't have lymph nodes[98]. Kidneys are quite similar to humans with nephrons consisting of glomerulus, proximal tubules, distal tubules, and collecting ducts[92]. The liver is the major player in metabolic homeostasis similar to mammals[94]. Also the brain is comparable to mammals and consists of five regions (telencephalon, diencephalons, mesencephalon, metencephalon, and myelencephalon)[99]. Another organ which is identical to higher vertebrates are the eyes consisting of three layers (tunica fibrosa, tunica vasculosa, and the retina)[92]. Very important for orientation, perception of sound, acceleration, and change in equilibrium are the otholiths. They are made of calcified stones and lie on sensory epithelium cells[92]. In general, the zebrafish is a well-fit model organism to study human disease, toxicology and drug delivery because of the anatomical, developmental and histological similarities[100].

BREEDING AND DEVELOPMENT

Zebrafish are regulated after the EU Directive 2010/63/EU that defines the protection of animals and is one of the most strict international standards for animal welfare and ethics[101]. In there, the earliest animal life-stages are not defined as protected and therefore, the zebrafish embryos are not considered as animals until 120 hours post fertilization at 28.5° C due to "depending feeding" from their yolk[102]. The following information about breeding are gathered from[103] and say that as soon as new adult zebrafish arrive in the laboratories, they need to be hold in quarantine to eliminate the risks of pathogens and increase biosecurity. They are hold in commercially available glass or PVC tanks "fully integrated with filter systems, germicidal irradiation

(UVC) and light and temperature control units". Their volume is around 10 liters and they are connected to a pure freshwater circulation system, where the used water is constantly purified and reused. The temperature is usually kept constant between 24 and 29° C at a "static dark–light (D–L) cycle" of 10 hours dark and 14 hours light. The adult fish can be kept between 3-12 fish/L without the need to physically enrich the environment because of lack of evidence that it increases benefits. Feeding takes place 2-3 times a day with different living organisms like *Artemia nauplii* from a pathogen-free source. Zebrafish have a high fecundity with a female fish spawning hundreds of eggs per mating. It is recommended to keep two to three males together with six to seven females during mating process in smaller tanks overnight with a sieve and physical structures like plastic plants and small stones which are mimicking the natural environment. The morning after mating, the eggs are removed and cleaned from feces and hold constantly in embryo medium containing 0.5 mg/l methylene blue to reduce fungal infections in D-L cycle at 28.5 ± 0.5° C. Stocking density is 100 embryos in 35 ml of medium in a nine cm diameter Petri dish. Between matings, the used embryos should at least get a break of one week to allow recovery.

After the eggs are hatched, the embryos immediately start to develop. Following information gathered from Kimmel et al. shows the different developmental stages[104]: After the fertilization, the zygote period (1-cell) starts where a first cleavage occurs. This continues with the cleavage period (2-cell), where every 15 minutes the cells divide themselves followed by the blastula period (128-cell). Followed by the gastrula (50%-epiboly), segmentation (3- and 14-somite), and pharyngula (prim-6) period, where the eggs are usually bleached to inhibit pigmentation with phenylthiourea (PTU), inhibiting TYR-dependent melanogenesis pathway, at a concentration of 75

μM[105]. After 48 hpf the hatching (long pec and protruding mouth) period is reached where the protruding-mouth is visible after 72 hpf (Figure 5).

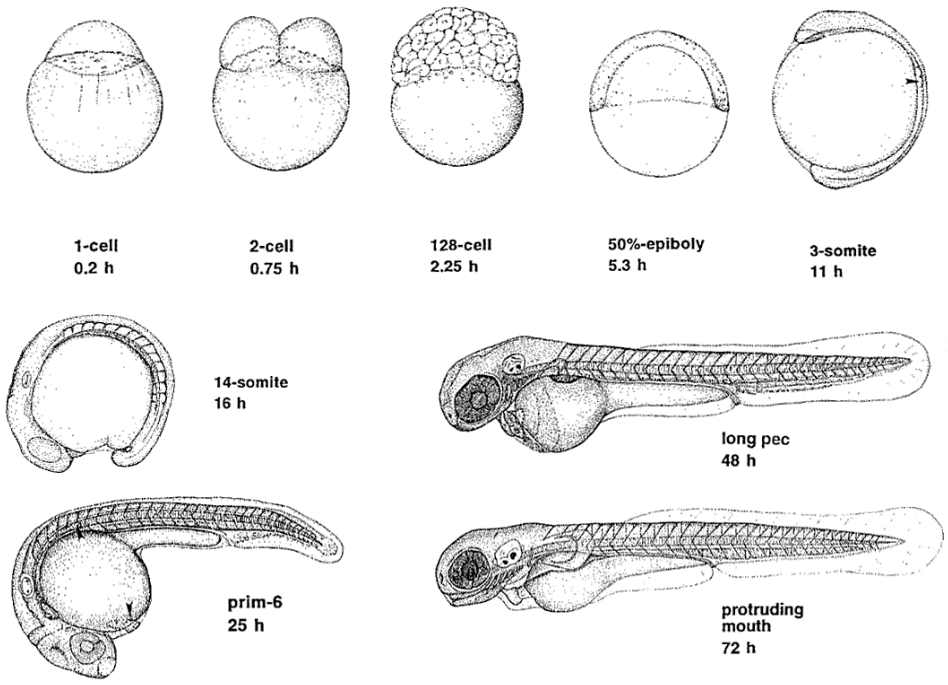

Figure 5 – Sketches made with a *camera lucida* of the zebrafish embryo at selected stages between 1-cell state at 0.2 hpf and fully developed embryo with a protruding mouth at 72 hpf (changed from[104])

ZEBRAFISH AS A MODEL ORGANISM

The first mentioning of zebrafish embryos as a model organism in laboratory research was in the early 1900s with a protocol for zebrafish handling[106]. In the following years between 1940s and 60s, several scientists used zebrafish for examination of developmental and behavioral biology, neurobiology, toxicology, and oncology. Starting from there, in the recent 40 years, zebrafish become a popular and well suited model organism in laboratories because of their easy handling and manipulation, high fecundity, rapid development, and small size[86] (Figure 6). One of the key figures in adapting zebrafish to a broad range of people was George Streisinger, a molecular biologist and aquarium hobbyist, who understood the

advantages of the model organism and optimized their breeding and care, developed mutation, genetical and clonal analysis of cell origins tools and started also a first genetical screening of zebrafish[107–109]. His work was continued by his colleague Charles Kimmel, which is now one of the most cited scientists in the field of zebrafish[110]. In 1996, the categorization and descriptions of 1163 mutant zebrafish lines was published which set the genetical basis for the phenotypes[111] and was completed by the zebrafish genome sequencing and comparison to human genome between 2001 and 2013[84].

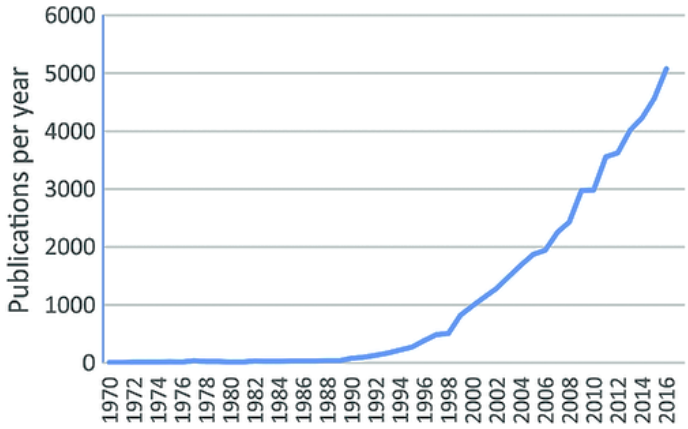

Figure 6 – Increase of publications including the words zebrafish, *Brachydanio rerio*, or *Danio rerio* in the last 30 years (copied from[86])

It was found out, that the genome of zebrafish contains around 26,000 genes over 1.4 billion base pairs on 25 pairs of chromosomes. Today, there is a wide variety of transgenic zebrafish strains which express fluorescent proteins, Cre-recombinases, cell-death proteins, also with the ability to manipulate other proteins[112,113]. One of the zebrafish strains used in this work was the mpeg1:kaede strain expressing green fluorescent kaede protein in macrophages[114]. Also, zebrafish are used for toxicological studies like tumor induction by carcinogens[115] or screening toxic compounds[116]. In drug delivery, zebrafish are used for screening of macrophage

clearance[117], and nanomedicines[118], or identifying off-target drug effects[119]. Especially for human disease models, zebrafish embryos suit very well because of their gene mutations that are orthologous to human disease genes with clear phenotypic similarities as a result[100]. With that, zebrafish are able to act as a pre-screening model prior to animal experiments and are reducing animal experiments in compliance with the 3R - Replace, Reduce, Refine – principle[120,121].

III. IMAGING TECHNIQUES

The history of microscopy started around 1021 AD. Muslim medieval physicist Ibn al-Haytham (*Alhazen*) wrote the seven-volume "Book of Optics*"* (*Kitab al-Manathir*) which "hugely influenced thinking across disciplines from the theory of visual perception to the nature of perspective in medieval art, in both the East and the West, for more than 600 years"[122]. The "Book of Optics*"* was then translated into Latin in the early 13th century, as "*De Aspectibus"*. This work was a basis in this field and influenced the future research tremendously. In the 11th century, the Arab world used plano-convex lenses made out of polished beryl which were used for magnifying manuscripts. Starting from this point, the first compound microscopes with an adjustable magnification of 3 or 9 X were built in the 16th century by the Dutch spectacle maker Hans Janssen and his son Zacharias followed by Galileo Galilei in 1609, who built a microscope out of a telescope[123]. Inspired from this, Johannes Kepler had the idea to create a microscope consisting of two converging lenses which was presented by the astronomer Cornelius Drebbel. The first publication about microscopes came out 1667 from the English universal scholar Robert Hooke with various studies using microscopes[124]. Antonie van Leeuwenhoek analyzed in 1674 some lake water and discovered bacteria which was a milestone[125]. The microscopes were further improved and 1863, the Ernst Leitz microscope manufacturer company

introduced the first revolving turret with more than five objectives. In 1869, Ernst Abbe who was working for Zeiss Optical Works, founded by Carl Zeiss, invented the new patented illumination device called the Abbe condenser that was the basis for immersion objectives[126].

Table 3 - Overview of different imaging techniques, their spatial resolution, scan time, used contrast agents, and their area of application (changed from[127])

Imaging Technique	Spatial Resolution	Scan Time	Contrast Agents and Molecular Probes	Key Use
Multi-photon Microscopy	15 – 1000 nm	Secs	Fluorescent proteins, dyes, rhodamine amide, quantum dots	Visualization of cell structures
Atomic Force Microscopy	10 – 20 nm	Mins	Intermolecular forces	Mapping cell surface
Electron Microscopy	~5 nm	Secs	Cyrofixation	Discerning protein structure
Ultrasound	50 μm	Secs	Microbubbles, nanoparticles	Vascular imaging
CT/MicroCT	12 – 50 μm	Mins	Iodine	Lung and bone tumor imaging
MRI/MicroMRI	4 – 100 μm	Mins – Hrs	Gadolinium, dysprosium, iron oxide particles	Anatomical imaging
fMRI	~1 mm	Secs – Mins	Oxygenated hemoglobin (HbO_2) deoxygenated hemoglobin (Hb)	Functional imaging of brain activity
MRS	~2 mm	Secs	N-acetylaspartate (NAA), creatine, choline, citrate	Detection of metabolites
PET/MicroPET	1 – 2 mm	Mins	Fluorodeoxyglucose (FDG), ^{18}F, ^{11}C, ^{15}O	Metabolic imaging

The various micro versions of the imaging modalities (MicroCT, MicroMRI, MicroPET) as well as the microscopy techniques (Fluorescence, Multi-photon, Atomic, Electron) are primarily used in either cellular or animal studies. The remaining modalities (Ultrasound, CT, MRI, MRS, PET) are more widely used clinically.

Today, we have a broad variety of different imaging techniques (Table 3). They all differ in their spatial resolution, area of application, scan time, and also with the usable contrast agents[127]. In the following chapters, the imaging techniques used in this work are further explained in more detail.

LIGHT AND FLUORESCENCE MICROSCOPY

LIGHT MICROSCOPY

The light microscope has a mechanical construction made of different pieces. One of the more advanced devices is the compound microscope. Here, an objective lens close to the viewed sample is used and applying light for illumination, the sample is magnified and visible inside the microscope. Together with the eyepieces, magnifications up to 2000 times are possible[128]. In light microscopy, the illumination source and the objectives are on different sides of the sample, so the light needs to pass through the specimen for visualization. Because of the thin sample layers, low amounts of light is absorbed which leads to a low contrast[129]. To overcome this, phase contrast and differential interference contrast (DIC) techniques are used. Phase contrast increases the contrast by showing i.e. cells darker on a bright background. DIC gives a “pseudo–three-dimensional (3D) shaded appearance” to the cells[130].

FLUORESCENCE MICROSCOPY

Instead of light, also fluorescent dyes in combination with an excitation and emission wavelength can be used to see different fluorescent structures in the sample. The structures are visible either by genetical modification with a fluorescent protein or by manual fluorescent labeling with fluorescent antibodies (immunofluorescence). Also multiple fluorescent structures can be visualized at once by using different wavelengths with the respective fluorophores[128]. An overview of different fluorescent proteins can be found in Table 4.

Table 4 – Overview of different fluorescent proteins and their excitation and emission wavelengths, molar extinction coefficients (EC), quantum yields (QY), physiological quaternary structures, and relative brightness (changed from[131]).

Protein (acronym)	Ex/nm	Em/nm	EC/10^{-3} M^{-1} cm^{-1}	QY	Quaternary structure	Relative brightness (% of EGFP)
Blue fluorescent proteins						
Sirius	355	424	15.0	0.24	Monomer*	11
Azurite	384	448	26.2	0.55	Monomer*	43
EBFP	383	445	29.0	0.31	Monomer*	27
EBFP2	383	448	32.0	0.56	Monomer*	53
Cyan fluorescent proteins						
ECFP	439	476	32.5	0.40	Monomer*	39
Cerulean	433	475	43.0	0.62	Monomer*	79
CyPet	435	477	35.0	0.51	Monomer*	53
SCFP	433	474	30.0	0.50	Monomer*	45
Green fluorescent proteins						
EGFP	488	507	56.0	0.60	Monomer*	100
Emerald	487	509	57.5	0.68	Monomer*	116
Superfolder avGFP	485	510	83.3	0.65	Monomer*	160
T-Sapphire	399	511	44.0	0.60	Monomer*	79
Yellow fluorescent proteins						
EYFP	514	527	83.4	0.61	Monomer*	151
Topaz	514	527	94.5	0.60	Monomer*	169
Venus	515	528	92.2	0.57	Monomer*	156
Citrine	516	529	77.0	0.76	Monomer*	174
YPet	517	530	104	0.77	Monomer*	238
SYFP	515	527	101	0.68	Monomer*	204
mAmetrine	406	526	45.0	0.58	Monomer	78

ELECTRON MICROSCOPY

The operation of the electron microscope is similar to the light microscope but the illumination source is substituted by an electron beam. Instead of glass lenses, electromagnetic and -static lenses are used[128]. The samples are specially prepared by staining with uranyl acetate or lead citrate to make a thin layer of electron-dense material on top of the specimens[132] and are placed on special metal grids made out of copper or other metals with a grid mesh size between 100 and 400. Samples need to be very thin which is achieved by using i.e. the Porter Bloom microtome that is able to cut 1 µm or ultrathin 40-60 nm histological sections[133]. Mainly, two different imaging methods are available, transmission electron microscopy (TEM) and scanning electron microscopy (SEM). TEM is mostly used for characterization of morphology, crystalline structures, membrane materials, or nanoparticles[134,135]. Nowadays, even tomography is possible with TEM, which is scanning a sample layer-by-layer and merging the images at the end to a 3D object. A disadvantage of this method is the appearance of artifacts[136]. In comparison to TEM, SEM is providing for the upper 1 µm layer of a sample an analysis of the surface topography, crystalline structures,

chemical composition and electrical behavior with magnifications up to 1 million times with an ultimate resolution of 1 nm[137]. Another method is the cryo-electron microscopy (cryo-EM) in which biological samples can be rapidly frozen, allowing visualization of organic macromolecules or soft matter materials like organic compounds, for example liposomes, in near-native environments[138].

CONFOCAL LASER SCANNING MICROSCOPY

There are several different types of confocal laser scanning microscopes (CLSMs). They are able to remove appearing blur from outside of the focal plane of images[139]. The principle can be explained as a laser beam light which is focused to a small area on the specimen. At this spot, the fluorophores are excited and the fluorescent emission is then reflected on a detector through a variable pinhole. Here, the fluorescence is measured on this specific in-plane focus spot which is becoming 1 pixel in the image afterwards. By moving the focused spot and repeating the whole procedure, an entire image of the specimen is created pixel-by-pixel. By changing the focal plane, 3D scans can be acquired which will give depth information of the specimen (acquisition of z-stacks). Another factor is the scan speed. Slower scan speeds result in better signal to noise ratios (S/N) because each pixel intensity will be integrated longer. At the same time, photobleaching of the fluorophores will also increase[139]. Therefore, the goal should be to gather images quantitatively with maximal S/N without clipping the data[140].

MICRO(SCOPIC) COMPUTED TOMOGRAPHY (MICRO-CT OR µCT)

The invention and usage of the µCt goes back to the 1980s where it is described as a “new technique of x-ray microtomography generates nondestructively three-dimensional maps of the x-ray attenuation coefficient inside small samples with

approximately one percent accuracy and with resolutions approaching one micrometer"[141]. Usually the system consists of a high-resolution imaging detector and of high-speed algorithms for generating the tomographic 3D reconstruction[141,142]. CT is a 3D X-ray imaging method where the sample is being rotated around the vertical or horizontal axis and many 2D images (image stacks) are generated. Those images made out of pixels (x μm^2) are then calculated back to the full 3D sample with internal structures by reconstruction defined by voxels (x μm^3). The µ in µCt stands for the submillimeter voxel resolution which is possible with these devices with spatial pixel resolutions between 12 and 50 µm (Table 3)[143]. The µCt has three main components: X-Ray source, X-Ray detector panel, and integrated algorithms to overcome hardware limitations and make reconstructions out of projections (Figure 7)[143].

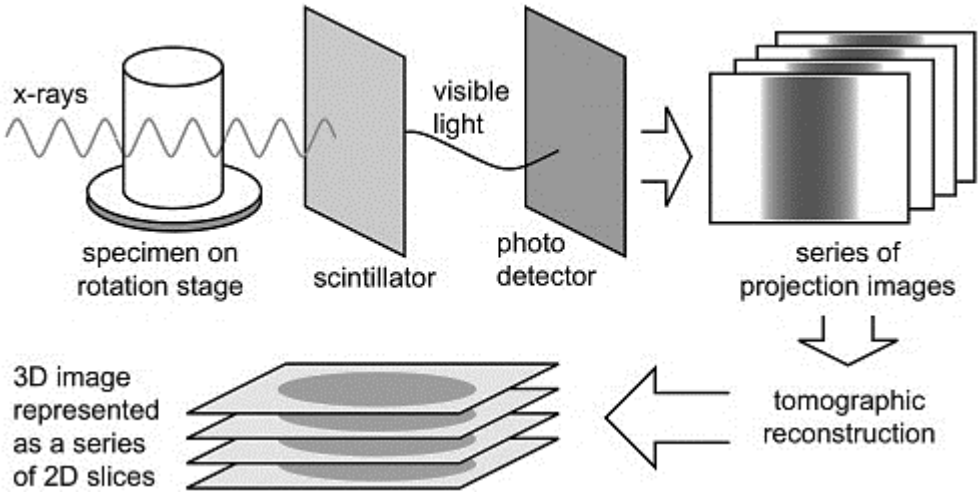

Figure 7 – Schematic representation of X-ray (µ)CT acquisition and reconstruction. X-rays going through the sample which is on a rotation stage and detected by a photo detector. The series of projection images are then reconstructed to a 3D volume which is made of 2D slices (copied from[144])

The µCt imaging is based on X-ray absorption of different materials depending on their electron density. This makes it possible to identify different structures of a 3D sample by plotting the voxel intensities (x-axis) against the number of voxels (y-axis).

The less dense structure peaks will be seen on the left, and the higher dense structure peaks on the right side of the x-axis (voxel intensity histogram)[144]. Based on this histogram, it is possible to segment the digital 3D volume of the sample in different components (intensity-based segmentation). Because samples with soft tissue have a very similar absorption, it can be difficult to segment them based on their density. For this reason, it can be helpful to either use contrast agents or to use a method with a high flux like the synchrotron radiation with more details in the next chapter[145].

SYNCHROTRON

The synchrotron radiation X-Ray µCT has increased benefits compared to the usual µCT i.e. higher resolution, higher X-ray flux and faster scan times[146]. If fast speed detectors are combined with high speed algorithms, nearly real-time speed scans are possible[144].

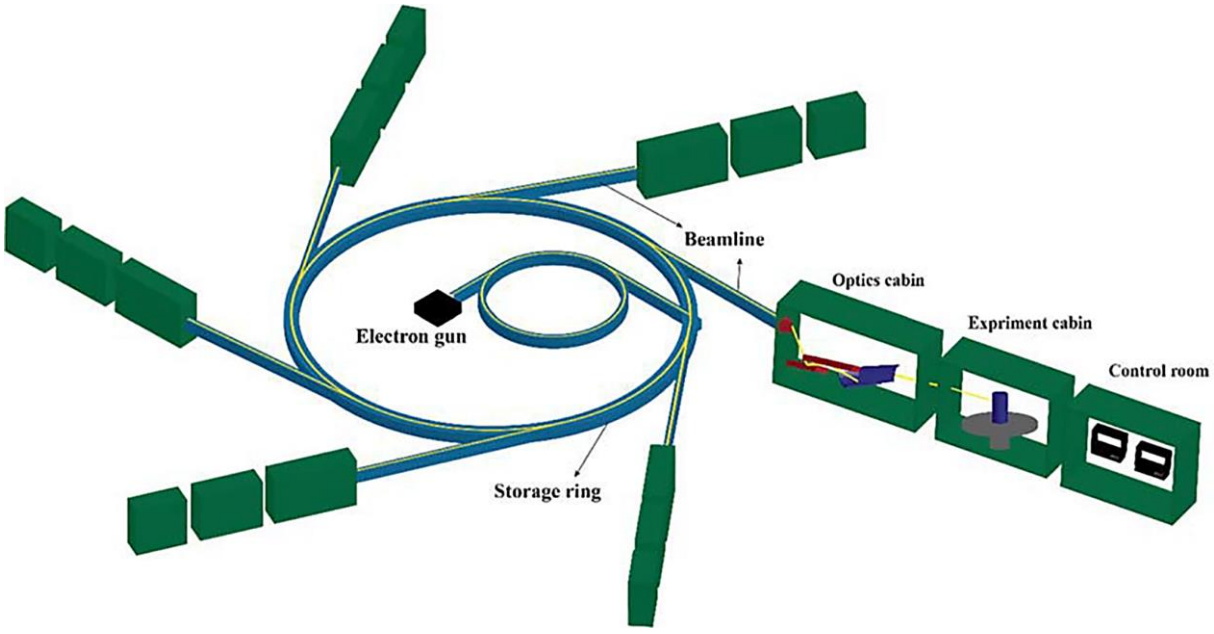

Figure 8 – Scheme of a synchrotron facility with the linear accelerator containing the electron gun and booster synchrotron, storage ring, beamlines, optics and experiment cabin, and control room (copied from[147])

The components of a synchrotron are as shown in Figure 8 a linear accelerator (linac) with an electron gun, producing electrons similar to a cathode ray where the electrons are pulled out with an energy of 90 kV between cathode and anode. They are accelerated up to 200 million electron-volts (MeV) before getting injected into a 270 to 300 m booster synchrotron ring that accelerates the electrons to a given energy (between 2.4 to 6 billion electron-volts (GeV)). The storage ring which is between 288 844 meters long depending on the facility, is a high-vacuum tube (around 10^{-9} mbar), where the electrons are kept at near speed of light. During this process, the electrons pass different magnets like bending magnets, which are at every curved section and force the electrons to the path of the tube, focusing magnets which ensure that the electrons stay on their ideal orbital path, and the undulators, a complex set of magnet arrays, where the intense X-ray beams are produced[148,149]. The undulators force the electrons to a wavy path to generate much more brilliant light beams compared to single magnets. The synchrotron light produced at facilities have an energy between 10 to 120 keV and a wavelength of 0.10 to 0.01 nanometers (ultra-violet to hard X-Rays). This is so small, that even atoms can be studied due to the closeness to interatomic distances[150]. The beamline itself is built of optics, experimental and control cabins. From the beginning to the end, the beamline consists of the source (entrance from the storage ring), lits, safety components like beam shutter and beam stopper, mirrors with filters to focus and cut away unwanted parts of the spectrum, well-polished and highly precise mirrors serving as lenses, and a monochromator for selecting a single wavelength made out of crystal followed by the experimental cabin[151]. Also in this method, absorption contrast is very weak between organic compounds *in vivo* and because of this, phase contrast imaging is used to enhance the contrast drastically by exploring the refractive index of the components[152]. To study larger animals, the body still needs to be sacrificed to examine single organs

or tissue areas. For smaller animals like *C. elegans* or *Danio rerio*, it is possible to analyze the whole sample non-destructively as a whole 3D model to see i.e. nanoparticle distributions[152,153]. This was also done in this work by using *Danio rerio* embryos to analyze the hybrid nanoparticle *in vivo* biodistribution by using synchrotron radiation X-ray µCT phase-contrast imaging and segmentation of the reconstructed digital 3D volume of the samples.

CHAPTER 3: AIM OF THE THESIS

The usage of nanoparticles in general, especially in drug delivery, imaging, and theranostics, is increasing since years. Therefore, one of the main questions of this thesis was how to ensure the safe usage of those nanoparticles and try to group them in populations with similar toxicity profiles and behaviors to make predictions by screenings in future. Out of a broad variety of different nanoparticles, superparamagnetic iron oxide nanoparticles and liposomes were chosen to create hybrid nanoparticles with characteristics of both groups. An electron dense and superparamagnetic core makes magnet-driven targeted drug delivery, *in vivo* imaging, and target-site manipulation like local hyperthermia possible. The liposome-coating is additionally modifiable with different targeting or imaging agents, peptides, polymer additions like PEG to increase stability, and lipo- or hydrophilic drug loading. So the second goal of this thesis was to establish a stable method to produce those hybrid nanoparticles, characterize them and use them for imaging and biodistribution studies in a small vertebrate animal model (*Danio rerio*). A short summary of the aims are:

- Evaluation of existing nanoparticle safety guidelines and working out a new guideline for intravenously applied clinical nanoparticles
- Working out a solid synthesis method for SPION/liposome hybrid nanoparticles, characterization, and analysis of biodistribution by imaging *Danio rerio* embryos with different methods including synchrotron µCT
- *In vivo* targeting with SPION/liposome hybrid nanoparticles and manipulation of those by magnetic fields and acoustic waves

CHAPTER 4: RESULTS

The results of this thesis were published / submitted* in the following journals:

1) Preclinical hazard evaluation strategy for nanomedicines, Cörek et al. (shared first author), Nanotoxicology, 13:1, 73-99 (2019)

2) Shedding Light on Metal-Based Nanoparticles in Zebrafish by Computed Tomography with Micrometer Resolution, Cörek et al., SMALL (2020)

3) Magnetic field induced phagocytosis of iron oxide nanoparticles in zebrafish embryo (*Danio rerio*), Cörek et al.*

4) Further publications as Co-Author:

    - Removing ring artefacts from synchrotron radiation-based hard x-ray tomography data, Thalmann et al., SPIE Proceedings (2017)
    - Propagation-based X-ray Phase Contrast Microtomography of Zebrafish Embryos to Understand Drug Delivery, Schulz et al., Microscopy and Microanalysis (2018)
    - An Introduction to Synchrotron Radiation: Techniques and Applications, Second Edition, Philip Willmott, John Wiley & Sons (2019)

*will be submitted to a journal, work in progress

I. PRECLINICAL HAZARD EVALUATION STRATEGY FOR NANOMEDICINES

Emre Cörek (shared first author), Stefan Siegrist (shared first author), Pascal Detampel, Jenny Sandström, Peter Wick, Jörg Huwyler

Journal: published in Nanotoxicology, 13:1, 73-99 (2019)

DOI: https://doi.org/10.1080/17435390.2018.1505000

Nanotoxicology

Taylor & Francis
Taylor & Francis Group

ISSN: 1743-5390 (Print) 1743-5404 (Online) Journal homepage: https://www.tandfonline.com/loi/inan20

Preclinical hazard evaluation strategy for nanomedicines

Stefan Siegrist, Emre Cörek, Pascal Detampel, Jenny Sandström, Peter Wick & Jörg Huwyler

To cite this article: Stefan Siegrist, Emre Cörek, Pascal Detampel, Jenny Sandström, Peter Wick & Jörg Huwyler (2019) Preclinical hazard evaluation strategy for nanomedicines, Nanotoxicology, 13:1, 73-99, DOI: 10.1080/17435390.2018.1505000

To link to this article: https://doi.org/10.1080/17435390.2018.1505000

Published online: 05 Sep 2018.

NANOTOXICOLOGY
2019, VOL. 13, NO. 1, 73–99
https://doi.org/10.1080/17435390.2018.1505000

Taylor & Francis
Taylor & Francis Group

REVIEW ARTICLE

OPEN ACCESS Check for updates

Preclinical hazard evaluation strategy for nanomedicines

Stefan Siegrist[a]*, Emre Cörek[a]*, Pascal Detampel[a], Jenny Sandström[b], Peter Wick[c] and Jörg Huwyler[a]

[a]Division of Pharmaceutical Technology, Pharmacenter, University of Basel, Basel, Switzerland; [b]Swiss Centre for Applied Human Toxicology, Basel, Switzerland; [c]Laboratory for Patricles-Biology Interactions, Empa Swiss Federal Laboratories for Materials Science and Technology, St. Gallen, Switzerland

ABSTRACT

The increasing nanomedicine usage has raised concerns about their possible impact on human health. Present evaluation strategies for nanomaterials rely on a case-by-case hazard assessment. They take into account material properties, biological interactions, and toxicological responses. Authorities have also emphasized that exposure route and intended use should be considered in the safety assessment of nanotherapeutics. In contrast to an individual assessment of nanomaterial hazards, we propose in the present work a novel and unique evaluation strategy designed to uncover potential adverse effects of such materials. We specifically focus on spherical engineered nanoparticles used as parenterally administered nanomedicines. Standardized assay protocols from the US Nanotechnology Characterization Laboratory as well as the EU Nanomedicine Characterisation Laboratory can be used for experimental data generation. We focus on both cellular uptake and intracellular persistence as main indicators for nanoparticle hazard potentials. Based on existing regulatory specifications defined by authorities such as the European Medicines Agency and the United States Food and Drug Administration, we provide a robust framework for application-oriented classification paired with intuitive decision making. The Hazard Evaluation Strategy (HES) for injectable nanoparticles is a three-tiered concept covering physicochemical characterization, nanoparticle (bio)interactions, and hazard assessment. It is cost-effective and can assist in the design and optimization of nanoparticles intended for therapeutic use. Furthermore, this concept is designed to be adaptable for alternative exposure and application scenarios. To the knowledge of the authors, the HES is unique in its methodology based on exclusion criteria. It is the first hazard evaluation strategy designed for nanotherapeutics.

ARTICLE HISTORY
Received 3 May 2018
Revised 25 June 2018
Accepted 20 July 2018

KEYWORDS
Nanoparticles; nanomedicine; hazard assessment; safe-by-design

1. Introduction

Engineered nanoparticles (ENP) were first introduced to the market as pharmaceutical indications in 1957 and 1959, when iron dextran and sucrose products of Sanofi Aventis and Vifor were approved for the intravenous treatment of iron deficiency in patients with chronic kidney disease. Since the approval of the anti-cancer drug Doxil®/Caelyx® by the United States Food and Drug Administration (FDA) in 1995, the number of yearly approved ENP formulations designed for medical purposes are steadily increasing (Etheridge et al. 2013; Pelaz et al. 2017; Weissig, Pettinger, and Murdock 2014; Witzigmann et al. 2015). Today, it is well accepted that ENP have an undisputable potential as drug carriers (Bozzuto and Molinari 2015; Coti et al. 2009; Puri et al. 2009), imaging agents (Arap et al. 2013; Toy et al. 2014; Unterweger et al. 2017), vaccines (Gregoriadis 1985; Gregory, Titball, and Williamson 2013; Zhao et al. 2014), and theranostic tools (Ambrogio et al. 2011; Elgqvist 2017; Xie, Lee, and Chen 2010). Nevertheless, ENP are not risk-free substances and safety concerns towards these novel formulations have to be addressed (Fadeel 2012; Wolfram et al. 2015). ENP may induce adverse side effects, which is not the case for the bulk chemicals they are composed of (Nel et al. 2006; Shvedova, Kagan, and Fadeel 2010; Singh 2015; Yildirimer et al. 2011). For example,

CONTACT Jörg Huwyler joerg.huwyler@unibas.ch Division of Pharmaceutical Technology, Pharmacenter, University of Basel, Klingelbergstrasse 50, 4056 Basel, Switzerland.
*Both authors contributed equally to the present work.

physicochemical characteristics such as particle size, shape, and surface properties (e.g. charge) have proven to influence the toxicological profile of ENP heavily regardless of their chemical composition (Berger 2009; Buzea, Pacheco, and Robbie 2007; Park et al. 2011). It is therefore generally believed that ENP cannot be regulated in the same way as bulk chemicals (Feliu and Fadeel 2010). In particular, a more detailed understanding of how and why nanoparticles interact with biological systems has to be developed (Dusinska et al. 2009; Guadagnini et al. 2015; Seaton et al. 2010). However, due to the shortage of nano-specific safety guidelines, nanomedicines are not regulated differently from 'ordinary' pharmaceuticals up to date. The awareness of nanoparticle toxicity has sensitized researchers and authorities alike to address these concerns and in turn has led to an increasing interest in phenomena related to 'nanotoxicology' (Gallud and Fadeel 2015; Gebel et al. 2014; Krug 2014).

Over the past decades, a plethora of research has been conducted on various ENP to better understand how and why nanoparticles are potentially toxic. It was found that nanoparticles entering an organism start to interact with their surroundings immediately (Kettiger et al. 2013; Unfried et al. 2007; Wu and Lu 2016). The nature of these interactions is dependent on the physicochemical identity of the nanoparticles, their surface properties, as well as the environment they encounter (Figure 1)(Fubini, Ghiazza, and Fenoglio 2010; Joris et al. 2016; Kim et al. 2015; Yang et al. 2017).

Today, it is known that many ENP are readily taken up by numerous cell types and have the ability to cross intra-cellular barriers as well as inter-cellular spaces (Guarnieri et al. 2014; Saraiva et al. 2016; Shimizu, Nakamura, and Watano 2016). Depending on type, dose, and incubation time, ENP can cause, e.g. the generation of reactive oxygen species, activate the complement system, or disrupt the functionality of membranes and cellular barriers (Guo et al. 2015; Moghimi and Simberg 2017; Sayes, Banerjee, and Romoser 2009; Siegrist et al. 2017). These actions lead to acute or chronic damage in the organism culminating in serious outcomes such as inflammation, gene aberrations, and severe organ damage (Nemmar et al. 2016; Vermeij et al. 2015; Wen et al. 2017). Yet – albeit all the efforts of elucidating nanotoxicological patterns – no standardized procedures exist to uniformly determine the safety of ENP. Ongoing debates about general definitions, ideal test systems, or how to group and classify ENP prevent the harmonization of existing safety and testing guidelines (Bleeker et al. 2013; Mühlebach, Borchard, and Yildiz 2015; Scott-Fordsmand et al. 2014; Whitesides 2003). Complicating this matter further, a number of clinical applications (e.g. in oncology) rely explicitly on cytotoxic effects induced by nanomedicines. Here, toxic effects are thus part of their mode of action (MoA) (Bao et al. 2015; Hung et al. 2016). Today, finding a consensus on how to evaluate the safety of ENP is one of the most controversially discussed topics among researchers (Nel et al. 2006), regulatory bodies (Stone et al. 2014), and authorities (van Teunenbroek 2017) alike.

The term nanotoxicology is generally defined as *'[…] the study of the adverse effects of engineered nanomaterials (ENM) on living organisms and the ecosystems, including the prevention and amelioration of such adverse effects. […]'* (Oberdörster 2010). This definition comprises environmental safety as well as adverse drug effects and consumer health thereby targeting every possible nanomaterial (including ENP). In contrast to this highly condensed and straightforward definition, the process of studying, preventing, or minimizing adverse effects caused by nanomaterials is very complex. So far it has not been possible to reach a consensus on how the safety on nanomaterials should be assessed using efficient methods and protocols, which are accepted by regulatory bodies. The reasons are manyfold: lack of defined reference material to benchmark the outcome of the tested material, lack of consensus on predictive endpoints for human toxicity, technical limitations of the tests for ENP (e.g. interference), and batch-to-batch differences due to insufficient control over the manufacturing process. For the past two decades, many government and non-government associations have tried to work out how to tackle this problem. Resulting from their work, the proposal to group or categorize nanomaterials for downstream risk and safety assessments has found large appreciation (Dekkers et al. 2016; Fadeel, Pietroiusti, and Shvedova 2017; Oomen et al. 2015). How to group nanomaterials will mostly be determined by their

toxicological profile or the underlying mechanisms thereof. However, it is at present still common to evaluate the safety of nanomaterials on a case-by-case basis due to the lack of standardized experimental data needed for establishing a grouping strategy. This is a time-consuming and costly procedure, which is especially undesirable in medicinal research. The most common grouping strategies (please refer to the following reflection papers of the European Medicines Agency (EMA) as provided in the References section: Data requirements for intravenous iron-based nano-colloidal products developed with reference to an innovator medicinal product; Joint MHLW/EMA reflection paper on the development of block copolymer micelle medicinal products;Reflection paper on surface coatings: general issues for consideration regarding parenteral administration of coated nanomedicine products; Reflection paper on the data requirements for intravenous liposomal products developed with reference to an innovator liposomal product; Reflection paper on nanotechnology-based medicinal products for human use.) are based on categorizing nanomaterials according to physicochemical properties, nanoparticle-cell interactions, exposure threats, or endpoint toxicity (Arts et al. 2015; Sayes, Smith, and Ivanov 2013; Simkó, Tischler, and Mattsson 2015). These strategies all target different aspects of nanomaterial toxicity and can provide vital information on the nature of nanomaterial-based toxicity. These approaches are often tailored to fit specific exposure risk scenarios of involuntary inhalation or voluntary oral ingestion (Bolt 2014; Gebel et al. 2014; Hadrup et al. 2015). Intentional therapeutic exposure upon injection on the other hand is only rarely referred to or even specifically ruled out of present grouping concepts (Arts et al. 2015). Yet, there are several reasons why the definition of such a strategy would be highly beneficial. First, for medical applications, where ENP formulations offer increasing therapeutic options, injection is the preferred route of administration. This route of administration leads to a defined and measurable exposure in contrast to inhalation or ingestion scenarios. Second, with the correct choice of biological models, it is possible to distinguish between intentional pharmacological effects (i.e. cytotoxicity as a MoA in cancer) and off-target effects. Third, with more than 75 FDA approved ENP, over 100 in clinical trials and hundreds more in research (Bobo et al. 2016; Witzigmann et al. 2015), the need for nano-specific regulation and safety assessment strategies for medical candidates is obvious.

2. Aim

It is the aim of the present work to provide a proposal for a novel hazard evaluation strategy to determine the safety of ENP designed for the use as injectable nano-pharmaceutics (Figure 2). It is important to note that inhalable and ingestible dosage forms were explicitly excluded from this study. Inhalables are based on particle size distributions that exceed the nano-range (Brown et al. 2013). Oral nanomedicines mostly consist of nanocrystals, which enhance solubility of poorly soluble drugs (Etheridge et al. 2013; Junghanns and Müller 2008). As they dissolve rapidly upon contact with gastric or intestinal fluids, these materials do not penetrate the body in the form of nanoparticles. Here, we propose a stepwise approach to assess the safety of nanomedicines (Figure 2). First, ENP are required to meet specific physicochemical properties to allow for their use as injectable nanoparticles (iNP). Second, a novel classification system divides selected candidates into hazard classes based on cellular uptake and intracellular persistence. Third, ENP are evaluated based on their safety classification using a distinct set of standardized toxicological assays as conducted by the US Nanotechnology Characterization Laboratory and European Nanomedicine Characterization Laboratory (USNCL and EUNCL, respectively). The US- and EUNCL assist the respective regulatory agencies (EMA and FDA) during the approval process of medical applications containing nanomaterials. Finally, the retrieved information serves a multitude of downstream processes such as safe-by-design, safety predictions, risk assessment, data mining, and grouping.

The three-tiered strategy allows us to identify suitable ENP for injection in an application-oriented and effective manner. Its structure could aid in minimizing the risk of adverse responses when moving from *in vitro* to *in vivo* testing as well as costly failures during later stages of their development. Our strategy is thus based on the International Organization of Standardization (ISO) definition of the term 'nanoparticle' and takes up a similar

classification approach as used, for example, in the Biopharmaceutics Classification System (BCS) to estimate the oral bioavailability of drugs (Amidon et al. 1995; ISO 2015). The concept uses standardized testing protocols from the USNCL and EUNCL to specifically assess the hazardous potential of ENP. Ultimately, the HES approach should promote an application-oriented decision-making process. It will contribute to informed and effective ENP hazard assessment and can be combined with future grouping strategies for read-across purposes.

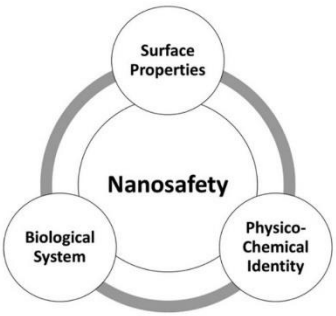

Figure 1. Nanosafety. Together with the biological system, the surface properties and physicochemical identity define the toxic potential of any engineered nanoparticle.

3. The hazard evaluation system for injectable nanoparticles (HES)

Approved nanomedicines designed for parenteral administration are very diverse with respect to their chemical identity, size, geometry, surface modifications, ζ-potential, and intended clinical uses. Very often, these formulations share certain physicochemical properties. They are mostly spherical or display an aspect ratio (AR) $\leq$ 3:1, have particle diameters below one micron (Buzea et al. 2007), and are stable as dispersions. However, this knowledge does not directly provide any information on the behavior or safety of an ENP after injection. ENP may provoke toxicity in a dose- and time-dependent manner upon interaction with biological systems. This includes, for example, recognition, phagocytosis or endocytosis, and processing of the immune system (macrophages) on a cellular level (Bartneck et al. 2010b; Sabella et al. 2014; Tiwari, Takashi, and Behari 2010; Weissleder, Nahrendorf, and Pittet 2014). On a whole-organism level, such interactions may lead to

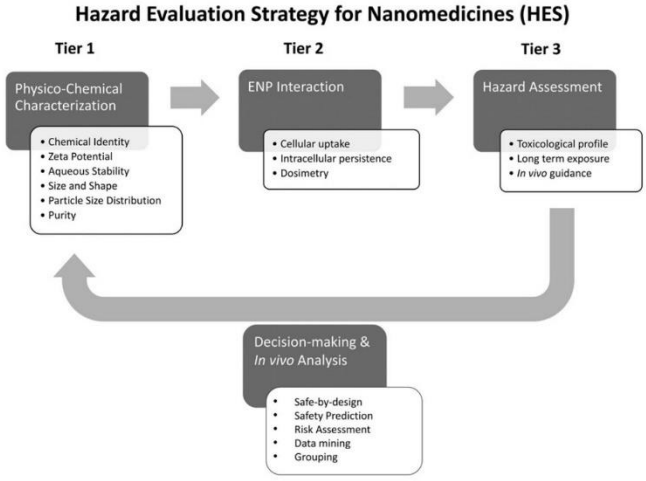

Figure 2. Hazard Evaluation System for Injectable Nanoparticles (HES). The HES hazard evaluation strategy is based on a three-tiered approach, which combines physicochemical characterization of engineered nanoparticles (ENP), ENP interaction, and hazard assessment. This test strategy can be used to (i) determine if a given ENP qualifies as a parentally administered medical application and (ii) identify potential safety issues of injected nanomedicines at early stages of their development. Furthermore, linking the findings from tiers 2 and 3 to the physicochemical properties determined in tier 1 can serve as the basis for *in vivo* testing strategies, risk assessment strategy set up and future grouping criteria. This will help to design and optimize ENP through safe-by-design principles and support personalized medicine initiatives.

augmented circulation time, accumulation, retarded clearance, off-target interactions, organ damage, and chronic adverse effects. We strongly believe that the two key factors, directly providing preliminary information on these biological interactions and the ensuing *in vivo* consequences, are cellular uptake (Oh and Park 2014; Yameen et al. 2014) and intracellular persistence (Laux et al. 2017; Lee et al. 2013). High uptake and high persistency may trigger inflammatory events (Fadeel et al. 2017; Kennedy, Wilson, and Barakat 2009). Low quantities of ENP uptake by cells other than macrophages and low intracellular persistency over time is indicative of limited biological interactions. In the latter case, phagocytosis by macrophages (Bartneck et al. 2010a) or extracellular events such as platelet aggregation or complement activation should be closely monitored. Due to the possibility of linking physicochemical properties with nanoparticle-cell interactions *in vitro*, the risk of provoking adverse effects *in vitro* and *in vivo* (e.g. toxicity or elimination) can be minimized significantly.

The Hazard Evaluation System for Injectable Nanoparticles (HES) was designed as a concept to specifically test the suitability of ENP as injectable pharmaceutics. The three tiers – as shown graphically in Figure 2 – are physicochemical characterization (1), ENP interaction (2), and hazard assessment (3).

The ENP are physicochemically characterized before progressing to *in vitro* toxicity studies. Following the characterization, cellular uptake and intracellular persistence of the formulations are determined to categorize them into hazard groups for more detailed hazard assessment. Dedicated hazard assessment processes designed for every group ensure the recognition of hazardous potential associated to a pharmaceutical candidate. Every tier includes specific assays, measuring techniques, controls and definitions that are discussed in detail in the following sections. Formulations failing to meet the requirements of tier 1 to tier 3 are not further considered in the HES approach and are required to proceed in case-by-case evaluations. Such formulations are not necessarily considered unfit as injectable pharmaceutics; however, due to their innovation or unconventional characteristics represent classes of formulations where vital information is still lacking. Thus, the safety of these candidates must be evaluated case-by-case until enough data are acquired in order to expand the HES framework or separately establish a novel testing strategy. An important component of the proposed concept is the retrospective analysis of results (decision-making and *in vivo* analysis, Figure 2). Data mining and data analysis will offer the possibility to perform informed safety predictions and to implement grouping and modeling strategies. Such a rational approach will be the basis for future safe-by-design strategies.

3.1. Tier 1: Physicochemical characterization

In the first tier of the HES, the candidate materials enter a defined physicochemical characterization cascade (see flowchart Figure 3). The cascade serves as a systematic preselection sequence, in which ENP are tested according to six criteria: chemical identity, ζ-potential (zeta potential), aqueous stability, shape, size and size distribution, and contamination. Depending on the outcome of this initial screen, an ENP either qualifies to be further investigated in the HES or must yet undergo a 'case-by-case' safety assessment, as mentioned earlier. The chemical identity, ζ-potential, and aqueous stability of an ENP are not directly a safety issue in most cases. Nevertheless, knowing these three parameters is a prerequisite for their further experimental assessment. Having this knowledge beforehand can give insight into how an ENP sample behaves in dispersion, or in what manner it may interact with buffers or biological fluids. A formulation that fulfills all physicochemical requirements (as summarized in Figure 3**)** also fits the physicochemical definition of an injectable nanoparticle and can therefore enter tier 2 of the HES.

Each one of the basic physicochemical properties of ENP should be measured using a standardized protocol. For the HES, we propose to use the written and recommended protocols of either the USNCL or the EUNCL. Both US- and EUNCL work together with the FDA or the European Medicines Agency (EMA), respectively. Furthermore, both NCL institutions do not only act as advisors to regulatory agencies but also provide assistance for small and medium-sized enterprises, spin-offs and newcomers towards nanomaterial characterization and product submission approvals. This assures that the assay

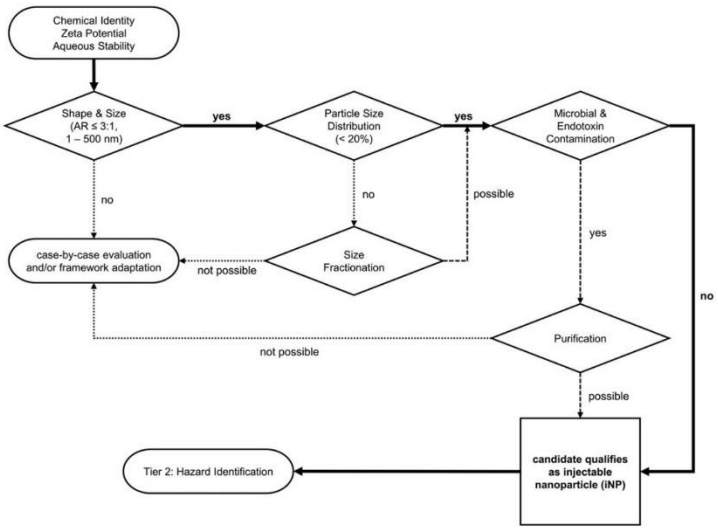

Figure 3. Physico-chemical characterization of nanoparticle properties. The physicochemical characterization of ENP represents tier 1 of the Hazard Evaluation System for Injectable Nanoparticles (HES). After the chemical identity, ζ-potential, and aqueous stability are determined, size, particle size distribution, and purity are examined. In this step-by-step approach, an ENP either moves on through the HES cascade or its safety has to be evaluated separately case-by-case depending on the results obtained during characterization. A candidate passing the entire cascade (Tier 1) qualifies as an injectable nanoparticle according to the HES guideline and moves on to ENP interaction (Tier 2, Figure 4). AR: Aspect Ratio.

protocols are well in-line with current testing standards and are re-evaluated on a regular basis.

In addition, proposals for alternative measurement techniques are provided as well. These techniques are not used by the US- or EUNCL but find much appreciation throughout their respective research fields. Furthermore, not all techniques suggested by the NCLs are available as a standard in every laboratory. References to selected protocols are listed in the appropriate sections of this publication.

3.1.1. Chemical identity

The chemical identity of an ENP should be assessed first as it may have an impact on the setup of further experiments regardless if the ENP is the active agent or its carrier system. Should any chemical contaminations (e.g. synthesis residues) be detected during the assay, it is strongly advised to purify the formulation before advancing further in tier 1 (Garbovskiy 2017). Batch-to-batch variability should be held as low as possible and must be recorded for at least three independently manufactured formulations.

Different analysis techniques can be used to gain information on the chemical identity of an ENP. The most commonly used technique is Inductively Coupled Plasma Mass Spectrometry (ICP-MS) (Fabricius et al. 2014). With ICP-MS entire samples or single nanoparticles (detection limit in nanogram per liter range) can be analyzed in very short time and high precision. Furthermore, ICP-MS can be coupled to several analytical separation methods whereby speciation and quantification measurements can also be performed. The USNCL provides four different protocols on how to characterize the chemical identity of nanomaterials all including ICP-MS techniques (USNCL-PCC-8, USNCL-PCC-9, USNCL-PCC-11, and USNCL-PCC-14). As an alternative, different techniques including High Performance Liquid Chromatography (HPLC) are also being used to analyze nanomaterials that are mainly carbon, or nonmetal based (Álvarez-Fuentes et al. 2012; Itoh et al. 2016).

Alternatively, Nanoscale Fourier-Transformation Infrared Spectroscopy (nano-FTIR) can also be used to determine the chemical identity of nanoparticles

(Huth et al. 2012). Fourier-Transformation Infrared Spectroscopy (FTIR) is commonly used in chemistry to identify chemical structure of materials or to verify the chemical purity of a synthesis product. Nano-FTIR is a combination of FTIR and scattering-type Scanning Near-field Optical Microscopy (s-SNOM) based on Atomic Force Microscopy (AFM) in non-contact mode. The technique allows measurements on ultra-small probe quantities with a spatial resolution of 10 nm–20 nm. Nano-FTIR has already been successfully used to identify polymers and nanocomposites or in investigations regarding the elucidation of secondary protein structures as well as bacterial membranes (Amenabar et al. 2013).

Another important technique is the Microscale Thermogravimetric Analysis (μ-TGA). It is used to characterize the surface coating and purity of nanoparticles, especially when they are introduced to a biological environment (Mansfield et al. 2014). This method is very sensitive and can be used to determine the amount of coating on the nanoparticle surface. These experiments are done in an inert atmosphere at temperatures over 1000 °C (Dongargaonkar and Clogston 2018).

Alternatively, quantitative NMR can be used to characterize nanoparticles to reveal structural and dimensional information. Especially the coatings can be analyzed to explore characteristics like the ligand density on the surface (Guo and Yarger 2018).

3.1.2. Aqueous stability and ζ-potential

The lack of aqueous stability provokes agglomeration and sedimentation, which may trigger immune responses such as phagocytosis, generation of reactive oxygen species (ROS), or inflammatory reactions. Moreover, agglomeration-flocculates can sediment and in extreme cases could clot capillaries causing mechanical distress and serious pain. Since there is no generally accepted protocol on the measurement of ENP stability, the authors propose the following: *'The aqueous stability of ENP should exceed the duration of the longest tests proposed in the tiers of the hazard evaluation strategy (HES). We therefore propose that ENP dispersions should not display any significant changes in particle size, shape, and particle size distribution over the course of at least one week, at a defined pH and at 37 °C using a physiological buffer system.'*

However, depending on specific project requirements and application needs, this basic protocol can be adjusted to a specific time frame (e.g. short-term application) or for factors that can affect the stability profile, such as the mechanism of the payload delivery or surface modifications. Furthermore, additional test might be needed to demonstrate prolonged stability during storage at room temperature or at 4 °C in a specific container (e.g. plastic infusion bag or glass vials). It should also be noted that the stability of an ENP may change after dispersion in biological fluids (Aguilar-Castillo et al. 2015; Moore et al. 2015). Thus, performing stability measurements in biological fluids may yield valuable information as well and should be carried out. Aqueous stability measurements follow the same protocols used for particle size, shape, and particle size distribution. Method descriptions and protocols are covered in detail by the appropriate standardized protocols (see Section '3.1 Tier 1: Physicochemical characterization').

The aqueous stability of any nanomaterial dispersion is often related to the surface charge (ζ-potential) of the nanoparticle. For this reason, ζ-potentials of ENP should be measured prior to analyzing their aqueous stability (Bhattacharjee 2016). Formulations that display positive or negative ζ-potentials are generally considered to be stable in water whereas nanoparticles with a ζ-potential near neutral tend to agglomerate (Clogston and Patri 2011). It should, however, be noted that highly positive charged particles have the potential to be acute cytotoxic (Dobrovolskaia et al. 2012). On the other hand, ζ-potential values directly depend on the pH of nanoparticle dispersions as pH influences protonation and deprotonation of the nanoparticles (Berg et al. 2009). Thus, ζ-potentials should always be determined at pH values that resemble the ones of the ENP storage solutions and ideally represent physiological conditions (i.e. ideally above 30 mV or below −30 mV). The protocols ensuring correct measurements of ζ-potentials and pH are referenced as USNCL-PCC-2 and USNCL-PCC-13, respectively. The preferred ζ-potential measuring technique is electrophoretic light scattering (ELS) whereas pH is predominantly measured with semi-micro combination pH electrodes.

3.1.3. Shape

The International Standards Organization (ISO) provides definitions for the terms nanomaterial, nanoobject, nanofiber, nanoplatelet, and nanoparticle based on their external and internal dimensions. In this sense, external dimensions describe length, width, and height of a material whereas surface structures (e.g. pores) and internal structures are acknowledged as internal dimensions (ISO 2015). As an exclusion criterion, the HES approach considers external dimensions of ENP only, yet taking into account that internal dimensions may well influence stability or the MoA.

As mentioned before, most commercially available nano-pharmaceutics are spherical in shape or have an aspect ratio of $\leq$3:1. Therefore, only nanoparticles that display an aspect ratio (AR) $\leq$3:1 are considered for further investigations in the HES. So called high aspect ratio nanomaterials (HARN) (Oberdörster, Stone, and Donaldson 2007) are excluded from the process. This includes the fiber-like single or multiwalled carbon nanotubes (SWCNT or MWCNT, respectively). Although these nanomaterials are at present heavily studied, they show typical signs of complications associated to HARN. HARN may inflict mechanical cell or tissue damage often due to rigidity and size (e.g. leading to frustrated phagocytosis). Moreover, their geometry bears a higher risk of recognition by the immune system. Considering these facts, HARN are not ideal nanomaterials for parenteral applications and have not been used as such up to date. Consequently, HARN are also excluded from the HES and must be evaluated on a case-by-case basis.

Transmission Electron Microscopy (TEM) (Pyrz and Buttrey 2008), Scanning Electron Microscopy (SEM) (Goldstein et al. 2014), and cryoEM (Crawford et al. 2011) are commonly used to study the shape of nanoparticles. The chemical identity of a nanoparticle dictates which of these techniques should be applied. The procedures using TEM and SEM can be carried out according to the protocols USNCL-PCC-7 and USNCL-PCC-15, respectively. Additionally, the EUNCL provides a protocol for cryoEM analysis (EUNCL-PCC-20).

3.1.4. Particle size

Particle size is arguably the most important characteristic in the first HES tier since various definitions of the term 'nanoparticle' are based entirely on primary particle size. We propose the implementation of a novel size range specifically suiting ENP designed for injection. Such candidates normally cover a size range of 1–500 nm rather than the regulatory definition of 1–1000 nm. Candidates averaging sizes below 1 nm or above 500 nm are subjected to case-by-case evaluations and are excluded from the HES.

We feel that, in this particular case, the novel ENP size range of 1 nm to 500 nm is a valid alternative to existing definitions of the International Standards Organization (ISO), the Organization for Economic Co-operation and Development (OECD), the European Commission, the US Environmental Protection Agency, or regulatory authorities in charge of pharmaceuticals. In many cases, nanoobjects are defined by a size of approximately 1– 100 nm (often referred to as the nanoscale) (ISO 2015; Krug and Wick 2011; Potočnik 2011; Serpone and Horikoshi 2013). The lower limit of 1 nm was set to specifically exclude single atoms and small atom groups. The upper limit of 100 nm was set to emphasize on the existence of so called 'quantum size effects' (Boilard et al. 2013; Krug and Wick 2011; Zhang et al. 2009) often originating from band-gap differences directly influenced by particle size (Chukwuocha, Onyeaju, and Harry 2012). Due to their submicron size, ENP may thus display unique characteristics that their bulk counterparts lack completely. The National Nanotechnology Initiative (NNI) states that quantum effects are size driven and in turn govern the behavior and properties of nanomaterials (NSCT/CoT/NSET 2014). A number of properties such as fluorescence, electrical conductivity, magnetic permeability, and chemical reactivity are affected when particles stay below the critical size of 100 nm (Navya and Daima 2016; Uskoković 2013). However, this 100 nm cutoff value remains controversial, for different reasons. Numerous regulatory organizations feel that the present justification of the upper size limit (100 nm) is not scientifically appropriate and should be extended with more qualifiers (such as particle size distribution and spatial dimensions) (Jong 2010; Lovestam 2010; Potočnik 2011). Additionally, it has been acknowledged that health and safety aspects with nanomaterials do not abruptly end at 100 nm (ISO 2015). In view of these debates and the

growing interest in pharmaceutical and medical nano-applications, the FDA has considered an augmentation of the upper scale limit to 1000 nm (FDA 2005). Most other regulatory authorities have also adopted this scale enlargement over the past years. However, the FDA also states that setting the cutoff at one micron is not at all trouble-free as this size incorporates an even greater palette of diverse materials (e.g. pigments, quartz, sand). The FDA, therefore, states that it might be beneficial not to cover all nanomaterials within one definition but rather set definitions according to the applicatory field of the material in question (FDA 2005).

Taking these facts into account, the HES size definition for injectable nanoparticles was considered to be appropriate for medical regulation purposes. The lower limit of the HES size definition (i.e. 1 nm) is based on widely accepted nanoparticle definitions from authorities and regulatory bodies whereby atoms and small molecules are excluded. Its upper limit (i.e. 500 nm) newly considers the activity of immune cells and their ubiquitous presence in the vasculature system. It is generally accepted that uptake of intact nanoparticles through cell membranes is mediated by active transport (e.g. receptor mediated endocytosis) (Zhang et al. 2009). These uptake routes depend on particle size. Objects smaller than 500 nm are readily internalized via different types of endocytosis (e.g. clathrin versus caveolin-mediated transport) (Champion, Katare, and Mitragotri 2007; Kettiger et al. 2013). However, objects larger than 500 nm mostly lack this ability and are prone to be predominantly exposed to phagocytosis, which is an immune cell-specific process (Aderem 2003). Therefore, limiting ENP size to 500 nm rules out size-dependent involvement of immune cells in cellular uptake of ENP or immune mediated reactions. Finally, since injectables are not designed to trigger phagocytosis, the upper size limit of 500 nm in the HES definition of an iNP was chosen.

Alternatively, some nanoparticles are designed to be fusiogenic (e.g. cationic liposomes). For example, liposomes with integrated lipopeptides in the bilayer were able to fuse with plasma membranes and to empty their cargo into the cytoplasm of their target cells (reviewed by Li et al. (2017)). Under such conditions, active transport will not be involved and the mentioned size definitions have to be adjusted.

Size measurements must be interpreted with caution since the term 'particle size' is often used interchangeably to describe the primary particle size as well as the hydrodynamic diameter of an ENP. Primary particle size denominates the true particle diameter, whereas the hydrodynamic diameter takes the first layer of solvent into account as well (Hackley and Clogston 2011). Hence, the hydrodynamic diameter should always be larger than the primary particle diameter and is therefore the decisive parameter when it comes to the discussed size limitations. Nevertheless, both parameters should be measured as either one can have an impact at later stages of the HES. The standard methods to measure hydrodynamic diameters of ENP are based on the technique of Dynamic Light Scattering (Kaszuba et al. 2008) (DLS, protocol USNCL-PCC-1). Here, Nanoparticle Tracking Analysis (NTA) (Hole et al. 2013; Maguire et al. 2017; Mehn et al. 2017) is frequently used as an alternative method. Atomic Force Microscopy (Rao et al. 2007) (AFM, protocol USNCL-PCC-6) and TEM (Pyrz and Buttrey 2008) (protocol USNCL-PCC-7) are typically used to determine primary particle sizes. Other techniques that are used to describe primary particle sizes include: Small-Angle X-Ray Scattering (SAXS) (Li, Senesi, and Lee 2016; Vippola et al. 2016) and electrospray differential mobility analysis (ES-DMA) (Guha et al. 2012).

3.1.5. Particle size distribution

The Scientific Committee on Emerging and Newly Identified Health Risks (SCENHIR) sub-categorizes nanoparticles into three categories depending on the range of particle size distributions. In contrast, we propose a more stringent approach. It demands particle size distributions to be as narrow as possible (Jong 2010). In physiological buffer, a particle size distribution limit of 20% or a polydispersity index value (PDI) of <0.2 based on an intensity-based Z-average diameter value is proposed. This limit is chosen because a PDI of <0.2 is considered to reflect monodispersity (Panchal et al. 2014; Roberson and Weltje 2014). However, the viscosity and refractive index of the solvent, ionic strength of the media, temperature, concentration of ENP,

handling of ENP (e.g. filtration, sonication) should be considered for comparing different PDI values across studies. It should be noted that a PDI <0.2 for parenteral applications might be smaller than the corresponding value defined for other therapeutic applications. For example, for dermal delivery of liposomes, a PDI <0.3 has been deemed acceptable to reflect monodisperse ENP-drug preparations. In addition, the PDI will change in presence of proteins due to protein adsorption or the presence of protein agglomerates. If the condition of monodispersity is not fulfilled, size fractionation (Akthakul et al. 2005; Robertson et al. 2016) or filtering (Droppo 2006) may be used to narrow down the particle size distribution of particle populations. The method of choice to determine hydrodynamic particle size distributions and polydispersity is DLS according to protocol USNCL-PCC-1. In addition, true particle size distributions of ENP should be confirmed by SEM and TEM (FDA 2005; Jong 2010; Lovestam 2010).

3.1.6. Microbial contamination and endotoxins

A well-known issue with ENP submitted for pharmaceutical or medical approval is purity (Li and Boraschi 2016). The presence of impurities is the most common reason regulatory bodies neglect pharmaceutical formulations or applications during the approval sequence. Purity refers to the absence of chemical or biological contamination. As chemical impurities must be checked for and identified previously during the analysis of the chemical identity; this step of the HES focuses on biological contamination (i.e. bacteria, mycoplasma, or endotoxin). The USNCL defines a number of assays to assess contamination levels of nanomaterials. At least endotoxin (USNCL-STE-1.1 until 1.4), bacterial (USNCL-STE-2.1 and 2.2), and mycoplasma contaminations (USNCL-STE-3) should be monitored. Purity is an intrinsic property of any iNP. In case of the presence of contaminants, ENP should be sterilized and depyrogenized by using standard techniques such as autoclaving, filtration, or gamma-irradiation (Li et al. 2013; Vetten et al. 2014; Zheng et al. 2011). If, however, impurities are still detected thereafter, which cannot be removed by a modified production process, the candidate falls out of the HES and must be further assessed in a case-by-case evaluation. Because standard sterilization techniques can influence the stability and physicochemical properties of ENP, it must be ensured that the properties of postprocessed ENP are not significantly changed.

3.1.7. Physicochemical definition of an injectable nanoparticle (iNP)

The physicochemical definition of an iNP takes all the previously discussed issues into account and summarizes tier 1 of the Hazard Evaluation Strategy for Injectable Nanoparticles (HES) as follows: *'An injectable nanoparticle (iNP) is defined as a nanoparticle measuring between 1 nm to 500 nm in all three external dimensions (height, length, width), whereas the length of the longest to the shortest axis of the nanoparticle do not differ by more than three-fold (aspect ratio 3:1). Additionally, iNP particle size distributions should be below 20% (polydispersity indices of <0.2) as determined in a physiological buffer system. Also, the aqueous stability should not be affected over the course of 7 days when measured at a distinct pH and 37 °C. Finally, an iNP must be endotoxin-free and should not show chemical, bacterial, or mycoplasma contamination.'*

3.2. Tier 2: ENP interaction

In the second tier of the HES, a novel classification system divides iNP into four different risk categories depending on two biological readouts, which are linked to particle persistence in biological systems and cellular exposure. In this novel ENP interaction concept (Figure 4), iNP are grouped according to the criteria of cellular uptake and intracellular persistence. We propose that these two parameters are key for iNP safety in circulation. In the HES plot, the intensity of cellular uptake and intercellular persistence increases from the top left to bottom right quadrant of the plot. This does not generally imply that high uptake and persistence of iNP bear the highest risk for a patient. Depending on the intended use of the iNP, high uptake and persistence are part of the MoA. Yet, the multitude of possible adverse effects is augmented when uptake and persistence are high. Consequently, iNP grouped into category IV necessitate a more detailed safety assessment as compared to iNP

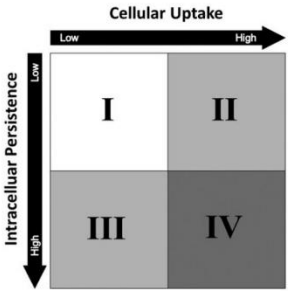

Figure 4. The HES ENP interaction. The HES ENP interaction divides nanoparticles into four different groups. The grouping strategy is based on cellular uptake and intracellular persistence of an iNP. By monitoring these two parameters, distinct hazard assessment strategies can be designed for individual ENP interaction groups. As a general rule, the higher the category the higher the number of possible hazards and thus the number of required safety assessments. It should be noted that the generation of ROS or an involvement and activation of the immune system has a major impact on the interpretation of the HES classification. For example, humoral responses mediated by the complement system may lead to hemolysis and platelet aggregation. Cellular immune responses may lead to particle depletion.

falling into lower risk categories (Category IV < III < II < I).

Neither USNCL nor EUNCL provides standardized protocols for measuring cellular uptake or intercellular persistence as this does not lie in the scope of their work. Therefore, experimental methods are proposed in the following sections to address these issues.

3.2.1. Cellular uptake

The techniques to measure cellular uptake can vary depending on the type of iNP and the availability of analytical technologies. Ideally, confocal-, dark-field-, and EM-microscopy (qualitative assessment) can be combined with flow cytometry, HPLC, single particle or single cell ICP-MS, or a combination of the latter techniques (quantitative assessment). The prerequisite for quantitative assessments is, however, knowing the initial administered dose. After a desired incubation time, the quantity of iNP and their residues is measurable in the supernatant as well as in the cell sample. This enables determining the quantity of iNP taken up. Measurements should be performed at time points 30 min, 4 h, 8 h, and 24 h. The indicator for low cellular uptake would then be defined as any quantity of iNP taken up in the first 8 h of incubation being below a certain cutoff value (percentage of total iNP dose). Alternatively, high cellular uptake levels would be represented by any quantity of iNP taken up in the first 8 h of incubation exceeding that same cutoff value. With this respect, erythrocytes may serve as negative control (minimal uptake) and macrophages as positive control (maximal uptake).

Cellular uptake of iNP should be monitored in the cell type, which is most likely to interact first with iNP after injection. After intravenous injection of iNP, for example, these are vascular endothelial cells as they line the blood vessels and the lymphoid system (Félétou 2011). Endothelial cells are known to readily take up nanoparticles (in contrast to, e.g. erythrocytes) (Siegrist et al. 2017). This can lead to severe cytotoxic effects that in turn damage the vascular system and potentially the tissue residing behind it, causing complications and pain in the patient. Furthermore, the endothelium acts as a semi-selective barrier and co-controls the migration of white blood cells into and out of the blood stream (Yuan and Rigor 2010). Endothelial dysfunction plays, therefore, a pivotal role in vascular diseases (Deanfield et al. 2005) and is often regarded as the early trigger of events such as arteriosclerosis (Davignon and Ganz 2004). We, therefore, believe that monitoring endothelial uptake of iNP *in vitro* provides essential information on endocytosis and cellular clearance of iNP. Intended target cells of the iNP should be excluded from these measurements, since the focus of these experiments is an ENP interaction in non-target cells. While the exact structure of the biocorona is controversially discussed (e.g. existence and relevance of a 'soft' protein corona), the detailed composition is very variable and highly fluctuating over time even *in vitro* (Casals et al. 2010; Docter et al. 2015). Furthermore, recent studies show that proteins adsorbed to nanoparticles *in vitro* are rapidly exchanged *in vivo* (Chen et al. 2017). Although, in the future, *in vitro* tests might permit to predict the role and influence of the biocorona *in vivo*, currently our understanding and ability of extrapolating the impact from *in vitro* to *in vivo* is insufficient. Therefore, future tests assessing the biocorona of nanoparticle might complement our test strategy.

For protein interactions of biomedical applied nanoparticles, see Shannahan (2017). This topic is further reviewed by Treuel et al. (2015), Ke et al. (2017), and Neagu et al. (2017).

3.2.2. Intracellular persistence

Intracellular persistence is monitored in the same cell type, preferably even in the same sample, as cellular uptake. The first measurements should be performed 8 h and 24 h after incubation, thereafter once every 24 h for a week. In the sense of a precautionary approach, low intracellular persistency is defined if the amount of iNP taken up after 24 h decreases by 80% until the fifth day of the measurement. High intracellular persistence is given, if less than 80% of the iNP taken up in the first 24 h has been degraded.

Measuring intracellular persistence can either be performed by confocal and EM microscopy or ICP-MS (Lee et al. 2013). While microscopy techniques will only yield qualitative results, ICP-MS allows for quantitative analyses. However, cellular samples are destroyed under ICP-MS in contrast to microscopy techniques. It should be emphasized, that intracellular persistence is not equivalent to chemical or colloidal stability as it is being tested for in tier 1 of the HES. Even though the two parameters can certainly be linked, the ability of an organism to degrade or eliminate an iNP underlies different and often more complex mechanisms than particle agglomeration or disintegration in aqueous solution.

Experimental results on cellular uptake are expected to be dose- and time-dependent. They are not only closely related to the number of nanoparticles taken up, but can vary depending on the capacity of cells to degrade or eliminate them after uptake. Thus, intracellular persistence correlates to intracellular accumulation and exposure. It is therefore expected that adverse effects gain in severity with increasing levels of uptake and persistence, in particular if iNP are administered repeatedly.

3.2.3. Dosimetry and dose

It is important to note that correct dosimetry is paramount for any type of nanosafety evaluation and ENP risk assessment (Teeguarden et al. 2007). Cellular uptake, intracellular persistence, and toxicity are in most cases dose-dependent. For *in vitro* studies on nanoparticles, appropriate doses range from ng/ml to µg/ml (Siegrist et al. 2017). To translate the dose-range from *in vitro* and *in vivo* experiments to humans (human equivalent dose, HED), no-observed-adverse-effect-level (NOAEL) values from corresponding animal experiments are used. The animal-derived NOAEL is multiplied with a conversion factor (k_m), which is different for each species. It is based on the body surface area and is set by the FDA. After calculating the HED, a maximum recommended starting dose (MRSD) is evaluated. Dividing HED values by a safety or uncertainty factor (often a factor of 10) is the common procedure to calculate an MRSD and reduce the risk of possible adverse effects in humans. The MRSD is given in milligrams per kilogram body weight (mg/kg), which can be reproducibly calculated for each individual (FDA 2005; Nair and Jacob 2016). Table 1 highlights the maximum recommended dose and route of administration of selected nanomedicine formulations approved by the FDA. The given doses correspond to the highest recommended dose for a person weighing 60 kg with a body surface area of 1.69 m^2. For reasons of completeness, nanocrystals – which are administered at very high doses – are also listed in Table 1. However, these oral dosage forms cannot be designated as iNP based on criteria of the HES as discussed in previous sections. Nevertheless, therapeutic doses of injectable nanomedicines typically cover three orders of magnitude depending on the indication, as the selection of approved nanomedicines in Table 1 shows.

In accordance with regulatory guidelines on pharmaceutical applications, we therefore recommend that a no-observed-adverse-effect-level (NOAEL) as well as a maximum recommended starting dose (MRSD) specifically for iNP should be established routinely. Nano-specific HED and k_m values should be calculated on a case-by-case basis considering the unique toxicological profile of nanoparticles and their intended clinical application. This should be done for the final formulation, which will be administered to the patient. If the preclinical formulations substantially differ from the final product formulations, the previously measured values should be updated. We recommend that for injectable nanomedicines, the dose units should uniformly be given in mg/kg (rather than U/kg or mg/

Table 1. Applied doses of FDA approved nanomedicines. Dose, dosing interval, administration route(s), and supplement size of selected FDA approved nanomedicines.

Name (Company), Year of approval	Dose	Interval	Administration	Supplement size
Selected examples of inorganic based injected nanoparticles				
Feridex®/Endorem® (AMAG pharmaceuticals), 1996 (2008)	0.65 mg/kg	Once	i.v.	56 mg/5 ml
Ferrlecit® (Sanofi Avertis), 1999	2.1 mg/kg	Once	i.v.	62.5 mg/5 ml
Feraheme®/ferumoxytol (AMAG pharmaceuticals), 2009	8.5 mg/kg	Twice a week	i.v.	510 mg/17 ml
Venofer® (Luitpold Pharmaceuticals), 2000	16.7 mg/kg	Once	i.v.	100 mg/5 ml, 200 mg/10 ml
INFeD® (Sanofi Avertis), 1957	45.9 mg/kg	Once	i.v.	100 mg/2 ml
Selected examples of injected nanocrystals				
Abraxane®]/ABI-007 (Celgene), 2005, 2012, 2013	7.7 mg/kg	Every 3 weeks	i.v.	100 mg/20 ml
Ryanodex® (Eagle Pharmaceuticals), 2014	11.7 mg/kg	Once	i.v.	250 mg/5 ml
Selected examples of lipid based injected nanoparticles				
Marqibo®\ (Onco TCS), 2012	67.7 μg/kg	Weekly	i.v.	5 mg/31 ml
Visudyne® (Bausch and Lomb), 2000	0.18 mg/kg	Once	i.v.	15 mg/7 ml
AmBisome®\ (Gilead Sciences), 1997	0.82 mg/kg	Daily	i.v.	50 mg/10 ml
DaunoXome® (Galen), 1996	1.2 mg/kg	Every 2 weeks	i.v.	50 mg/25 ml
Onivyde® (Merrimack), 2015	2.1 mg/kg	Every 2 weeks	i.v.	43 mg/10 ml
Doxil®/Caelyx® (Janssen), 1995, 2005, 2008	1.5 mg/kg	Monthly	i.v.	20 mg/10 ml, 50 mg/30 ml
DepoDur® (Pacira Pharmaceuticals), 2004	0.25 mg/kg	Once	lumbar-epidural	10 mg/ml
DepoCyt® (Sigma Tau), 1996	0.83 mg/kg	Every 2 weeks	intrathecal	50 mg/5 ml
Curosurf®/Poractant alpha (Chiesei farmaceutici), 1999	2.9 mg/kg	Once	intratracheal	120 mg/1.5 ml, 240 mg/3 ml
Selected examples for injected polymeric drugs				
Mircera®/Methoxy polyethylene glycol-epoetin beta (Hoffman-La Roche), 2007	0.7 μg/kg	Every 2 weeks	s.c. or i.v	50–1000 μg/ml
PegIntron® (Merck), 2001	1.8 μg/kg	Weekly	s.c.	50–150 μg/0.5 ml
Cimzia®/certolizumab pegol (UCB), 2008, 2009, 2013, 2013	6.7 mg/kg	Monthly	s.c.	200 mg/ml
Oncaspar®/pegaspargase (Enzon Pharmaceuticals), 1994	0.88 mg/kg	Every 2 weeks	i.m. or i.v.	3750 U/5 ml (> 85 IU/kg)
Macugen®/ Pegaptanib (Bausch & Lomb), 2004	5.0 μg/kg	Every 6 weeks	intravitreal	0.3 mg/ml
Selected examples for oral or dermal applied nanoparticles or polymeric drugs				
Zanaflex® (Acorda), 2002	66.5 μg/kg	3x daily	oral	2 mg, 4 mg, 6 mg capsules 4 mg tablets
Megace ES® (Par Pharmaceuticals), 2001	10.4 mg/kg	Daily	oral	625 mg/ 5 ml
Estrasorb® (Novavax), 2003	58 mg/kg	Daily	topical	4.35 mg/1.74 g foil

Highest recommended doses are shown and are normalized to 60 kg body weight and 1.69 m^2 body surface area (FDA, 2005).
The supplement size shows the amount of drug per sample unit.
Therapeutically used doses vary by three orders of magnitude.
i.m.: intramuscular; s.c.: subcutaneous; i.v.: intravenous.

m^2) as proposed in 2005 by the FDA for initial clinical trials (FDA 2005).

3.3. Tier 3: Hazard assessment

As described in Figure 4, the ENP interaction system of iNP is subdivided into four categories that depend on uptake and persistence.

- Category I – low cellular uptake and low intracellular persistence
- Category II – high cellular uptake and low intracellular persistence
- Category III – low cellular uptake and high intracellular persistence
- Category IV – high cellular uptake and high intracellular persistence

The assignment of an iNP to one of the four HES risk categories (Figure 4) dictates which set of assays must be performed to assess the safety of the formulation in question. As the four categories are related to possible adverse outcomes, the assay cascades become more elaborate with increasing uptake and persistence of the iNP. However, this does not necessarily suggest increasing levels of nanoparticle toxicity: For example, an iNP in category II may show greater toxic potential than a counterpart entering category IV. We propose eight different parameters in total, which should be monitored throughout hazard assessment. These parameters cover complement activation, platelet aggregation, hemolysis, oxidative stress, cell viability, phagocytosis, inflammation, and DNA damage. An overview of assays recommended by the USNCL or the EUNCL is given in Table 2. This includes measurement technique, assay type, specific category affiliation, and a protocol reference. It should be noted that the incorporation of different toxicogenomics techniques such as genomics, proteomics, and metabolomics may complement or eventually replace a number of biochemical or cell based assays mentioned in Table 2 since there is a growing interest in these approaches in the nanosafety community (Fröhlich 2017). In general, the HES approach is highly dependent on the selection of specific assays and endpoints that best represent the critical hazard criteria that are relevant to the *in vivo* situation. Therefore, the approach should provide some flexibility in revisiting and updating the specific subsets of assays as the science evolves.

The most common routes of administration summarized under the term injection are intravenous, subcutaneous, and intramuscular. Complement activation, platelet aggregation, and hemolysis are risks associated with intravenously injected iNP. Such adverse effects are less likely if iNP are not in direct contact with the lymphoid system and bloodstream (Turner et al. 2011). Nevertheless, we believe it is important to test for these events routinely for any

Table 2. Hazard assessment portfolio. This table shows the nine possible parameters that can be determined in the HES Tier 3.

Target	Assay	Technique	Risk category	Protocol
Present techniques				
Complement activation	Antibody presentation	ELISA	Category I – IV	USNCL-ITA-5.1 EUNCL-ITA-005.2
Platelet aggregation	Whole blood assay	Bioassay	Category I – IV	EUNCL-ITA-02.1 EUNCL-ITA-02.2
Hemolysis	Colorimetric assay	Spectroscopy	Category I – IV	EUNCL-ITA-01
Cell viability	MTT	Spectroscopy	Category I – IV	EUNCL-GTA-01
	WST8	Spectroscopy		USNCL-GTA-2
Phagocytosis	THP-1 uptake	Spectroscopy Microscopy	Category I, III, IV	USNCL-ITA-9
Oxidative stress	DCF-HA	Flow Cytometry	Category II, III, IV	USNCL-ITA-7 USNCL-GTA-3
Cytotoxicity	LDH	Spectroscopy		USNCL-GTA-4 USNCL-GTA-7
DNA damage	Micronucleus assay, Ames assay, COMET assay	Microscopy, Spectroscopy	Category III, IV	OECD
Inflammation	ELISA	Microarray	Category IV	EUNCL-ITA-10
	NFk-B, STAT, CD34	Western Blot		EUNCL-ITA-30
	MHC I / MHC II	Flow Cytometry		EUNCL-ITA-31
Future techniques				
Unbiased approaches	Genomics, Proteomics, Metabolomics	Screening and sequencing	Category II-IV	*Under evaluation for regulatory purposes*

According to the risk category and injection type, a subset of assays is selected for hazard assessment of a given iNP.
All assay protocols (except for DNA damage) listed in this table are validated and approved by the US NCL or the EU NCL.
Novel unbiased approaches are at present under evaluation for regulatory purposes.

type of iNP-injection based on the observations that platelet aggregation and complement activation can be observed after s.c. (Ermidou-Pollet et al. 2005) and i.m (Atkinson, Taylor, and Chetty 1985) injections of nanomaterials (Meng et al. 2011). Moreover, hemolysis has been reported to occur after i.m. diclofenac-therapy as well (Ahrens et al. 2004). Figure 5 provides a summary of the required safety assessments for each category of iNP.

3.3.1. Application of the hazard assessment concept

In the following sections, the case of super-paramagnetic iron oxide nanoparticles (SPIONs) is discussed to demonstrate the applicability and validity of the HES recommendations provided in Figure 5. These iNPs are used as imaging agents and therapeutics to treat glioblastoma, iron deficiency anemia, and iron deficiency in chronic kidney disease (Kievit and Zhang 2011; McCormack 2012; Ros et al. 1995; Weinstein et al. 2010). We were able to match one specific type of SPION to every ENP interaction group and to discuss the proposed HES test strategy in the light of observed *in vitro* and *in vivo* toxic effects. SPIONs were categorized based on FDA compliant preclinical test procedures. Temporal changes in the surface coating of the ENP are not considered. This approach can be justified since storage stability under physiological conditions was assessed based on criteria discussed above.

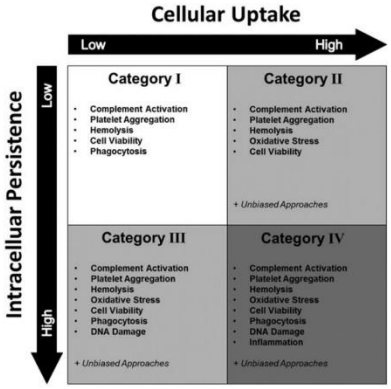

Figure 5. Recommended HES hazard assessments for iNP. Depending on the outcomes in tier 2, an iNP is proposed to pass a hazard assessment cascade individually tailored for one of the four risk categories. Increasing levels of uptake and persistence require more elaborate assay cascades. The eight assays include complement activation, platelet aggregation, hemolysis, oxidative stress, cell viability, phagocytosis, inflammation, and DNA damage.

Category I: Pegylated SPIONs proposed as theranostics do not seem to be acutely toxic to rats after injection. In animal experiments, viability did not decrease over the course of three weeks (Jarockyte et al. 2016). Moreover, neither significant endocytic uptake nor accumulation of the particles was detectable leading to an extended systemic circulation and a prolonged contact with blood cells. These particles are considered to be well tolerated. However, PEGylation may potentially cause complement activation (leading to the hypersensitivity syndrome 'C activation-related pseudo allergy – CARPA') and represents a possible risk (Verhoef and Anchordoquy 2013). Based on these considerations, a test strategy with a focus on complement activation, platelet aggregation, and hemolysis is recommended. Moreover, even though no notable viability decrease was observed, there is a regulatory need of assuring that ENP do not affect cell viability. It is, therefore, required to test cell viability as well.

Category II: Unlike their PEGylated counterparts, endocytic cellular uptake is commonly observed with uncoated SPIONs (Singh et al. 2010). These nanoparticles are rapidly degraded within the lysosomal compartment placing them in the risk category II. *In vitro*, their degradation has been shown to trigger cytotoxic events such as mitochondrial oxidative stress and a significant cell viability decrease. *In vivo*, phagocytosis and hypersensitivity have been reported to be the consequence of treatment of rats with this type of SPIONs (Mahmoudi et al. 2012; Park 2003; Szebeni et al. 2015).

Category III: Approved drug formulations, such as Rienso (Friedrich et al. 2015) or Feraheme (Lu et al. 2010) are SPIONs coated with a layer of polyglucose sorbitol carboxymethylether (PSC). They are used to treat iron deficiency in patients suffering from chronic kidney disease. The PSC layer contributes to low cellular uptake and high persistence, simultaneously minimizing cytotoxic effects (low platelet aggregation and phagocytosis). In patients with a

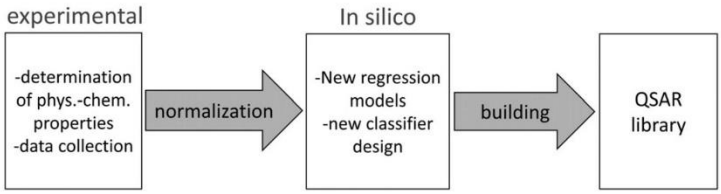

Figure 6. Workflow of a QSAR based grouping and modeling approach. Quantitative structure-activity relationships (QSAR) are used to correlate physicochemical properties of nanoparticles and cytotoxic effects. QSAR model libraries support grouping of ENP.

history of allergies, hypersensitivity was shown to be a likely side-effect (Lu et al. 2010). This is an example of a nanoparticle that would have successfully passed the proposed HES hazard assessment in category III.

Category IV: *In situ*-coated lauric acid ferrofluid ($SEON^{LA}$) (Friedrich et al. 2015; Zaloga et al. 2014) was used to validate the effect of different lauric acid coatings on SPIONs towards the application as a drug delivery system *in vitro* as well as *in vivo*. The formulation displayed high levels of cellular uptake (Zaloga et al. 2014) paired with a high biopersistence (Cicha 2016) *in vitro*. However, this formulation proved to be cytotoxic. Cell viability decreased and generation of reactive oxygen species combined with DNA damage were observed (Friedrich et al. 2015; Zaloga et al. 2014). Moreover, the tendency of $SEON^{LA}$ to agglomerate while in circulation is indicative of a liability for phagocytosis, complement activation, platelet aggregation and hemolysis. The proposed HES test strategy for category IV ENP would have been appropriate to uncover these risks.

4. HES compared to existing hazard evaluation strategies

The HES provides an application-oriented and effective hazard evaluation cascade based on a novel classification approach and well-accepted protocols. To our knowledge, the HES is the first hazard evaluation strategy that targets solely the pharmaceutical applicability of injectable ENP and does this in a unique manner.

To underline this statement, we compared our strategy to three alternative grouping and hazard evaluation strategies that were proposed either by regulatory authorities or by academia. The chosen strategies use different approaches and levels of complexity to determine nanomaterial safety.

4.1. QSAR-based grouping and modeling

The two-tiered strategy groups metal oxide nanoparticles based on their physicochemical characteristics and subsequently uses a quantitative structure-activity relationships (QSARs) analysis to identify statistical correlations with cytotoxic effects (Sayes et al. 2013). Such a QSAR approach was used previously as well to group non-nano substances based on structural similarities (ECHA 2013). Defined physicochemical properties of nanoparticles are measured using a screening approach, normalized, and statistically analyzed. This approach relies on *in silico* pattern recognition techniques and predictive modeling. The workflow is schematically depicted in Figure 6.

This test strategy was validated based on the analysis of silver, copper, nickel, iron, and zinc nanoparticles. Nanoparticles were suspended in aqueous media according to a defined protocol. The measured properties included engineered particle size, agglomerate size in water, ζ-potential, pH, and age of suspension. The measured biological response was the production of ROS. In order to compare results, the raw data was normalized *'[…] by dividing each raw data value by the standard deviation in its respective data type […]'* (Sayes et al. 2013). Statistical methods (i.e. principal component analysis – PCA and correlation analysis – CA) were used to group the metal oxide nanoparticles (Tämm et al. 2016). In contrast to the HES, this QSAR approach was specifically designed to support the analysis of metal nanoparticles. Considering that a solid validation of the HES will provide a large

Table 3. Nanoparticle risk assessment based on dose exposure. Starting from a deposited dose, the dose rate or dose equivalents of nanoparticles deposited in specific target tissues or organs are estimated.

Deposited dose (D)	Dose rate (DR)	Committed tissue dose (TD)	Equivalent dose (ED)	Effective dose ($DEff$)
Deposited surface area (SA) per mass of living matter (M)	Mean absorbed dose (D_{mean}) in target tissue ($tiss$) at time point (t)	Quantity of D taken up over a defined time period (τ)	TD weighted by nanoparticle - specific weighting factors (w_N)	Tissue - weighted (W_T) sum of ED in all tissues/organs
$D = SA/M$	$DR = D_{mean,tiss}\ (t)$	$TD = \int_0^{\tau} DR\ dt$	$ED = w_N \cdot TD$	$DEff = \Sigma w_T \cdot ED$

The toxic impact of nanoparticles on specific organs can thus be approximated. The nanoparticle dose units are square meters per kilogram (m^2/kg). The term deposited surface area (SA) corresponds to the total surface area of nanoparticles the sample (M) is potentially exposed to.
Table adapted from Simkó et al. (2014).

amount of processable data, data mining and QSAR analysis could aid to establish a future grouping strategy for iNP. For metal oxide nanoparticles this has already been shown by Zhang et al. (2012) where the ENP band gap was used to develop predictive paradigm for oxidative stress and inflammation (Zhang et al. 2012).

4.2. Dosimetry-based risk assessment

In this approach, nanoparticles can be grouped as safe or unsafe in relation to the applied nanoparticle dose, which in this case is uniformly defined in square meters per kilogram (m^2/kg) (Simkó, Nosske, and Kreyling 2014). Weighting factors are introduced to account for differences in physicochemical properties of ENP. The concept provides an elegant solution on how to calculate the dose rate (DR), committed tissue dose (TD), equivalent dose (ED), and effective dose (DEff) of a nanoparticle formulation based on the knowledge of the original deposited nanoparticle dose (D) (Table 3).

The reactivity and thus toxic potential of different nanoparticles at a given dose can be determined by calculating the ED considering several nanoparticle-specific properties (i.e. nanoparticle weighting factors, W_N). The W_N chosen by the authors were specific surface area, surface texture, ζ-potential, particle morphology, band gap energy levels for metal as well as metal oxide nanoparticles, and particle dissolution/dissociation rates. This concept supports our notion that a careful dose assessment is indispensable to compare and interpret experiments and studies. Although the HES does provide its own proposal on dosimetry as well, the two concepts differ significantly. In principle, the dosimetry concept is designed to enable risk assessments for any nanomaterial in any tissue or organ and groups nanomaterials thereafter. However, at present, the concept has limitations due to the lack of tissue- and organ-specific data and was applied to the analysis of metal particles only.The HES assumes that toxicity does not occur at a defined exposure but is based on dose-response relationships. The HES does not define exposure limits for toxicity but rather uncovers potential hazards.

4.3. The 'DF4Nano' concept

In 2015, the European Centre for Ecotoxicology and Toxicology of Chemicals 'Nano Task Force' (ECETOC) has published a new decision-making framework on nanomaterial grouping (Arts et al. 2015). The DF4NanoGrouping approach is a multi-tiered grouping strategy that *'[…] uses the 'functionality' of nanomaterials for grouping rather than relying on intrinsic material properties alone […].'* With the strict exception of medical or therapeutic ENP, nanomaterials can be grouped with the DF4Nano approach according to the adverse outcome pathway (AOP) concept (Ankley et al. 2010). An AOP is designed to establish a link between a sequence of measurable key events and an adverse outcome. The DF4Nano is the first AOP concept specific to nanomaterials. The strategy is divided into four main parts as shown in Figure 7. Starting with defining and measuring intrinsic material properties, the concept takes system-dependent nanomaterial properties into account before determining their impact on cells and entire systems (organs, organisms). The experimental section is divided into three tiers of *in vitro* assay cascades. In tier 1, basic physicochemical properties for ENM are determined. This includes the determination of particle size, surface area, shape, aspect ratio, chemical composition, aqueous solubility, and impurities. Thereafter, system-dependent properties such as exposure, uptake, biodistribution, biopersistence, and cellular effects are monitored in tier 2. *In vivo* studies are

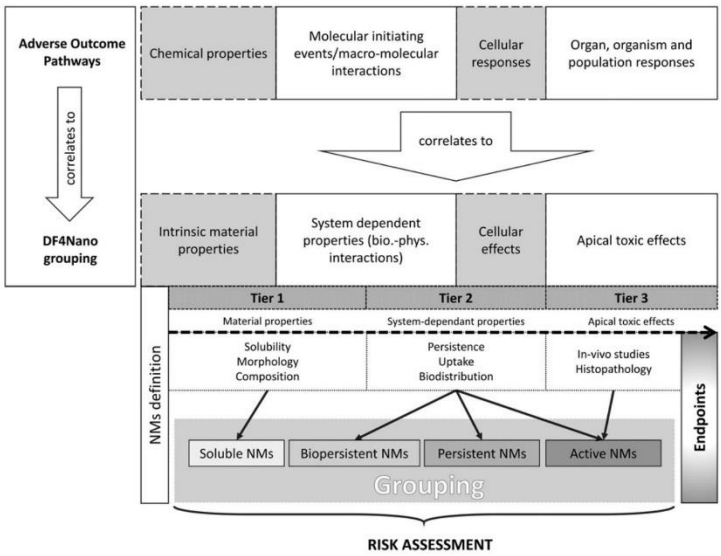

Figure 7. Overview of the DF4NanoGrouping approach of ECETOC. The DF4NanoGrouping strategy designed for nanomaterials adopts the Adverse Outcome Pathway (AOP) approach designed for chemicals. Generally, the grouping is divided into four steps where intrinsic material properties, system dependent properties, cellular effects, and apical toxic effects are determined. The experimental part of the concept is a three-tiered assay cascade. Nanomaterials are grouped into soluble, biopersistent, passive or active nanomaterials. The DF4NanoGrouping strategy is not applicable for nanomedicines or nano-therapeutics. It is explicitly designed for the risk assessment of environmental and accidental nanomaterial exposure. Adapted from Arts et al. (2015).

carried out in tier 3. Based on this concept, four main nanomaterial groups are defined (i.e. soluble, biopersistent, passive and active nanomaterials). Biopersistence refers to insoluble high-aspect-ratio (HARN) nanomaterials. Passive nanomaterials include non-fibrous, biopersistent materials that have the tendency to agglomerate in biological fluids. In contrast to active materials, they lack chemical reactivity. The thresholds and limitations defining the decision-making process of grouping in the DF4Nano concept are based on regulatory standards and authority proposals.

The DF4NanoGrouping concept is a rather complex grouping approach that is – to a certain extent – similar to the HES approach. However, the two concepts group nanomaterials based on different parameters. The DF4Nano concept is based on solubility and reactivity, whereas the HES categorizes nanoparticles according to cellular uptake and intracellular persistence. The DF4Nano concept cannot be used for the grouping and risk assessment of medical and therapeutic nanomaterials. The HES, on the other hand, does feature a possibility of establishing both for injectable nanomedicines. In contrast to the DF4Nano concept, however, the HES is not based on a systematic screening approach but combines a subset of individual experiments and specific exclusion criteria to generate standardized data needed for risk assessment.

5. Discussion

The proposed Hazard Evaluation System for Injectable Nanoparticles (HES) is a three-tiered hazard evaluation concept that was specifically designed for injectable nanoparticles (iNP) used as nanomedicines. To demonstrate that the approach poses a valid alternative or extension to existing grouping and risk assessment strategies, we compared the HES to three alternative screening and risk assessment strategies.

In Table 4, an overview of all 28 measured experimental parameters of the four discussed concepts is provided. ζ-potential, shape, size, and aspect ratio were the key properties for most

Table 4. Overview of relevant hazard evaluation determinants.

Parameters	QSAR-based concept	Dosimetry concept	DF4Nano concept	HES
Physicochemical properties (tier I)				
Chemical identity				X
Shape		X	X	X
Size	X	X	X	X
Aspect ratio		X	X	X
PDI		X	X	X
ζ-potential	X	X	X	X
Agglomeration size	X			
Surface area		X	X	
Surface texture		X		
pH	X			X
Solubility/Stability		X	X	X
Suspension age	X			
Contamination/Impurity			X	X
System-dependent properties (tier II)				
Exposure		X		
Biopersistence			X	
Intracellular persistence				X
Systemic uptake		X	X	
Cell specific uptake				X
Cellular effects			X	X
Concentration/Dosimetry	X	X		X
Bioactivity		X		
Biodistribution			X	
Toxic endpoints (tier III)				
Complement activation				X
Platelet aggregation				X
Hemolysis				X
Oxidative stress	X	X	X	X
Cytotoxicity	X	X	X	X
Cell viability			X	X
Phagocytosis		X	X	X
DNA damage				X
Inflammation			X	X

Comparison between the HES and three alternative hazard evaluation approaches.
The four discussed strategies use different combinations of experimental parameters, which cover physicochemical properties (tier I), system-dependent properties (tier II), and toxic endpoints (tier III).

concepts. Any experimental result should be critically evaluated considering the aspects of contamination, impurity, and dosimetry. This comparison shows that the HES uses the highest number of measured parameters. However, the HES (in contrast to the other strategies) is not a screening approach but uses an informed decision-making process to minimize the number of needed experiments. The HES follows thereby an intuitive and straightforward decision-making path.

In terms of future applications of the concept, several scenarios can be envisaged. First, preclinical safety evaluations will be facilitated since the HES is based on physicochemical exclusion criteria. Non-qualifying materials can be identified and the number of *in vitro* experiments can be minimized. Second, the number of *in vitro* experiments can be further reduced based on selective application of toxicological assays. This approach is cost-effective. Third, a careful *in vitro* evaluation of test materials at early stages of the development process helps to avoid costly *in vivo* experiments at later stages. This is in line with the 3R principles of animal welfare. Fourth, the HES concept will help to mitigate the risk of off-target effects *in vivo*. Fifth, it is tempting to speculate that a systematic evaluation of nanomaterials will form the basis for future grouping strategies. It will, thus, be possible to correlate physicochemical properties with hazard categories of injectable nanopharmaceuticals. This knowledge can guide the design of novel and/or optimized nanomaterials according to safe-by-design principles (as presented by the NanoReg and Prosafe European initiatives) to assist both regulatories and industry. It addresses issues regarding nanomaterial safety, both in products and processes (Gottardo 2017). The HES works towards this principle by focusing on injectable nanoparticles. By proposing a stepwise strategy based on key parameters, the HES encourages developers to consider safety during the different steps of product design.

6. Conclusions

The motivation of this project was to develop an application-oriented, cost-effective, robust, and user-friendly hazard assessment concept for nanopharmaceuticals. To the knowledge of the authors, HES is the first hazard evaluation concept focusing entirely on the application of nanoparticles as injectable formulations. Validation of the HES approach using well characterized reference materials will be an important next step towards its acceptance and implementation by research scientists as well as regulatory authorities.

Acknowledgments

We express our gratitude to Prof. Dr. Martin Wilks (Swiss Centre for Applied Human Toxicology – SCAHT), Dr. Andrea Haase ("Bundesinstitut für Risikobewertung – BfR" and the NanoReg2 consortium), Dr. Christoph Studer ("Bundesamt für Gesundheit – BAG"), and Dr. Blanca Suarez (TEMAS AG) for their valuable inputs on the novel hazard evaluation strategy.

Disclosure statement

Dr. P. Wick is executive board member of the EUNCL.

Funding

This work was financially supported by the Swiss Centre for Applied Human Toxicology (SCAHT), the NanoReg2 program (European Union Horizon 2020 research agreement 646221, 15.0200-3), and the NanoScreen Materials Challenge co-founded by the Competence Centre for Materials Science and Technology (CCMX).

References

Aderem, A. 2003. "Phagocytosis and the Inflammatory Response." *The Journal of Infectious Diseases* 187 (s2): S340–S345. doi:10.1086/374747

Aguilar-Castillo, B. A., J. L. Santos, H. Luo, Y. E. Aguirre-Chagala, T. Palacios-Hernandez, and M. Herrera-Alonso. 2015. "Nanoparticle Stability in Biologically Relevant Media: influence of Polymer Architecture." *Soft Matter* 11 (37): 7296–7307. doi:10.1039/C5SM01455G

Ahrens, N., L. Schewior, E. Garbe, H. Kiesewetter, and A. Salama. 2004. "Massive Haemolysis after Intramuscular Diclofenac in a Patient Who Apparently Tolerated Oral Medication." *Vox Sanguinis* 86 (1): 71–74. doi:10.1111/j.0042-9007.2004.00389.x

Akthakul, A., A. I. Hochbaum, F. Stellacci, and A. M. Mayes. 2005. "Size Fractionation of Metal Nanoparticles by Membrane Filtration." *Advanced Materials* 17 (5): 532–535. doi:10.1002/adma.200400636

Álvarez-Fuentes, J., L. Martín-Banderas, I. Muñoz-Rubio, M. A. Holgado, and M. Fernández-Arévalo. 2012. "Development and Validation of an RP-HPLC Method for CB13 Evaluation in Several PLGA Nanoparticle Systems [WWW Document]." *The Scientific World Journal* 2012: 737526. doi:10.1100/2012/737526

Ambrogio, M. W., C. R. Thomas, Y.-L. Zhao, J. I. Zink, and J. F. Stoddart. 2011. "Mechanized Silica Nanoparticles: A New Frontier in Theranostic Nanomedicine." *Accounts of Chemical Research* 44 (10): 903–913. doi:10.1021/ar200018x

Amenabar, I., S. Poly, W. Nuansing, E. H. Hubrich, A. A. Govyadinov, F. Huth, R. Krutokhvostov, L. Zhang, M. Knez, J. Heberle. J., et al. 2013. "Structural Analysis and Mapping of Individual Protein Complexes by Infrared Nanospectroscopy." *Nature Communications* 4 (1): 3890. Ncomms doi:10.1038/ncomms3890

Amidon, G. L., H. Lennernäs, V. P. Shah, and J. R. Crison. 1995. "A Theoretical Basis for a Biopharmaceutic Drug Classification: The Correlation of in Vitro Drug Product Dissolution and in Vivo Bioavailability." *Pharmaceutical Research* 12: 413–420. doi:10.1023/A:1016212804288

Ankley, G. T., R. S. Bennett, R. J. Erickson, D. J. Hoff, M. W. Hornung, R. D. Johnson, D. R. Mount, J. W. Nichols, C. L. Russom, P. K. Schmieder, et al. 2010. "Adverse Outcome Pathways: A Conceptual Framework to Support Ecotoxicology Research and Risk Assessment." *Environmental Toxicology and Chemistry* 29 (3): 730–741. doi:10.1002/etc.34

Arap, W., R. Pasqualini, M. Montalti, L. Petrizza, L. Prodi, E. Rampazzo, N. Zaccheroni, and S. Marchiò. 2013. "Luminescent Silica Nanoparticles for Cancer Diagnosis." *Current Medicinal Chemistry* 20 (17): 2195–2211. doi:10.2174/0929867311320170005

Arts, J. H. E., M. Hadi, M.-A. Irfan, A. M. Keene, R. Kreiling, D. Lyon, M. Maier, K. Michel, T. Petry, U. G. Sauer, et al. 2015a. "A Decision-Making Framework for the Grouping and Testing of Nanomaterials (DF4nanoGrouping)." *Regulatory Toxicology and Pharmacology* 71 (2): S1–S27. doi:10.1016/j.yrtph.2015.03.007

Atkinson, P. M., D. I. Taylor, and N. Chetty. 1985. "Inhibition of Platelet Aggregation by Ketamine Hydrochloride." *Thrombosis Research* 40 (2): 227–234. doi:10.1016/0049-3848(85)90333-0

Bao, H., X. Yu, C. Xu, X. Li, Z. Li, D. Wei, and Y. Liu. 2015. "New Toxicity Mechanism of Silver Nanoparticles: Promoting Apoptosis and Inhibiting Proliferation." *PLoS One* 10 (3): e0122535. doi:10.1371/journal.pone.0122535

Bartneck, M., H. A. Keul, S. Singh, K. Czaja, J. Bornemann, M. Bockstaller, M. Moeller, G. Zwadlo-Klarwasser, and J. Groll. 2010a. "Rapid Uptake of Gold Nanorods by Primary Human Blood Phagocytes and Immunomodulatory Effects of Surface Chemistry." *ACS Nano* 4 (6): 3073–3086. doi:10.1021/nn100262h

Bartneck, M., H. A. Keul, G. Zwadlo-Klarwasser, and J. Groll. 2010b. "Phagocytosis Independent Extracellular Nanoparticle Clearance by Human Immune Cells." *Nano Letters* 10 (1): 59–63. doi:10.1021/nl902830x

Berg, J. M., A. Romoser, N. Banerjee, R. Zebda, and C. M. Sayes. 2009. "The Relationship between pH and Zeta Potential of ~30 Nm Metal Oxide Nanoparticle Suspensions Relevant to in Vitro Toxicological Evaluations." *Nanotoxicology* 3 (4): 276–283. doi:10.3109/17435390903276941

Berger, M. 2009. "Size matters. Comparing the toxicity of micro- to nanoparticles" [WWW Document]. Accessed August 21 2017. http://www.nanowerk.com/spotlight/spotid=10128.php

Bhattacharjee, S. 2016. "DLS and Zeta Potential – What They Are and What They Are Not?." *Journal of Controlled Release* 235: 337–351. doi:10.1016/j.jconrel.2016.06.017

Bleeker, E. A. J., W. H. de Jong, R. E. Geertsma, M. Groenewold, E. H. W. Heugens, M. Koers-Jacquemijns, D. van de Meent, J. R. Popma, A. G. Rietveld, S. W. P. Wijnhoven, et al. 2013. "Considerations on the EU Definition of a Nanomaterial: Science to Support Policy Making." *Regulatory Toxicology and Pharmacology* 65 (1): 119–125. doi:10.1016/j.yrtph.2012.11.007

Bobo, D., K. J. Robinson, J. Islam, K. J. Thurecht, and S. R. Corrie. 2016. "Nanoparticle-Based Medicines: A Review of FDA-Approved Materials and Clinical Trials to Date." *Pharmaceutical Research* 33 (10): 2373–2387. doi:10.1007/s11095-016-1958-5

Boilard, S. P., P. R. Amyotte, F. I. Khan, A. G. Dastidar, and R. K. Eckhoff. 2013. "Explosibility of Micron- and Nano-Size Titanium Powders." *Journal of Loss Prevention in the Process Industries* 26 (6): 1646–1654. doi:10.1016/j.jlp.2013.06.003

Bolt, H. M. 2014. "Grouping of Nanomaterials for Risk Assessment." *Archives of Toxicology* 88 (12): 2077–2078. doi:10.1007/s00204-014-1416-2

Bozzuto, G., and A. Molinari. 2015. "Liposomes as Nanomedical Devices." *International Journal of Nanomedicine* 10: 975–999. doi10.2147/IJN.S68861

Brown, J. S., T. Gordon, O. Price, and B. Asgharian. 2013. "Thoracic and Respirable Particle Definitions for Human Health Risk Assessment." *Particle and Fibre Toxicology* 10 (1): 12. doi:10.1186/1743-8977-10-12

Buzea, C., I. I. Pacheco, and K. Robbie. 2007. "Nanomaterials and Nanoparticles: sources and Toxicity." *Biointerphases* 2 (4): MR17–MR71. doi:10.1116/1.2815690

Casals, E., T. Pfaller, A. Duschl, G. J. Oostingh, and V. Puntes. 2010. "Time Evolution of the Nanoparticle Protein Corona." *ACS Nano* 4 (7): 3623–3632. doi:10.1021/nn901372t

Champion, J. A., Y. K. Katare, and S. Mitragotri. 2007. "Particle Shape: A New Design Parameter for Micro- and Nanoscale Drug Delivery Carriers." *Official journal of the Controlled Release Society* 121 (1–2): 3–9. doi:10.1016/j.jconrel.2007.03.022

Chen, F., G. Wang, J. I. Griffin, B. Brenneman, N. K. Banda, V. M. Holers, D. S. Backos, L. Wu, S. M. Moghimi, and D. Simberg. 2017. "Complement Proteins Bind to Nanoparticle Protein Corona and Undergo Dynamic Exchange In Vivo." *Nature Nanotechnology* 12 (4): 387–393. doi:10.1038/nnano.2016.269

Chukwuocha, E. O., M. C. Onyeaju, and T. S. T. Harry. 2012. "Theoretical Studies on the Effect of Confinement on Quantum Dots Using the Brus Equation World Journal of Condensed Matter Physics 2 (2): 96–100. doi:10.4236/wjcmp.2012.22017

Cicha, I. 2016. "Strategies to Enhance Nanoparticle-Endothelial Interactions under Flow." *Journal of Cellular Biotechnology* 1 (2): 191–208. doi:10.3233/JCB-15020

Clogston, J. D., and A. K. Patri. 2011. "Zeta Potential Measurement." *Methods in Molecular Biology (Clifton, N.J.)* 697: 63–70. doi:10.1007/978-1-60327-198-1

Coti, K. K., M. E. Belowich, M. Liong, M. W. Ambrogio, Y. A. Lau, H. A. Khatib, J. I. Zink, N. M. Khashab, and J. F. Stoddart. 2009. "Mechanised Nanoparticles for Drug Delivery." *Nanoscale* 1 (1): 16–39. doi:10.1039/b9nr00162j

Crawford, R., B. Dogdas, E. Keough, R. M. Haas, W. Wepukhulu, S. Krotzer, P. A. Burke, L. Sepp-Lorenzino, A. Bagchi, and B. J. Howell. 2011. "Analysis of Lipid Nanoparticles by Cryo-EM for Characterizing siRNA Delivery Vehicles." *International Journal of Pharmaceutics* 403 (1–2): 237–44. doi:10.1016/j.ijpharm.2010.10.025

Davignon, J., and P. Ganz. 2004. "Role of Endothelial Dysfunction in Atherosclerosis." *Circulation* 109 (23_suppl_1): III-27–III-32. doi:10.1161/01.CIR.0000131515.03336.f8

Deanfield, J., A. Donald, C. Ferri, C. Giannattasio, J. Halcox, S. Halligan, A. Lerman, G. Mancia, J. J. Oliver, A. C. Pessina, et al., Working Group on Endothelin and Endothelial Factors of the European Society of Hypertension. 2005. "Endothelial Function and Dysfunction. Part I: Methodological Issues for Assessment in the Different Vascular Beds: A Statement by the Working Group on Endothelin and Endothelial Factors of the European Society of Hypertension." *Journal of Hypertension* 23 (1): 7–17. doi:10.1097/00004872-200501000-00004

Dekkers, S., A. G. Oomen, E. A. J. Bleeker, R. J. Vandebriel, C. Micheletti, J. Cabellos, G. Janer, N. Fuentes, S. Vázquez-Campos, T. Borges, et al. 2016. "Towards a Nanospecific Approach for Risk Assessment." *Regulatory Toxicology and Pharmacology* 80: 46–59. doi:10.1016/j.yrtph.2016.05.037

Dobrovolskaia, M. A., A. K. Patri, J. Simak, J. B. Hall, J. Semberova, S. H. De Paoli Lacerda, and S. E. McNeil. 2012. "Nanoparticle Size and Surface Charge Determine Effects of PAMAM Dendrimers on Human Platelets in Vitro." *Molecular Pharmaceutics* 9 (3): 382–393. doi:10.1021/mp200463e

Docter, D., D. Westmeier, M. Markiewicz, S. Stolte, S. K. Knauer, and R. H. Stauber. 2015. "The Nanoparticle Biomolecule Corona: lessons Learned – Challenge Accepted?" *Chemical Society Reviews* 44: 6094–6121. doi:10.1039/C5CS00217F

Dongargaonkar, A. A., and J. D. Clogston. 2018. "Quantitation of Surface Coating on Nanoparticles Using Thermogravimetric Analysis." In *Characterization of Nanoparticles Intended for Drug Delivery, Methods in Molecular Biology*, edited by McNeil S, 57–63. New York, NY: Humana Press. doi:10.1007/978-1-4939-7352-1_6

Droppo, I. G. 2006. "*Filtration in Particle Size Analysis.*" *In Encyclopedia of Analytical Chemistry*, edited by R. A. Meyers and R. B. Flippen. Hoboken, New Jersey: John Wiley & Sons, Ltd. doi:10.1002/9780470027318.a1506

Dusinska, M., M. Dusinska, L. Fjellsbø, Z. Magdolenova, A. Rinna, E. Runden Pran, A. Bartonova, E. Heimstad, M. Harju, L. Tran. et al. 2009. "Testing Strategies for the Safety of Nanoparticles Used in Medical Applications." *Nanomed* 4 (6): 605–607. doi:10.2217/nnm.09.47

ECHA. 2013. "Grouping of Substances and Read-Across – ECHA" [WWW Document]. Accessed August 28 2017. https://echa.europa.eu/support/registration/how-to-avoid-unnecessary-testing-on-animals/grouping-of-substances-and-read-across

Elgqvist, J. 2017. "Nanoparticles as Theranostic Vehicles in Experimental and Clinical Applications—Focus on Prostate and Breast Cancer." *International Journal of Molecular Sciences* 18 (5): 1102. doi:10.3390/ijms18051102

Ermidou-Pollet, S., H. Nounopoulos, N. Sdougas, M. Szilágyi, and S. Pollet. 2005. "Influence of Subcutaneous Injection of Essential Fatty Acids on the Stress-Induced Modifications of Rat Platelet Aggregation and Membrane Lipid Composition." *Acta Biologica Hungarica* 56 (3–4): 247–259. doi:10.1556/ABiol.56.2005.3-4.8

Etheridge, M. L., S. A. Campbell, A. G. Erdman, C. L. Haynes, S. M. Wolf, and J. McCullough. 2013. "The Big Picture on Small Medicine: The State of Nanomedicine Products Approved for Use or in Clinical Trials." *Nanomedicine: Nanotechnology, Biology, and Medicine* 9 (1): 1–14. doi:10.1016/j.nano.2012.05.013

European Medicines Agency - Multidisciplinary - Data requirements for intravenous iron-based nano-colloidal products developed with reference to an innovator medicinal product [WWW Document], n.d. Accessed January 19 2018. http://www.ema.europa.eu/docs/en_GB/document_library/Scientific_guideline/2015/03/WC500184922.pdf

European Medicines Agency - Multidisciplinary - Joint MHLW/EMA reflection paper on the development of block copolymer micelle medicinal products [WWW Document], n.d. Accessed January 19 2018. http://www.ema.europa.eu/docs/en_GB/document_library/Scientific_guideline/2013/02/WC500138390.pdf

European Medicines Agency - Multidisciplinary - Reflection paper on surface coatings: general issues for consideration regarding parenteral administration of coated nanomedicine products [WWW Document], n.d. Accessed January 19 2018. http://www.ema.europa.eu/docs/en_GB/document_library/Scientific_guideline/2013/08/WC500147874.pdf

European Medicines Agency - Multidisciplinary - Reflection paper on the data requirements for intravenous liposomal products developed with reference to an innovator liposomal product [WWW Document], n.d. Accessed January 19 2018. http://www.ema.europa.eu/docs/en_GB/document_library/Scientific_guideline/2013/03/WC500140351.pdf

European Medicines Agency - Multidisciplinary - Reflection paper on nanotechnology-based medicinal products for human use [WWW Document], n.d. Accessed 19 Jan 2018. http://www.ema.europa.eu/docs/en_GB/document_library/Regulatory_and_procedural_guideline/2010/01/WC500069728.pdf

Fabricius, A.-L., L. Duester, B. Meermann, and T. A. Ternes. 2014. "ICP-MS-Based Characterization of Inorganic Nanoparticles—Sample Preparation and off-Line Fractionation Strategies." *Analytical and Bioanalytical Chemistry* 406 (2): 467–479. doi:10.1007/s00216-013-7480-2

Fadeel, B. 2012. *Clear and Present Danger? Engineered Nanoparticles and the Immune System [WWW document]*. Swiss Med. Wkly. Accessed May 11 2016. http://blog.smw.ch/

Fadeel, B., A. Pietroiusti, and A. A. Shvedova. 2017. *Adverse Effects of Engineered Nanomaterials: Exposure, Toxicology, and Impact on Human Health*. Cambridge, Massachusetts: Academic Press.

FDA. 2005. "Guidance for Industry on Estimating the Maximum Safe Starting Dose in Initial Clinical Trials for Therapeutics in Adult Healthy Volunteers." Availability [WWW Document]. Fed. Regist. Accessed August 24 2017. https://www.federalregister.gov/documents/2005/07/22/05-14456/guidance-for-industry-on-estimating-the-maximum-safe-starting-dose-in-initial-clinical-trials-for

Félétou, M. 2011. "The Endothelium: Part 1: Multiple Functions of the Endothelial Cells—Focus on Endothelium-Derived Vasoactive Mediators." In *Integrated Systems Physiology: From Molecule to Function to Disease*, edited by D. Neil Granger and Joey P. Granger, 1–306. San Rafael (CA): Morgan & Claypool Life Sciences.

Feliu, N., and B. Fadeel. 2010. "Nanotoxicology: No Small Matter." *Nanoscale* 2 (12): 2514–2520. doi:10.1039/c0nr00535e

Friedrich, R. P., C. Janko, M. Poettler, P. Tripal, J. Zaloga, I. Cicha, S. Dürr, J. Nowak, S. Odenbach, I. Slabu. et al. 2015. "Flow Cytometry for Intracellular SPION Quantification: Specificity and Sensitivity in Comparison with Spectroscopic Methods." *International Journal of Nanomedicine* 10: 4185–4201. doi:10.2147/IJN.S82714

Fröhlich, E. 2017. "Role of Omics Techniques in the Toxicity Testing of Nanoparticles." *Journal of Nanobiotechnology* 15 (1): 84. doi:10.1186/s12951-017-0320-3

Fubini, B., M. Ghiazza, and I. Fenoglio. 2010. "Physico-Chemical Features of Engineered Nanoparticles Relevant to Their Toxicity." *Nanotoxicology* 4 (4): 347–363. doi:10.3109/17435390.2010.509519

Gallud, A., and B. Fadeel. 2015. "Keeping It Small: Towards a Molecular Definition of Nanotoxicology." *European Journal of Nanomedicine* 7: 143–151. doi:10.1515/ejnm-2015-0020

Garbovskiy, Y. 2017. "Biological Contamination of Nanoparticles and Its Manifestation in Optical Absorbance Measurements." *Analytical Chemistry* 89 (14): 7282–7285. doi:10.1021/acs.analchem.7b01766

Gebel, T., H. Foth, G. Damm, A. Freyberger, P.-J. Kramer, W. Lilienblum, C. Röhl, T. Schupp, C. Weiss, K.-M. Wollin, et al. 2014. "Manufactured Nanomaterials: Categorization and Approaches to Hazard Assessment." *Archives of Toxicology* 88 (12): 2191–2211. doi:10.1007/s00204-014-1383-7

Goldstein, A., Y. Soroka, M. Frušić-Zlotkin, I. Popov, and R. Kohen. 2014. "High Resolution SEM Imaging of Gold Nanoparticles in Cells and Tissues." *Journal of Microscopy* 256 (3): 237–247. doi:10.1111/jmi.12179

Gottardo, S. 2017. "NANoREG Framework for the Safety Assessment of Nanomaterials - EU Science Hub - European Commission [WWW Document]." *EU Science Hub*. Accessed March 7 2018. https://ec.europa.eu/jrc/en/publication/eur-scientific-and-technical-research-reports/nanoreg-framework-safety-assessment-nanomaterials

Gregoriadis, G., 1985. Liposomes for drugs and vaccines. *Trends Biotechnol*. 3: 235–241. doi:10.1016/0167-7799(85)90014-9

Gregory, A. E., R. Titball, and D. Williamson. 2013. "Vaccine Delivery Using Nanoparticles." *Frontiers in Cellular and Infection Microbiology* 3: 13. doi:10.3389/fcimb.2013.00013

Guadagnini, R., B. Halamoda Kenzaoui, L. Walker, G. Pojana, Z. Magdolenova, D. Bilanicova, M. Saunders, L. Juillerat-Jeanneret, A. Marcomini, A. Huk, et al. 2015. "Toxicity Screenings of Nanomaterials: Challenges Due to Interference with Assay Processes and Components of Classic in Vitro Tests." *Nanotoxicology* 9 (Supp1): 13–24. doi:10.3109/17435390.2013.829590

Guarnieri, D., S. Sabella, O. Muscetti, V. Belli, M. A. Malvindi, S. Fusco, E. De Luca, P. P. Pompa, and P. A. Netti. 2014. "Transport across the Cell-Membrane Dictates Nanoparticle Fate and Toxicity: A New Paradigm in Nanotoxicology." *Nanoscale* 6 (17): 10264–10273. doi:10.1039/C4NR02008A

Guha, S., M. Li, M. J. Tarlov, and M. R. Zachariah. 2012. "Electrospray–Differential Mobility Analysis of Bionanoparticles." *Trends Biotechnol* 30 (5): 291–300. doi:10.1016/j.tibtech.2012.02.003

Guo, C., Y. Xia, P. Niu, L. Jiang, J. Duan, Y. Yu, X. Zhou, Y. Li, and Z. Sun. 2015. "Silica Nanoparticles Induce Oxidative Stress, Inflammation, and Endothelial Dysfunction in Vitro via Activation of the MAPK/Nrf2 Pathway and Nuclear Factor-κB Signaling." *International Journal of Nanomedicine* 10: 1463–1477. doi:10.2147/IJN.S76114

Guo, C., and J. L. Yarger. 2018. "Characterizing Gold Nanoparticles by NMR Spectroscopy." *Magnetic Resonance in Chemistry*. doi:10.1002/mrc.4753. [Epub ahead of print]

Hackley, V. A., and J. D. Clogston. 2011. "Measuring the Hydrodynamic Size of Nanoparticles in Aqueous Media Using Batch-Mode Dynamic Light Scattering." In *Characterization of Nanoparticles Intended for Drug Delivery*, edited by S. E. McNeil, 35–52. Totowa, NJ: Humana Press. doi:10.1007/978-1-60327-198-1_4

Hadrup, N., A. K. Sharma, M. Poulsen, and E. Nielsen. 2015. "Toxicological Risk Assessment of Elemental Gold following Oral Exposure to Sheets and Nanoparticles - A Review." *Regulatory Toxicology and Pharmacology* 72 (2): 216–221. doi:10.1016/j.yrtph.2015.04.017

Hole, P., K. Sillence, C. Hannell, C. M. Maguire, M. Roesslein, G. Suarez, S. Capracotta, Z. Magdolenova, L. Horev-Azaria, A. Dybowska, et al. 2013. "Interlaboratory Comparison of Size Measurements on Nanoparticles Using Nanoparticle Tracking Analysis (NTA)." *Journal of Nanoparticle Research* 15 (12): 2101. doi:10.1007/s11051-013-2101-8

Hung, H.-l., O. J. Klein, S. W. Peterson, S. R. Rokosh, S. Osseiran, N. H. Nowell, and C. L. Evans. 2016. "PLGA Nanoparticle Encapsulation Reduces Toxicity While Retaining the Therapeutic Efficacy of EtNBS-PDT In Vitro." *Scientific Reports* 6 (1): 33234. doi:10.1038/srep33234

Huth, F., A. Govyadinov, S. Amarie, W. Nuansing, F. Keilmann, and R. Hillenbrand. 2012. "Nano-FTIR Absorption Spectroscopy of Molecular Fingerprints at 20 Nm Spatial Resolution." *Nano Letters* 12 (8): 3973–3978. doi:10.1021/nl301159v

ISO. 2015. "ISO/TS 80004-2:2015(en), Nanotechnologies — Vocabulary — Part 2: Nano-objects." [WWW Document]. Accessed August 28 2017. https://www.iso.org/obp/ui/#iso:std:iso:ts:80004:-2:ed-1:v1:en

Itoh, N., E. Yamamoto, T. Santa, T. Funatsu, and M. Kato. 2016. "Effect of Nanoparticle Surface on the HPLC Elution Profile of Liposomal Nanoparticles." *Pharmaceutical Research* 33 (6): 1440–1446. doi:10.1007/s11095-016-1886-4

Jarockyte, G., E. Daugelaite, M. Stasys, U. Statkute, V. Poderys, T.-C. Tseng, S.-H. Hsu, V. Karabanovas, and R. Rotomskis. 2016. "Accumulation and Toxicity of Superparamagnetic Iron Oxide Nanoparticles in Cells and Experimental Animals." *International Journal of Molecular Sciences* 17 (8): 1193. doi:10.3390/ijms17081193

Jong, W. 2010. "Scientific Basis for the Definition of the Term 'nanomaterial'." [WWW Document] Accessed 28 August 2017. http://ec.europa.eu/health/scientific_committees/emerging/docs/scenihr_o_032.pdf

Joris, F., D. Valdepérez, B. Pelaz, S. J. Soenen, B. B. Manshian, W. J. Parak, S. C. De Smedt, and K. Raemdonck. 2016. "The Impact of Species and Cell Type on the Nanosafety Profile of Iron Oxide Nanoparticles in Neural Cells." *Journal of Nanobiotechnology* 14 (1): 69. doi:10.1186/s12951-016-0220-y

Junghanns, J.-U. A. H., and R. H. Müller. 2008. "Nanocrystal Technology, Drug Delivery and Clinical Applications." *International Journal of Nanomedicine* 3 (3): 295–310.

Kaszuba, M., D. McKnight, M. T. Connah, F. K. McNeil-Watson, and U. Nobbmann. 2008. "Measuring Sub Nanometre Sizes Using Dynamic Light Scattering." *Journal of Nanoparticle Research* 10 (5): 823–829. doi:10.1007/s11051-007-9317-4

Ke, P. C., S. Lin, W. J. Parak, T. P. Davis, and F. Caruso. 2017. "A Decade of the Protein Corona." *ACS Nano* 11 (12): 11773–11776. doi:10.1021/acsnano.7b08008

Kennedy, I. M., D. Wilson, and A. I. Barakat; HEI Health Review Committee. 2009. "Uptake and Inflammatory Effects of Nanoparticles in a Human Vascular Endothelial Cell Line." *Research reports - Health Effects Institute* 136: 3–32.

Kettiger, H., A. Schipanski, P. Wick, and J. Huwyler. 2013. "Engineered Nanomaterial Uptake and Tissue Distribution: From Cell to Organism." *International Journal of Nanomedicine* 8: 3255–3269. doi:10.2147/IJN.S49770

Kievit, F. M., and M. Zhang. 2011. "Surface Engineering of Iron Oxide Nanoparticles for Targeted Cancer Therapy." *Accounts of Chemical Research* 44 (10): 853–862. doi:10.1021/ar2000277

Kim, I.-Y., E. Joachim, H. Choi, and K. Kim. 2015. "Toxicity of Silica Nanoparticles Depends on Size, Dose, and Cell Type." *Nanomedicine: Nanotechnology, Biology, and Medicine* 11 (6): 1407–1416. doi:10.1016/j.nano.2015.03.004

Krug, H. F. 2014. "Nanosafety Research – Are We On the Right Track?" *Angewandte Chemie (International Ed. In English)* 53 (46): 12304–12319. doi:10.1002/anie.201403367

Krug, H. F., and P. Wick. 2011. "Nanotoxicology: An Interdisciplinary Challenge." *Angewandte Chemie International Edition* 50 (6): 1260–1278. doi:10.1002/anie.201001037

Laux, P., C. Riebeling, A. M. Booth, J. D. Brain, J. Brunner, C. Cerrillo, O. Creutzenberg, I. Estrela-Lopis, T. Gebel, G. Johanson, et al. 2017. "Biokinetics of Nanomaterials: The Role of Biopersistence." *NanoImpact* 6: 69–80. doi:10.1016/j.impact.2017.03.003

Lee, J. H., Y. S. Kim, K. S. Song, H. R. Ryu, J. H. Sung, J. D. Park, H. M. Park, N. W. Song, B. S. Shin, D. Marshak, et al. 2013. "Biopersistence of Silver Nanoparticles in Tissues from Sprague–Dawley Rats." *Particle and Fibre Toxicology* 10 (1): 36. doi:10.1186/1743-8977-10-36

Li, L. K. Y. Mak, J. Shi, C. H. Leung, C. M. Wong, C. W. Leung, C. S. K. Mak, K. Y. Chan, N. M. M. Chan, E. X. Wu, and P. W. T. Pong. 2013. "Sterilization on Dextran-Coated Iron Oxide Nanoparticles: Effects of Autoclaving, Filtration, UV Irradiation, and Ethanol Treatment." *Microelectronic Engineering* 111: 310–313. doi:10.1016/j.mee.2013.02.021

Li, T., A. J. Senesi, and B. Lee. 2016. "Small Angle X-Ray Scattering for Nanoparticle Research." *Chemical Reviews* 116 (18): 11128–11180. doi:10.1021/acs.chemrev.5b00690

Li, Y., and D. Boraschi. 2016. "Endotoxin Contamination: A Key Element in the Interpretation of Nanosafety Studies." *Nanomed* 11 (3): 269–287. doi:10.2217/nnm.15.196

Li, Z., Y. Zhang, D. Zhu, S. Li, X. Yu, Y. Zhao, X. Ouyang, Z. Xie, and L. Li. 2017. "Transporting Carriers for Intracellular Targeting Delivery via Non-Endocytic Uptake Pathways." *Drug Delivery* 24 (2): 45–55. doi:10.1080/10717544.2017.1391889

Lovestam, G. 2010. "Considerations on a Definition of Nanomaterial for Regulatory Purposes." [WWW Document]. Accessed 28 August 2017. https://ec.europa.eu/jrc/sites/jrcsh/files/jrc_reference_report_201

Lu, M., M. H. Cohen, D. Rieves, and R. Pazdur. 2010. "FDA Report: Ferumoxytol for Intravenous Iron Therapy in Adult Patients with Chronic Kidney Disease." *American Journal of Hematology* 85 (5): 315–319. doi:10.1002/ajh.21656

Maguire, C. M., Sillence, K. Roesslein, M. Hannell, C. Suarez, G. Sauvain, J.-J. Capracotta, S. Contal, S. Cambier, S. El Yamani. N. et al., 2017. "Benchmark of Nanoparticle Tracking Analysis on Measuring Nanoparticle Sizing and Concentration." *Journal of Micro and Nano-Manufacturing* 5 (4): 041002–041010. doi:10.1115/1.4037124

Mahmoudi, M., H. Hofmann, B. Rothen-Rutishauser, and A. Petri-Fink. 2012. "Assessing the in Vitro and in Vivo Toxicity of Superparamagnetic Iron Oxide Nanoparticles." *Chemical Reviews* 112 (4): 2323–2338. doi:10.1021/cr2002596

Mansfield, E., K. M. Tyner, C. M. Poling, and J. L. Blacklock. 2014. "Determination of Nanoparticle Surface Coatings and Nanoparticle Purity Using Microscale Thermogravimetric Analysis." *Analytical Chemistry* 86: 1478–1484. doi:10.1021/ac402888v

McCormack, P. L. 2012. "Ferumoxytol: In Iron Deficiency Anaemia in Adults with Chronic Kidney Disease." *Drugs* 72: 2013–2022. doi:10.2165/11209880-000000000-00000

Mehn, D., F. Caputo, M. Rösslein, L. Calzolai, F. Saint-Antonin, T. Courant, P. Wick, and D. Gilliland. 2017. "Larger or More? Nanoparticle Characterisation Methods for Recognition of Dimers." *RSC Advances* 7 (44): 27747–27754. doi:10.1039/C7RA02432K

Meng, J., M. Yang, F. Jia, Z. Xu, H. Kong, and H. Xu. 2011. "Immune Responses of BALB/c Mice to Subcutaneously Injected Multi-Walled Carbon Nanotubes." *Nanotoxicology* 5 (4): 583–591. doi:10.3109/17435390.2010.523483

Moghimi, S. M., and D. Simberg. 2017. "Complement Activation Turnover on Surfaces of Nanoparticles." *Nano Today* 15: 8–10. doi:10.1016/j.nantod.2017.03.001

Moore, T. L., L. Rodriguez-Lorenzo, V. Hirsch, S. Balog, D. Urban, C. Jud, B. Rothen-Rutishauser, M. Lattuada, and A. Petri-Fink. 2015. "Nanoparticle Colloidal Stability in Cell Culture Media and Impact on Cellular Interactions." *Chemical Society Reviews* 44 (17): 6287–6305. doi:10.1039/C4CS00487F

Mühlebach, S., G. Borchard, and S. Yildiz. 2015. "Regulatory Challenges and Approaches to Characterize Nanomedicines and Their Follow-on Similars." *Nanomed* 10 (4): 659–674. doi:10.2217/nnm.14.189

Nair, A. B., and S. Jacob. 2016. "A Simple Practice Guide for Dose Conversion between Animals and Human." *Journal of Basic and Clinical Pharmacy* 7 (2): 27–31. doi:10.4103/0976-0105.177703

Navya, P. N., and H. K. Daima. 2016. "Rational Engineering of Physicochemical Properties of Nanomaterials for Biomedical Applications with Nanotoxicological Perspectives." *Nano Converg* 3 (1): 1. doi:10.1186/s40580-016-0064-z

Neagu, M., Z. Piperigkou, K. Karamanou, A. B. Engin, A. O. Docea, C. Constantin, C. Negrei, D. Nikitovic, and A. Tsatsakis. 2017. "Protein Bio-Corona: critical Issue in Immune Nanotoxicology." *Archives of Toxicology* 91 (3): 1031–1048. doi:10.1007/s00204-016-1797-5

Nel, A., T. Xia, L. Mädler, and N. Li. 2006. "Toxic Potential of Materials at the Nanolevel." *Science* 311 (5761): 622–627. doi:10.1126/science.1114397

Nemmar, A., P. Yuvaraju, S. Beegam, J. Yasin, E. E. Kazzam, and B. H. Ali. 2016. "Oxidative Stress, Inflammation, and DNA Damage in Multiple Organs of Mice Acutely Exposed to Amorphous Silica Nanoparticles." *International Journal of Nanomedicine* 11: 919–928. doi:10.2147/IJN.S92278

NSCT/CoT/NSET. 2014. "2014 NNI Strategic Plan | Nano." [WWW Document]. Accessed August 23 2017. https://www.nano.gov/node/1113

Oberdörster, G. 2010. "Safety Assessment for Nanotechnology and Nanomedicine: concepts of Nanotoxicology."

Journal of Internal Medicine 267 (1): 89–105. doi:10.1111/j.1365-2796.2009.02187.x

Oberdörster, G., V. Stone, and K. Donaldson. 2007. "Toxicology of Nanoparticles: A Historical Perspective." *Nanotoxicology* 1 (1): 2–25. doi:10.1080/17435390701314761

Oh, N., and J.-H. Park. 2014. "Endocytosis and Exocytosis of Nanoparticles in Mammalian Cells." *International Journal of Nanomedicine* 9: 51–63. doi:10.2147/IJN.S26592

Oomen, A. G., E. A. J. Bleeker, P. M. J. Bos, F. van Broekhuizen, S. Gottardo, M. Groenewold, D. Hristozov, K. Hund-Rinke, M.-A. Irfan, A. Marcomini, et al. 2015. "Grouping and Read-across Approaches for Risk Assessment of Nanomaterials." *International Journal of Environmental Research and Public Health* 12 (10): 13415–13434. doi:10.3390/ijerph121013415

Panchal, J., J. Kotarek, E. Marszal, and E. M. Topp. 2014. "Analyzing Subvisible Particles in Protein Drug Products: A Comparison of Dynamic Light Scattering (DLS) and Resonant Mass Measurement (RMM)." *The AAPS Journal* 16 (3): 440–451. doi:10.1208/s12248-014-9579-6

Park, J.-B. 2003. "Phagocytosis Induces Superoxide Formation and Apoptosis in Macrophages." *Experimental & Molecular Medicine* 35 (5): 325–335. doi:10.1038/emm.2003.44

Park, M. V. D. Z., A. M. Neigh, J. P. Vermeulen, L. J. J. de la Fonteyne, H. W. Verharen, J. J. Briedé, H. van Loveren, and W. H. de Jong. 2011. "The Effect of Particle Size on the Cytotoxicity, Inflammation, Developmental Toxicity and Genotoxicity of Silver Nanoparticles." *Biomaterials* 32 (36): 9810–9817. doi:10.1016/j.biomaterials.2011.08.085

Pelaz, B., C. Alexiou, R. A. Alvarez-Puebla, F. Alves, A. M. Andrews, S. Ashraf, L. P. Balogh, L. Ballerini, A. Bestetti, C. Brendel, et al. 2017. "Diverse Applications of Nanomedicine." *ACS Nano* 11 (3): 2313–2381. doi:10.1021/acsnano.6b06040

Potočnik, J. 2011. "Commission Recommendation of 18 October 2011 on the Definition Of Nanomaterial 2011/696/EU." Accessed 28 August 2017. https://eur-lex.europa.eu/legal-content/EN/ALL/?uri=CELEX:32011H0696

Puri, A., K. Loomis, B. Smith, J.-H. Lee, A. Yavlovich, E. Heldman, and R. Blumenthal. 2009. "Lipid-Based Nanoparticles as Pharmaceutical Drug Carriers: From Concepts to Clinic." *Critical Reviews in Therapeutic Drug Carrier Systems* 26 (6): 523–580. doi:10.1615/CritRevTherDrugCarrierSyst.v26.i6.10

Pyrz, W. D., and D. J. Buttrey. 2008. "Particle Size Determination Using TEM: A Discussion of Image Acquisition and Analysis for the Novice Microscopist." *Langmuir* 24 (20): 11350–11360. doi:10.1021/la801367j

Rao, A., M. Schoenenberger, E. Gnecco, T. Glatzel, E. Meyer, D. Brändlin, and L. Scandella. 2007. "Characterization of Nanoparticles Using Atomic Force Microscopy." *Journal of Physics: Conference Series* 61: 971. doi:10.1088/1742-6596/61/1/192

Roberson, S., and G. J. Weltje. 2014. "Inter-Instrument Comparison of Particle-Size Analysers." *Sedimentology* 61 (4): 1157–1174. doi:10.1111/sed.12093

Robertson, J. D., L. Rizzello, M. Avila-Olias, J. Gaitzsch, C. Contini, M. S. Magoń, S. A. Renshaw, and G. Battaglia. 2016. "Purification of Nanoparticles by Size and Shape." *Scientific Reports* 6 (1): 27494. doi:10.1038/srep27494

Ros, P. R., P. C. Freeny, S. E. Harms, S. E. Seltzer, P. L. Davis, T. W. Chan, A. E. Stillman, L. R. Muroff, V. M. Runge, and M. A. Nissenbaum. 1995. "Hepatic MR Imaging with Ferumoxides: A Multicenter Clinical Trial of the Safety and Efficacy in the Detection of Focal Hepatic Lesions." *Radiology* 196 (2): 481–488. doi:10.1148/radiology.196.2.7617864

Sabella, S. R. P. Carney, V. Brunetti, M. A. Malvindi, N. Al-Juffali, G. Vecchio, S. M. Janes, O. M. Bakr, R. Cingolani, F. Stellacci, and P. P. Pompa. 2014. "A General Mechanism for Intracellular Toxicity of Metal-Containing Nanoparticles." [†Electronic Supplementary Information (ESI) available. See doi:10.1039/c4nr01234h Click here for additional data file.] *Nanoscale* 6: 7052–7061.

Saraiva, C., C. Praça, R. Ferreira, T. Santos, L. Ferreira, and L. Bernardino. 2016. "Nanoparticle-Mediated Brain Drug Delivery: Overcoming Blood–Brain Barrier to Treat Neurodegenerative Diseases." *Journal of Controlled Release* 235: 34–47. doi:10.1016/j.jconrel.2016.05.044

Sayes, C. M., N. Banerjee, and A. A. Romoser. 2009. "The Role of Oxidative Stress in Nanotoxicology."In *General, Applied and Systems Toxicology*, edited by B. Ballantyne, T. C. Marrs, T. Syversen, D. A. Casciano and S. C. Sahu. Hoboken, New Jersey: John Wiley & Sons, Ltd. doi:10.1002/9780470744307.gat245

Sayes, C. M., P. A. Smith, and I. V. Ivanov. 2013. "A Framework for Grouping Nanoparticles Based on Their Measurable Characteristics." *International Journal of Nanomedicine* 8: 45–56. doi:10.2147/IJN.S40521

Scott-Fordsmand, J. J., S. Pozzi-Mucelli, L. Tran, K. Aschberger, S. Sabella, U. Vogel, C. Poland, D. Balharry, T. Fernandes, S. Gottardo, et al. 2014. "A Unified Framework for Nanosafety Is Needed." *Nano Today* 9 (5): 546–549. doi:10.1016/j.nantod.2014.07.001

Seaton, A., L. Tran, R. Aitken, and K. Donaldson. 2010. "Nanoparticles, Human Health Hazard and Regulation." *Journal of the Royal Society Interface* 7 (Suppl_1): S119–S129. doi:10.1098/rsif.2009.0252.focus

Serpone, N., and S. Horikoshi. 2013. "Microwaves in Nanoparticle Synthesis: Fundamentals and Applications." [WWW Document]. Accessed August 28 2017. http://www.wiley.com/WileyCDA/WileyTitle/productCd-3527331 972.html

Shannahan, J. 2017. "The Biocorona: A Challenge for the Biomedical Application of Nanoparticles." *Nanotechnology Reviews* 6: 345–353. doi:10.1515/ntrev-2016-0098

Shimizu, K., H. Nakamura, and S. Watano. 2016. "MD Simulation Study of Direct Permeation of a Nanoparticle across the Cell Membrane under an External Electric Field." *Nanoscale* 8 (23): 11897–11906. doi:10.1039/C6NR02051H

Shvedova, A. A., V. E. Kagan, and B. Fadeel. 2010. "Close Encounters of the Small Kind: adverse Effects of Man-

Made Materials Interfacing with the Nano-Cosmos of Biological Systems." *Annual Review of Pharmacology and Toxicology* 50 (1): 63–88. doi:10.1146/annurev.pharmtox.010909.105819

Siegrist, S., H. Kettiger, E. Fasler-Kan, and J. Huwyler. 2017. "Selective Stimulation of the JAK/STAT Signaling Pathway by Silica Nanoparticles in Human Endothelial Cells." *Toxicology In Vitro* 42: 308–318. doi:10.1016/j.tiv.2017.05.002

Simkó, M., D. Nosske, and W. G. Kreyling. 2014. "Metrics, Dose, and Dose Concept: The Need for a Proper Dose Concept in the Risk Assessment of Nanoparticles." *International Journal of Environmental Research and Public Health* 11 (4): 4026–4048. doi:10.3390/ijerph110404026

Simkó, M., S. Tischler, and M.-O. Mattsson. 2015. "Pooling and Analysis of Published in Vitro Data: A Proof of Concept Study for the Grouping of Nanoparticles." *International Journal of Molecular Sciences* 16 (11): 26211–26236. doi:10.3390/ijms161125954

Singh, A. K. 2015. *Engineered Nanoparticles: Structure, Properties and Mechanisms of Toxicity*. Cambridge, Massachusetts: Academic Press.

Singh, N., G. J. Jenkins, R. Asadi, and S. H. Doak. 2010. "Potential Toxicity of Superparamagnetic Iron Oxide Nanoparticles (SPION)." *Nano Rev* 1 (1): 5358. doi:10.3402/nano.v1i0.5358

Stone, V., S. Pozzi-Mucelli, L. Tran, K. Aschberger, S. Sabella, U. Vogel, C. Poland, D. Balharry, T. Fernandes, S. Gottardo, et al. 2014. "ITS-NANO - Prioritising Nanosafety Research to Develop a Stakeholder Driven Intelligent Testing Strategy." *Particle and Fibre Toxicology* 11 (1): 9. doi:10.1186/1743-8977-11-9

Szebeni, J., S. Fishbane, M. Hedenus, S. Howaldt, F. Locatelli, S. Patni, D. Rampton, G. Weiss, and J. Folkersen. 2015. "Hypersensitivity to Intravenous Iron: classification, Terminology, Mechanisms and Management." *British Journal of Pharmacology* 172 (21): 5025–5036. doi:10.1111/bph.13268

Tämm, K., L. Sikk, J. Burk, R. Rallo, S. Pokhrel, L. Mädler, J. J. Scott-Fordsmand, P. Burk, and T. Tamm. 2016. "Parametrization of Nanoparticles: development of Full-Particle Nanodescriptors." *Nanoscale* 8 (36): 16243–16250. doi:10.1039/C6NR04376C

Teeguarden, J. G., P. M. Hinderliter, G. Orr, B. D. Thrall, and J. G. Pounds. 2007. "Particokinetics in Vitro: dosimetry Considerations for in Vitro Nanoparticle Toxicity Assessments." *Toxicological Sciences* 95 (2): 300–312. doi:10.1093/toxsci/kfl165

Tiwari, D., J. Takashi, and J. Behari. 2010. "Dose-Dependent In-Vivo Toxicity Assessment of Nanoparticle in Wistar Rats." *Toxicology Mechanisms and Methods* 21 (1): 13–24. doi:10.3109/15376516.2010.529184

Toy, R., L. Bauer, C. Hoimes, K. B. Ghaghada, and E. Karathanasis. 2014. "Targeted Nanotechnology for Cancer Imaging." *Advanced Drug Delivery Reviews* 76: 79–97. doi:10.1016/j.addr.2014.08.002

Treuel, L., D. Docter, M. Maskos, and R. H. Stauber. 2015. "Protein Corona – from Molecular Adsorption to Physiological Complexity." *Beilstein Journal of Nanotechnology* 6: 857–873. doi:10.3762/bjnano.6.88

Turner, P. V., T. Brabb, C. Pekow, and M. A. Vasbinder. 2011. "Administration of Substances to Laboratory Animals: Routes of Administration and Factors to Consider." *Journal of the American Association for Laboratory Animal Science* 50 (5): 600–613.

Unfried, K., C. Albrecht, L.-O. Klotz, A. Von Mikecz, S Grether-Beck, R.P.F. Schins. 2007. "Cellular responses to nanoparticles: Target structures and mechanisms." *Nanotoxicology* 1: 52–71. doi:10.1080/00222930701314932

Unterweger, H., C. Janko, M. Schwarz, L. Dézsi, R. Urbanics, J. Matuszak, E. Őrfi, T. Fülöp, T. Bäuerle, J. Szebeni. et al. 2017. "Non-Immunogenic Dextran-Coated Superparamagnetic Iron Oxide Nanoparticles: A Biocompatible, Size-Tunable Contrast Agent for Magnetic Resonance Imaging." *International Journal of Nanomedicine* 12: 5223–5238. doi:10.2147/IJN.S138108

Uskoković, V. 2013. "Entering the Era of Nanoscience: Time to Be so Small." *Journal of Biomedical Nanotechnology* 9 (9): 1441–1470. doi:10.1166/jbn.2013.1642

van Teunenbroek, T. 2017. "NANoREG, A Common European Approach to the Regulatory Testing of Nanomaterials." [WWW Document]. www.nanoreg.eu. Accessed December 21 2017. http://www.rivm.nl/en/About_RIVM/Mission_and_strategy/International_Affairs/International_Projects/Completed/NANoREG/NANoREG_Results_Repository_sub_page_Final_Report

Verhoef, J. J., and T. J. Anchordoquy. 2013. "Questioning the Use of PEGylation for Drug Delivery. Drug Deliv." *Drug Delivery and Translational Research* 3 (6): 499–503. doi:10.1007/s13346-013-0176-5

Vermeij, E. A., M. I. Koenders, M. B. Bennink, L. A. Crowe, L. Maurizi, J.-P. Vallée, H. Hofmann, W. B. Berg, L. van den, P. L. E. M. van, Loo, and F. A. J. van de. 2015. "The in-Vivo Use of Superparamagnetic Iron Oxide Nanoparticles to Detect Inflammation Elicits a Cytokine Response but Does Not Aggravate Experimental Arthritis." *PLoS One* 10 (5): e0126687. doi:10.1371/journal.pone.0126687

Vetten, M. A., C. S. Yah, T. Singh, and M. Gulumian. 2014. "Challenges Facing Sterilization and Depyrogenation of Nanoparticles: effects on Structural Stability and Biomedical Applications." *Nanomedicine: Nanotechnology, Biology, and Medicine* 10 (7): 1391–1399. doi:10.1016/j.nano.2014.03.017

Vippola, M., M. Valkonen, E. Sarlin, M. Honkanen, and H. Huttunen. 2016. "Insight to Nanoparticle Size Analysis—Novel and Convenient Image Analysis Method versus Conventional Techniques." *Nanoscale Research Letters* 11 (1): 169. doi:10.1186/s11671-016-1391-z

Weinstein, J. S., C. G. Varallyay, E. Dosa, S. Gahramanov, B. Hamilton, W. D. Rooney, L. L. Muldoon, and E. A. Neuwelt. 2010. "Superparamagnetic Iron Oxide Nanoparticles: diagnostic Magnetic Resonance Imaging and Potential Therapeutic Applications in Neurooncology and Central Nervous System Inflammatory Pathologies, A Review."

Journal of Cerebral Blood Flow & Metabolism 30 (1): 15–35. doi:10.1038/jcbfm.2009.192

Weissig, V., T. K. Pettinger, and N. Murdock. 2014. "Nanopharmaceuticals (Part 1): Products on the Market." *International Journal of Nanomedicine* 9: 4357–4373. doi:10.2147/IJN.S46900

Weissleder, R., M. Nahrendorf, and M. J. Pittet. 2014. "Imaging Macrophages with Nanoparticles." *Nature Materials* 13 (2): 125–138. doi:10.1038/nmat3780

Wen, H., M. Dan, Y. Yang, J. Lyu, A. Shao, X. Cheng, L. Chen, and L. Xu. 2017. "Acute Toxicity and Genotoxicity of Silver Nanoparticle in Rats." *PLoS One* 12 (9): e0185554. doi:10.1371/journal.pone.0185554

Whitesides, G. M. 2003. "The "Right" Size in Nanobiotechnology." *Nature Biotechnology* 21 (10): 1161–1165. doi:10.1038/nbt872

Witzigmann, D., M. Camblin, J. Huwyler, and V. Balasubramanian. 2015. "Nanomaterials: Therapeutic Applications."In *The Encyclopedia of Biomedical Polymers & Polymeric Biomaterials*, edited by M. Mishra, 5364–5378. New York: Taylor & Francis.

Wolfram, J., M. Zhu, Y. Yang, J. Shen, E. Gentile, D. Paolino, M. Fresta, G. Nie, C. Chen, H. Shen. et al. 2015. "Safety of Nanoparticles in Medicine." *Current Drug Targets* 16 (14): 1671–1681. doi:10.2174/1389450115666140804124808

Wu, X., Z.-R. Lu. 2016. "Nanoparticle–Tissue Interaction.." In *Nanomaterials in Pharmacology. Methods in Pharmacology and Toxicology*, edited by Z.-R. Lu, S. Sakuma, 201–218. New York, NY: Humana Press. doi:10.1007/978-1-4939-3121-7

Xie, J., S. Lee, and X. Chen. 2010. "Nanoparticle-Based Theranostic Agents." *Advanced Drug Delivery Reviews* 62 (11): 1064–1079. doi:10.1016/j.addr.2010.07.009

Yameen, B., W. I. Choi, C. Vilos, A. Swami, J. Shi, and O. C. Farokhzad. 2014. "Insight into Nanoparticle Cellular Uptake and Intracellular Targeting." *30th Anniversary Special Issue* 190: 485–499. doi:10.1016/j.jconrel.2014.06.038

Yang, Y., Z. Qin, W. Zeng, T. Yang, Y. Cao, C. Mei, and Y. Kuang. 2017. "Toxicity Assessment of Nanoparticles in Various Systems and Organs." *Nanotechnology Reviews* 6: 279. doi:10.1515/ntrev-2016-0047

Yildirimer, L., N. T. K. Thanh, M. Loizidou, and A. M. Seifalian. 2011. "Toxicology and Clinical Potential of Nanoparticles." *Nano Today* 6 (6): 585–607. doi:10.1016/j.nantod.2011.10.001

Yuan, S. Y., and R. R. Rigor. 2010. *The Endothelial Barrier*. San Rafael, California: Morgan & Claypool Life Sciences.

Zaloga, J., C. Janko, J. Nowak, J. Matuszak, S. Knaup, D. Eberbeck, R. Tietze, H. Unterweger, R. P. Friedrich, S Duerr, et al. 2014. "Development of a Lauric Acid/Albumin Hybrid Iron Oxide Nanoparticle System with Improved Biocompatibility." *International Journal of Nanomedicine* 9: 4847–4866. doi:10.2147/IJN.S68539

Zhang, H., Z. Ji, T. Xia, H. Meng, C. Low-Kam, R. Liu, S. Pokhrel, S. Lin, X. Wang, Y.-P. Liao, et al. 2012. "Use of Metal Oxide Nanoparticle Band Gap to Develop a Predictive Paradigm for Oxidative Stress and Acute Pulmonary Inflammation." *ACS Nano* 6 (5): 4349–4368. doi:10.1021/nn3010087

Zhang, S., J. Li, G. Lykotrafitis, G. Bao, and S. Suresh. 2009. "Size-Dependent Endocytosis of Nanoparticles." *Advanced Materials* 21 (4): 419–424. doi:10.1002/adma.200801393

Zhao, L., A. Seth, N. Wibowo, C.-X. Zhao, N. Mitter, C. Yu, and A. P. J. Middelberg. 2014. "Nanoparticle Vaccines." *Vaccine* 32 (3): 327–337. doi:10.1016/j.vaccine.2013.11.069

Zheng, J., J. D. Clogston, A. K. Patri, M. A. Dobrovolskaia, and S. E. McNeil. 2011. "Sterilization of Silver Nanoparticles Using Standard Gamma Irradiation Procedure Affects Particle Integrity and Biocompatibility." *Journal of Nanomedicine & Nanotechnology* S5 (01): 001. doi:10.4172/2157-7439.S5-001

II. Shedding Light on Metal-Based Nanoparticles in Zebrafish by Computed Tomography with Micrometer Resolution

Emre Cörek, Griffin Rodgers, Stefan Siegrist, Tomaz Einfalt, Pascal Detampel, Christian M. Schlepütz, Sandro Sieber, Pascal Fluder, Georg Schulz, Harald Unterweger, Christoph Alexiou, Bert Müller, Maxim Puchkov, Jörg Huwyler

Journal: published in SMALL (2020), early view

DOI: https://doi.org/10.1002/smll.202000746

NANO · MICRO small
www.small-journal.com

Shedding Light on Metal-Based Nanoparticles in Zebrafish by Computed Tomography with Micrometer Resolution

*Emre Cörek, Griffin Rodgers, Stefan Siegrist, Tomaz Einfalt, Pascal Detampel, Christian M. Schlepütz, Sandro Sieber, Pascal Fluder, Georg Schulz, Harald Unterweger, Christoph Alexiou, Bert Müller, Maxim Puchkov, and Jörg Huwyler**

Metal-based nanoparticles are clinically used for diagnostic and therapeutic applications. After parenteral administration, they will distribute throughout different organs. Quantification of their distribution within tissues in the 3D space, however, remains a challenge owing to the small particle diameter. In this study, synchrotron radiation-based hard X-ray tomography (SRμCT) in absorption and phase contrast modes is evaluated for the localization of superparamagnetic iron oxide nanoparticles (SPIONs) in soft tissues based on their electron density and X-ray attenuation. Biodistribution of SPIONs is studied using zebrafish embryos as a vertebrate screening model. This label-free approach gives rise to an isotropic, 3D, direct space visualization of the entire 2.5 mm-long animal with a spatial resolution of around 2 μm. High resolution image stacks are available on a dedicated internet page (http://zebrafish.pharma-te.ch). X-ray tomography is combined with physico-chemical characterization and cellular uptake studies to confirm the safety and effectiveness of protective SPION coatings. It is demonstrated that SRμCT provides unprecedented insights into the zebrafish embryo anatomy and tissue distribution of label-free metal oxide nanoparticles.

1. Introduction

Engineered metal-based nanoparticles are increasingly used for medical applications, notably in the field of biomedical imaging.[1,2] In most cases, they consist of a metal or metal oxide core and a coating of organic materials such as polysaccharides, polypeptides, proteins, fatty acids or polyethyleneglycol (PEG) for chemical and colloidal stabilization.[3] Prominent examples are superparamagnetic iron oxide nanoparticles (SPIONs) which are clinically used as magnetic resonance imaging contrast agents.[4] In addition, application of an (alternating) external magnetic field for therapeutic purposes offers interesting perspectives in oncology, in that such nanoparticles can be used for a hyperthermia therapy or to target drug loaded particles to tumors. The latter is referred to as magnetic drug targeting.[5] In order to study the in vivo biodistribution of such particles, they have to be labeled by conjugation of fluorescent or radioactive agents. However, these chemical modifications can significantly change the interaction patterns with biological matter since they have a direct impact on particle size and polydispersity, electrokinetic potential (ζ-potential), and possibly the protein corona.[6–9] It is therefore recommended to carry out, whenever possible, physicochemical characterization, formulation development, pharmacokinetic studies, and hazard and safety evaluations with non-tagged nanoparticles.[10] In recent years, magnetic particle imaging (MPI), magnetic resonance imaging (MRI) or computed tomography[11] have been discussed as label-free alternative to trace engineered metal nanoparticles within a biological system. The latter technology takes advantage of their strong X-ray absorption.[12,13] In medical research, laboratory-based micro-computed tomography (μCT) has been used to monitor the biodistribution of metal-based nanoparticles in vitro or in small experimental animals.[13–16] A challenge

Dr. E. Cörek, Dr. S. Siegrist, Dr. T. Einfalt, Dr. P. Detampel, Dr. S. Sieber, P. Fluder, Dr. M. Puchkov, Prof. J. Huwyler
Department of Pharmaceutical Technology
University of Basel
Klingelbergstrasse. 50, Basel 4056, Switzerland
E-mail: joerg.huwyler@unibas.ch

The ORCID identification number(s) for the author(s) of this article can be found under https://doi.org/10.1002/smll.202000746.

DOI: 10.1002/smll.202000746

G. Rodgers, Dr. G. Schulz, Prof. B. Müller
Biomaterials Science Center
Department of Biomedical Engineering
University of Basel
E-mail: Gewerbestrasse 14, Allschwil 4123, Switzerland

Dr. C. M. Schlepütz
Swiss Light Source
Paul Scherrer Institute
Forschungsstrasse 111, Villigen 5232, Switzerland

Dr. H. Unterweger, Prof. C. Alexiou
Department of Otorhinolaryngology
Head and Neck Surgery, Section for Experimental Oncology and Nanomedicine (SEON), Else Kröner-Fresenius Stiftung Professorship
Erlangen University of Erlangen
Waldstraße 1, Erlangen 91054, Germany

is thereby the combination of a large field-of-view (to image an entire animal) and a relatively low resolution of the used detector arrays in the order of a few thousand pixels in width. In addition, large administered doses are needed to overcome density resolution limits, despite the fact that high doses may cause artefacts. Therefore, detecting medically relevant metal-based nanoparticle concentrations within intact whole-body samples remains a major challenge.

It was therefore the aim of the present study to address these issues by using synchrotron radiation-based micro computed tomography (SRμCT) in phase and absorption contrast modalities to study the biodistribution of non-labeled SPIONs within a soft tissue sample. To this end, the zebrafish embryo was used as a test system. The zebrafish embryo has been widely discussed as predictive vertebrate screening model for nanotoxicology in recent years.[17,18] It has several benefits over alternative in vivo models such as optical transparency, 78% genetic homology with humans, cost-efficiency, small size (less than 0.5 mm in diameter, less than 5 mm in length), and an immune system similar to humans.[19] Our team has extensively used zebrafish embryos to study the pharmacokinetics and tissue distribution of particulate drug carriers.[20] SRμCT offers higher density and spatial resolution than conventional laboratory μCT thanks to higher brilliance. It should be noted that the high intensity synchrotron X-ray beam allows for incorporation of a monochromator providing a tunable beam source. Consequently, no beam hardening correction is necessary to obtain quantitative absorption data and phase contrast accessibility.[21] In this study, we demonstrate that low doses of sterically stabilized SPIONs can indeed be localized within the whole zebrafish embryo by SRμCT. The offered micrometer resolution allowed for detailed 3D image reconstruction of the small (≈2.5 mm) vertebrate embryos. Furthermore, it was possible to detect within these soft tissue specimens deposits of iron oxide nanoparticles.

2. Results

2.1. Synthesis of SPIONs

Coating of iron oxide nanoparticles is important to ensure colloidal stability in solution and to prevent particle erosion.[3] The iron oxide core of the SPIONs was synthesized by co-precipitation in a one-pot synthesis resulting in particles with a narrow particle size distribution.[22] Subsequently, four types of surface modifications were introduced. Hydrophilic macromolecules, that is, dextran and human serum albumin, were deposited on the SPION surface giving rise to HSA-SPIONs[23] or Dex-SPIONs.[24] Alternatively, particles were embedded within a phospholipid bilayer (Lipid-SPIONs) or a lipid shell containing pegylated phospholipids (sterically stabilized Lipid-PEG-SPIONs) using a microfluidics approach.[25]

Reference particles were fluorescent labeled in the case of Lipid-SPIONs and Lipid-PEG-SPIONs. HSA-SPIONs and Dex-SPIONs were produced using good manufacturing practice (GMP) compliant protocols. It was therefore neither desired nor possible to deviate from the manufacturing process and to introduce a fluorescent label.

Table 1. Physico-chemical characterization of superparamagnetic iron oxide nanoparticles (SPIONs). Human serum albumin coated iron oxide nanoparticles (HSA-SPIONs), Dextran-coated iron oxide nanoparticles (Dex-SPIONs), phospholipid embedded iron oxide nanoparticles (Lipid-SPIONs), and modified phospholipid embedded iron oxide nanoparticles with PEG of molecular weight 5000 (Lipid-PEG-SPIONs) were characterized by dynamic and electrophoretic light scattering. Hydrodynamic diameter, polydispersity index (PDI), and the electrokinetic potential (ζ-potential) of the particles were determined using phosphate-buffered saline as a diluent. Where indicated, particles were fluorescent labeled. Values are means ± SD, $n = 3$.

Particle	Hydrodynamic diameter [nm]	PDI[a)]	ζ-potential [mV]	Fluorescent label
HSA-SPIONs	61 ± 0.4	0.14	−35.7 ± 1.0	No
Dex-SPIONs	70 ± 0.3	0.17	−18.4 ± 3.1	No
Lipid-SPIONs	100.8 ± 0.6	0.26	−42.3 ± 2.8	No
Lipid-PEG-SPIONs	89.2 ± 0.5	0.23	−22.5 ± 1.2	No
Lipid-SPIONs	91 ± 0.5	0.24	−41.6 ± 2.0	Yes
Lipid-PEG-SPIONs	81.5 ± 0.5	0.22	−20.6 ± 1.4	Yes

[a)]Mean PDI values, SD was ≤0.01.

2.2. Physico-Chemical Characterization of SPIONs

The physico-chemical characterization of SPIONs (**Table 1**) was based on dynamic light scattering, electrophoretic light scattering (ζ-potential determination), and transmission electron microscopy.

Nanoparticles used in the present study had a hydrodynamic diameter below 100 nm and a monodisperse size distribution (PDI ≈ 0.2). All particles were anionic with a ζ-potential of at least −18 mV. Due to a high colloidal stability, they could be stored for prolonged periods of time (>1 month at 4 °C). Fluorescent labeling of the particles had a minor impact on their basic physicochemical characteristics.

The size, morphology and colloidal stability of stabilized SPIONs was visualized by transmission electron microscopy (**Figure 1**). Uncoated SPIONs could not be analyzed due to flocculation and erosion. Agglomeration and degradation of these lipophilic and dense SPION cores can be minimized by appropriate particle coating, see Figure 1—the protein HSA (Figure 1A), the polysaccharide dextran (Figure 1B), phospholipids (Figure 1C), or a combination of phospholipids and PEG of molecular weight 5000 (Figure 1D).

2.3. Cellular Uptake and Cytotoxicity

Interactions of nanoparticles with cells of the immune system can drastically reduce their half-life in the circulation. Tissue resident macrophages will bind and internalize such nanoparticles leading to their accumulation in the liver and the spleen. These cellular interactions can be minimized by steric stabilization of the particles, that is, coating of their surface with hydrophilic polymers such as polyethylene glycol (PEG). In the present study, such interactions with cells of the immune system were studied in cell culture using the human monocytic cell line THP-1. Fluorescent labeled Lipid- and Lipid-PEG-SPIONs were incubated with THP-1 cells differentiated into immature dendritic cells. They were subsequently analyzed by confocal laser scanning

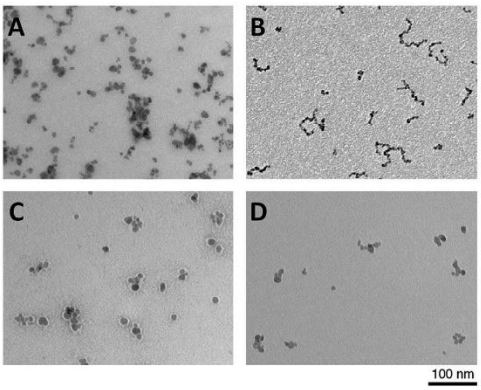

Figure 1. Transmission electron microscope images of SPIONs. Nanoparticles coated with A) human serum albumin (HSA-SPIONs), B) dextran (Dex-SPIONs), and embedded with C) phospholipids without PEG (Lipid-SPIONs), and D) phospholipids containing PEG of MW 5000 (Lipid-PEG-SPIONs). Particle characteristics are summarized in Table 1. Scale bars correspond to 100 nm.

microscopy (**Figure 2**A,B) and flow cytometry (Figure 2C). The phagocytic THP-1 cells rapidly internalize Lipid-SPIONs whereas sterically stabilized Lipid-PEG-SPIONs are not taken up due to the shielding effect of PEG. Qualitative fluorescent microcopy results were confirmed by quantitative flow cytometry analysis (Figure 2C). It should be emphasized, that this type of in vitro experiments can be performed only with fluorescent labeled particles. To exclude any cytotoxic effects of Lipid-SPIONs and Lipid-PEG-SPIONs, MTT, and Alamar blue viability assays were performed. Both lipid coated SPIONs had no negative impact on the viability of THP-1 cells (data not shown).

2.4. Light Microscopy-Based Visualization of SPIONs in the Zebrafish Embryo

In view of limitations imposed by cell culture-based test systems such as the THP-1 model, in vivo experiments were initiated using zebrafish embryos as a vertebrate screening model. Minute amounts of SPIONs (3 nL of a 4.8 mg mL^{-1} solution corresponding to a dose of less than 15 ng) were intravenously injected. Circulation and biodistribution of fluorescent nanoparticles in the zebrafish embryo 72 h post fertilization (hpf) was visualized by confocal microscopy (**Figure 3**A). Again, lipid-SPIONs and Lipid-PEG-SPIONs had to be labeled using the fluorescent, lipophilic, and cationic indocarbocyanine dye DiI (Figure 3B, red signal). To allow for a co-localization of nanoparticles, a transgenic zebrafish line (mpeg:kaede) expressing a green fluorescent protein within macrophages was used (Figure 3B, green signal). Macrophage uptake in vivo was detectable 24 h post injection in the caudal vein region of the embryo. A short half-life in the circulation and rapid sequestration of lipid-SPIONs by macrophages was observed. In contrast, pegylated nanoparticles (Lipid-PEG-SPIONs) had a long half-life in the circulation and apparently evaded macrophage uptake.

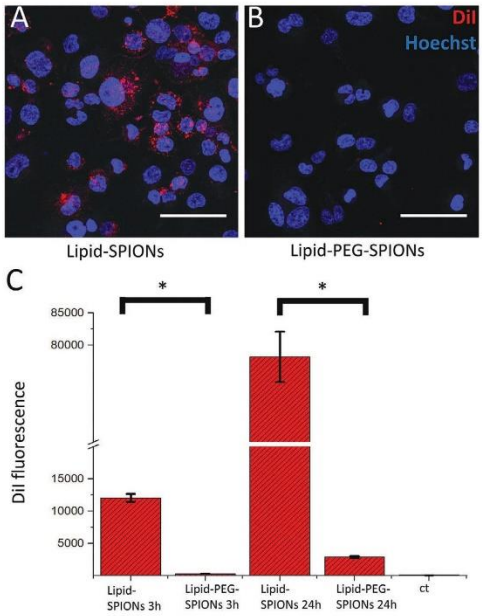

Figure 2. Cellular uptake of fluorescent labeled SPIONs by phagocytic THP-1 cells. Uptake of A) lipid-SPIONs or B) lipid-PEG-SPIONs by phagocytic THP-1 cells. Incubation for 3 h followed by confocal microscopy reveals intracellular location of SPIONs (red signal: DiI labeled SPIONs, blue signal: Hoechst 33342 staining of cell nuclei). Scale bars correspond to 60 µm. C) Quantitative analysis of cellular uptake of DiI labeled SPIONs by flow cytometry analysis after 3 and 24 h incubations. ct: untreated control cells. Values are means ± S.D., $n = 3$. *: Student's t-test, $p < 0.05$.

HSA-SPIONs and Dex-SPIONs used in the present study did not carry a fluorescent label. Therefore, particles had to be co-injected with Prussian blue to allow for an analysis by bright-field microscopy. This dye changes its color from brown to blue in presence of free iron, thus serving as an indicator to discriminate between SPIONs with an intact coating (Figure 3B, brown signal) or agglomerates of partially degraded particles (Figure 3B, blue signal). HSA-SPIONs did accumulate in a tissue compartment below the cardinal vein. A granular blue staining pattern was indicative of agglomeration and degradation. Dex-SPIONs could not be detected suggesting a good coating stability in vivo. To ensure that injected HSA-SPIONs did not cause toxic effects despite their degradation and the associated release of free iron, zebrafish embryo viability and malformation occurrence were monitored for up to 96 h post injection (Table S1, Supporting Information) to confirm absence of toxicity.

2.5. Hard X-Ray Tomography of SPION Biodistribution in Zebrafish Embryos

Exploratory experiments with two laboratory µCT instruments nanotom m (phoenix|x-ray, GE Sensing & Inspection Technologies

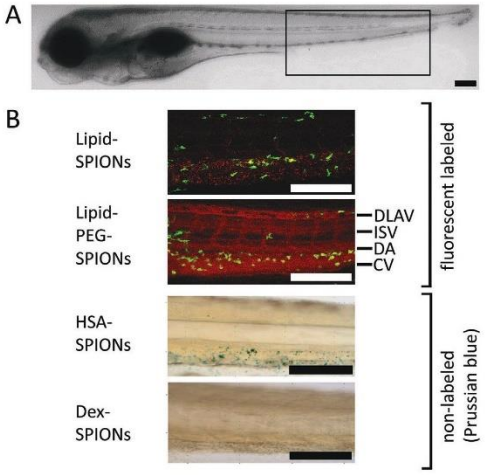

Figure 3. Microscopy based analysis of SPIONs injected into zebrafish embryos. A) Phase-contrast image of a 72 hpf zebrafish embryo. B) Tail section used for visual inspection of particle distribution is highlighted. (top) Confocal microscopy analysis of 72 hpf zebrafish embryos injected with DiI labeled, phospholipid embedded SPIONs (red signal). Macrophages expressing mpeg:kaede are visible in green. (bottom) bright-field images of 72 hpf zebrafish embryos injected with HSA-SPIONs or Dex-SPIONs co-injected with Prussian blue. Embryos were analyzed 24 h post injection. DA: dorsal aorta, CV: cardinal vein, ISV: intersegmental vessel, DLAV: dorsal longitudinal anastomotic vessel. Scale bars correspond to 100 µm.

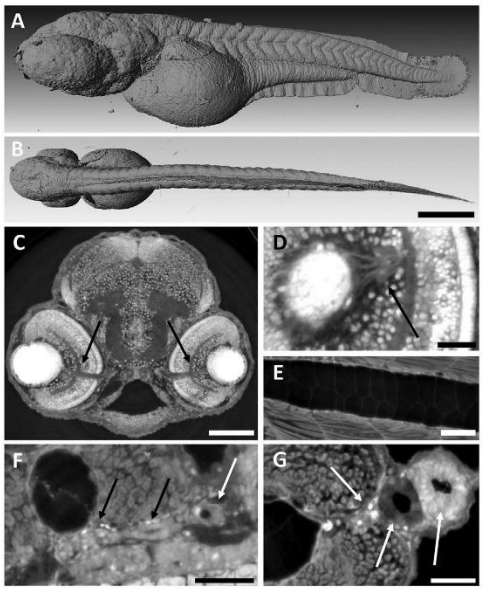

Figure 4. 3D surface rendering and virtual histology of the zebrafish embryo from SRµCT. 3D surface rendering in A) lateral direction and B) dorsal-ventral direction of a 48 hpf zebrafish embryo. C) Virtual tissue sections showing the brain and the eyes of the embryo (transverse plane through the head). The optic nerves are labeled with black arrows. D) Magnification of the eye showing the retina and optical nerve fenestrations (transverse plane, black arrow). E) Notochord with surrounding muscle fibers (midsagittal plane through the tail). F) Pronephron with glomerulus (sagittal plane, dorsal location next to the yolk sac, white arrow) and tubules (black arrows). G) Gut (transverse plane through the tail cranial to the cloaca, right arrow), kidney tubule (middle arrow), and the caudal vein (left arrow). Scale bars correspond to 200 µm (A,B); 70 µm (C,E); 20 µm (D,F,G). Additional high-resolution images are provided on a dedicated internet page (http://zebrafish.pharma-te.ch).

GmbH, Wunstorf, Germany) and Skyscan 1275 (Bruker, Kontich, Belgium) revealed several anatomical features in zebrafish embryos (Figure S1, Supporting Information). The nanotom m measurement showed the outer shape of the embryos (Figure S1A, Supporting Information) and the position of the otoliths (Figure S1B, Supporting Information), but other anatomical features could not be identified because of the detector's energy selectivity, that is, photons below 30 keV are suppressed by the aluminum film in front of the detector. The otoliths have a length of 15–30 µm and consist of crystalline calcium carbonate, that is, aragonite with a density of 2.83 g cm^{-3}[26] and are very well resolved in µCT.[27] The Skyscan 1275 system allows detecting photons with energies as low as 10 keV. Therefore, many additional details including eye, eye lens, spine and yolk were identified with a spatial resolution of about 8 µm.

In order to increase the spatial and density resolution with respect to advanced laboratory-based µCT, SRµCT was explored. Combined absorption- and phase-contrast revealed a wealth of anatomical structures of dehydrated and ethanol-fixed zebrafish embryos 48 hpf. An effective voxel size of 330 nm was selected and three vertically stacked tomograms were acquired to completely visualize the zebrafish embryo with a size of $3.0 \times 1.0 \times 0.5$ mm^3, resulting in 1.4×10^7 voxels. The spatial resolution was around 2 µm, as measured in the reconstructed slices.[28,29]

3D surface renderings reveal honeycomb-like structures on the yolk and eye surface, muscles were in the tail region behind the yolk of the zebrafish embryo, and fins laterally at the yolk (**Figure 4**A,B). Virtual slices at arbitrary position and angle through the 3D volume allow for inspection of the anatomy on the micrometer scale. For example, the structure of the eye including the retina and the visual nerve, the brain, the gastrointestinal (GI) tract and the kidneys are revealed with high detail (Figure 4C–G).

Additional stacks of 100 slices in cranial-caudal, ventral-dorsal, and lateral directions are provided for one 48 hpf zebrafish embryo on a dedicated internet site (http://zebrafish.pharma-te.ch). In the head region of these projections, the four otoliths of each zebrafish are clearly visible due to their high density and X-ray attenuation. They may serve as reference points of an imaginary coordinate system.

To visualize tissue distribution of SPIONs, SRµCT imaging was performed 24 h post injection of coated SPIONs (**Figure 5**). To exploit phase contrast, single-distance phase retrieval was performed prior to tomographic reconstruction.[30] Maximum intensity projections of the resulting 3D datasets allow for

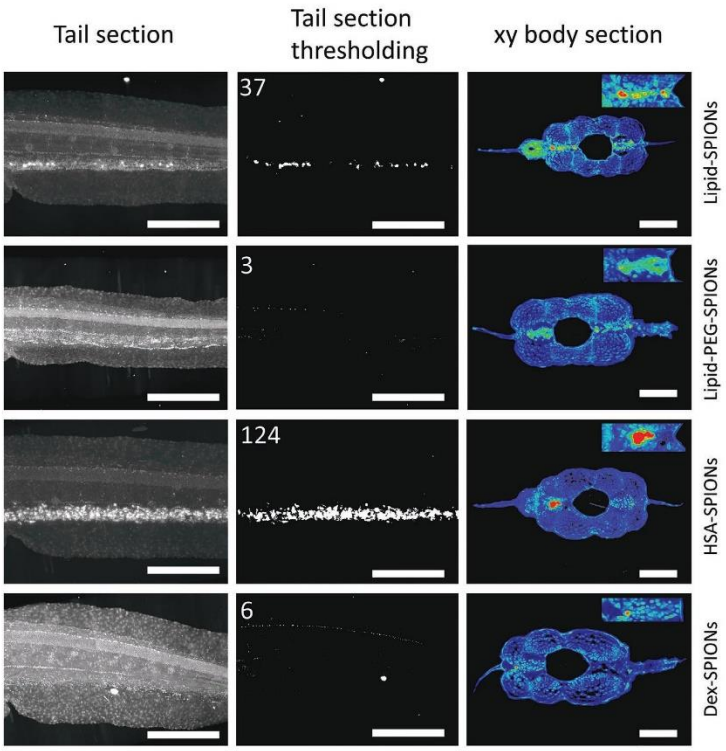

Figure 5. Localization of SPIONs by SRμCT in the tail section of 72 hpf zebrafish embryos. Maximum intensity projections of the tail section behind the cloaca of the zebrafish embryos 24 h post injection of SPIONs. Left column: maximum intensity projections onto the lateral plane. Center column: visualization of SPION agglomerates based on threshold value segmentation of intensity projections shown in the left column. Numbers refer to the number of identified particle agglomerates. Right column: tail sections through the cranial-caudal (*x*–*y*) plane. Visualization by false coloring of high-density agglomerates representing SPIONs. Color gradient from blue (low density) to red (high density). Insert: magnification of the caudal vein. Left and central column scale bars correspond to 300 μm; right column scale bars correspond to 50 μm.

differentiating SPIONs, eye lenses, otoliths, and soft tissue. The injected SPIONs could be localized based on just the higher density of their iron core, confirming that precise localization of non-labeled SPIONs is possible. A single threshold was applied to all four maximum intensity projections to segment the SPION agglomerates. SPIONs were distributed throughout the vascular system and accumulated in the vicinity of the caudal vein as well as the dorsal artery (Figure 5). Particles coated with PEG of MW 5000 (Lipid-PEG-SPIONs) or dextran (Dex-SPIONs) showed no agglomeration whereas particles without steric stabilization (Lipid-SPIONs) or HSA-SPIONs showed extensive agglomeration and deposition within the caudal vein in the tail region. A high-contrast colormap applied to the transverse plane through the tail further confirms these findings. It should be noted, that SPION derived high-density signals can be combined with high-resolution SRμCT tissue representations, see **Figure 6**, which provides a comparable spatial resolution and, but enhanced anatomical details, as compared to light or confocal microscopy, see Figure 3. The nanoparticles are well separated from other strongly X-ray-absorbing features such as the otoliths. Therefore, the authors selected the region

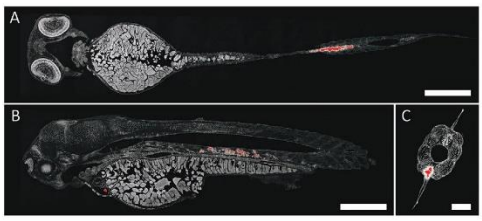

Figure 6. Localization of SPIONs by SRμCT. High resolution SRμCT sections of zebrafish embryos 24 h post injection of SPIONs (density-based red signal). A) coronal plane, B) sagittal plane, and C) transverse plane. Scale bars correspond to 200 μm (A and B), 50 μm (C).

of interest with the nanoparticles and an appropriate threshold to determine the total volume of the aggregated nanoparticles, which corresponds to 220 pL. The nanoparticles volume injected amounts to 2.8 pL. There is a considerable ratio between the nanoparticles volume identified and the one injected, namely about 80. The reasons behind are i) partial volume phenomena and ii) the smear-out by the application of the Paganin algorithm. Furthermore, the authors are convinced that the nanoparticles form loosely packed agglomerates making them to an efficient contrast agent in X-ray imaging.

3. Discussion

SPIONs used in the present study were characterized according to established principles.[10,31,32] They had a similar size, a negative ζ-potential, a high colloidal stability, and a monodisperse size distribution. SPIONs were not cytotoxic and well tolerated in vivo. Neither the MTT assay nor the Alamar blue assay showed statistically significant differences with respect to THP-1 viability as compared to untreated controls confirming previous results with HSA-SPIONs[23] and Dex-SPIONs.[24] Maximal concentrations in these assays were 96 µg mL^{-1} (96 ppm) to avoid catalytic or optical interference of tested particles. It is reasonable to assume that particle concentrations reached in blood in vivo are comparable to these concentrations. The total blood volume of the zebrafish is ≈80 nL. The injected volumes with a particle concentrations 4.8 mg mL^{-1} were 3 nL. Thus, the ratio 14.4 ng/80 nL corresponds to about 180 ppm. Upon injection the particles rapidly started to extravasate and distribute within the organism. Since the volume of the fish is substantially larger than the blood volume, we can reasonably expect nanoparticle concentrations within the studied nanotoxicological range.

Bright-field and fluorescence microscopy[33–35] were used to analyze SPIONs. Both light microscopy methods confirm findings from the SRµCT experiments in that HSA-SPIONs and non-pegylated SPIONs (in contrast to pegylated SPIONs or Dex-SPIONs) had a short half-life in the circulation and did accumulate late in the caudal vein. The light microscopy methods used confirm the findings from the SRµCT experiments. Contrary to the pegylated SPIONs or Dex-SPIONs, the HSA-SPIONs and non-pegylated SPIONs had a short half-life in circulation and did accumulate mainly in the caudal vein and heart 24 h *post injection*. Prussian blue co-injection provided information on particle integrity since reaction of Prussian blue with iron ions leads to the formation of a blue colored complex.[36] However, samples could be visualized in 2D only by bright field microscopy. Confocal laser scanning microscopy allows for 3D scanning of samples and offers a better sensitivity. Furthermore, different fluorescent labels can be combined to co-localize particles with cellular or anatomical structures. In particular, co-localization of non-pegylated SPIONs with macrophages provides information on the cellular fate of these particles. Live imaging of fish embryos is possible. Still, the requirement of labeling SPIONs for this method is a drawback. We therefore decided to combine these methods with X-ray micro-computed tomography (µCT).

Preliminary experiments based on a laboratory µCT instrument were ultimately unable to reveal the zebrafish embryo micro-anatomy and SPION distribution (Figure S1, Supporting Information). Although spatial resolution was approximately equal to that of the SRµCT (2 µm), density resolution was not satisfactory for the simultaneous visualization of soft tissues and SPIONs. The improved density resolution of SRµCT can be attributed to three factors. First, significantly higher X-ray flux, with 200 000 counts s^{-1} for the SRµCT compared to 260 counts s^{-1} for µCT, allowed for both a faster acquisition time and improved photon statistics. Second, the lower photon energy for SRµCT, which was 10.25 keV compared to the 40 kV acceleration voltage (≈30 keV mean energy) of the laboratory µCT meant that the photon efficiency was greater for the SRµCT.[37] This is not an inherent limitation of laboratory µCT, rather the particular instrument employed in this study has a medical X-ray detector with an aluminum coating that absorbs lower energy photons. Third, the high temporal and spatial coherence of the X-ray beam provided by the synchrotron source allow for access to the phase information. Single-distance phase retrieval was applied and provided improved contrast-to-noise ratio, though at the expense of some spatial resolution. It should be noted that a major advantage of laboratory sources is the accessibility. Furthermore, developments in advanced laboratory systems allow for excellent flux and sufficient coherence for high quality phase contrast imaging of biological specimens. This will offer interesting possibilities in the near future.[38,39]

In view of the limitations imposed by laboratory µCT, we decided to use SRµCT as an alternative method to localize non-labeled SPIONs within the vasculature of the zebrafish embryo based on the inherent electron density differences between the nanoparticles and biological tissues. Indeed, it was possible to visualize SPIONs and anatomical structures at a cellular resolution with unprecedented detail. With respect to the established murine and rat models,[40–42] the zebrafish embryos are an attractive alternative for pharmacokinetics and pharmacology studies of nanoparticles due to their small size, the possibility to perform screening experiments in a vertebrate, reduced costs, and ethical aspects. Pegylated SPIONs (Lipid-PEG-SPIONs) and Dex-SPIONs did not form agglomerates or tissue deposits, indicating a long half-life in the circulation. These results were in line with uptake experiments in phagocytic THP-1 cells, where pegylated SPIONs showed minimal cellular uptake. In contrast, agglomerates of particles without steric stabilization or HSA-SPIONs were deposited in the caudal vein or the tail region of the zebrafish embryo suggesting a rapid uptake by tissue resident macrophages.[43] It should be noted that the high X-ray intensity led to formation of gas bubbles and motion artefacts in the medium surrounding the specimen if aqueous buffers were used. We therefore had to replace the medium by ethanol. Consequently, imaging of living specimens was impossible, at least for the spatial and density resolution achieved in this study. No structural change of the fixed zebrafish embryo was observed over the course of the tomographic acquisition. The radiation dose of ≈160 kGy, however, is too high for in vivo studies. In comparison with alternative methods including MR microscopy, SRµCT provides at least one order of magnitude better spatial resolution in each of the three orthogonal directions.[44] Thus, the information gain in tomographic imaging is at least 1000.

The contrast mechanism in SRµCT differs from optical microscopy. In the photon energy range used, the photo effect

yields X-ray attenuation, which linearly depends on the density and from the atomic number by a power law. The SPION exhibits strong X-ray absorption and, thus become visible at low concentrations. The main advantage of SRμCT with respect to conventional and advanced optical methods is the isotropic spatial resolution in the three orthogonal directions. Therefore, 3D pharmacokinetics and pharmacology studies based on absorption, distribution, metabolism, and excretion (ADME) should become more reliable especially for larger organisms.

Because the contrast mechanisms of the optical and X-ray-based techniques have dedicated origin, a combination of the methods can be beneficial, although the lateral spatial resolution is almost equal.[44] A bivariant histogram of data from a selected individuum may lead to information inaccessible by a single method.[45]

The wavelength of hard X-ray tomography is below one nanometer, which implies that the diffraction limit is three orders of magnitude smaller than for optical methods. Therefore, the use of X-ray optics has pushed the spatial resolution of synchrotron radiation-based computed tomography to values well below 100 nm.[46]

It should be mentioned that SRμCT has further advantages with respect to laboratory-based systems. First, the photon energy can be selected in an optimized fashion, for example by applying the Grodzins' criterion.[37] Second, one can acquire data above and below an absorption edge to derive the 3D distribution of the selected element. Concentrations as low as 10 ppm have been detected for osmium.[47] In order to determine the iron distribution within the zebrafish embryo, tomography data just above and below the K-edge (7.1 keV) have to be recorded. At the TOMCAT beamline photon energies below 8 keV are inaccessible. Other imaging beamlines such as P05 at PETRA III, Hamburg, Germany[48] are suited for such a task. Hence, one can reasonably expect future high-resolution tomography studies using synchrotron radiation.

4. Conclusion

Label-free, non-destructive monitoring of low-dose metal-based nanoparticles in an entire vertebrate embryo at submicron voxel sizes was achieved using SRμCT. Analysis based on single-distance phase-contrast provides insight into micro-anatomical structures of zebrafish embryos at a defined developmental stage. For example, structures such as the retina, the optical nerve or the renal tubular system could be examined in their natural state without staining and slicing the specimen. It is tempting to speculate that application of SRμCT for medical diagnostics might offer similar insights. In such a scenario, fast visualization of anatomical structures within small samples of native soft tissue such as, for example, needle biopsies could become a clinical routine.

5. Experimental Section

Synthesis of Superparamagnetic Iron Oxide Nanoparticles Coated with Human Serum Albumin (HSA-SPIONs): Superparamagnetic iron oxide nanoparticles (SPIONs) coated with human serum albumin ($SEON^{LA17HSA2}$) and dextran ($SEON^{Dex\text{-}36q}$) were synthesized as described previously.[23,24] In the present publication, they were designated as HSA-SPIONs and Dex-SPIONs.

Synthesis of Iron Oxide Nanoparticles (SPIONs): SPIONs were synthesized as described previously.[22] In brief, iron(II) chloride ($FeCl_2$) and iron(III) chloride ($FeCl_3$) aqueous solutions (0.024 M $FeCl_2$, 0.037 M $FeCl_3$ in 20 mL milliQ water) were combined at a molar ratio of 3:2 and filtered through a 0.22 μm polycarbonate membrane to remove undissolved agglomerates. By adding concentrated ammonia (30% aqueous solution) at room temperature, co-precipitation took place with an immediate black precipitate formation. The precipitate was washed three times with diluted ammonia (1.5% aqueous solution). Oleic acid (1 g) was added and the solution was heated for 5–10 min to 90 °C. With the help of a magnet, the particles were transferred to trichloromethane. These lipophilic particles were stable for at least 6 months at 4 °C.

Microfluidics Based Preparation of Lipid Coated SPIONs: Lipid-SPIONs and Lipid-PEG-SPIONs, respectively, were prepared using a microfluidics benchtop instrument (NanoAssemblr, Precision Nanosystems, Vancouver, Canada). SPIONs (5 mg) in trichloromethane were dried by evaporation of the solvent and dissolved again in the same volume of a mixture of 60:40 (v/v) of ethanol:tetrahydrofurane containing 1.3 μM cholesterol and 1.63 μM POPC (Avanti Polar Lipids, Alabaster, AL, USA). Where indicated, part of POPC was replaced by an equal molar amount of indocarbocyanine fluorescent dye (0.03 μM) and/or DSPE modified with PEG of molecular weight 5000 (0.33 μM) (Avanti Polar Lipids). As the admixed hydrophilic phase, phosphate buffered saline (10 mM phosphate, 150 mM NaCl, pH of 7.4) was used. The flow rate ratio organic phase:aqueous phase was 2:1 and the flow rate was 10 mL min^{-1}. Liposome-coated SPIONs were dialyzed against PBS overnight using a Spectra/Por2 dialysis membrane with a MW cut-off of 12–14 kDa (Spectrum Europe BV., DG Breda, The Netherlands) to remove organic solvents. After dialysis, samples were purified by size exclusion chromatography (NAP-10 Sephadex G25 column (Sigma Aldrich, St. Louis, MO, USA) to remove uncoated iron oxide nanoparticles/free iron from the solution. Concentrations of SPIONs were determined based on their optical density (OD) in trichloromethane at 520 nm using stock solutions of uncoated SPIONS in trichloromethane (see above) as a reference.

Physico-Chemical Characterization of Nanoparticles: Analysis of particle size, hydrodynamic diameter, polydispersity index, and ζ potential of lipid-(PEG-)SPIONs were performed as described.[49] The used methods were dynamic and electrophoretic light scattering (Delsa Nano C, Beckman Coulter Inc., Nyon, Switzerland) and transmission electron microscopy (CM-100, Philips, Amsterdam, Netherlands).

Cellular Uptake of SPIONs by THP-1 Phagocytic Cells: THP-1 monocytic cells (acute monocytic leukemia, human, ATCC, TIB-202) were cultured in Roswell Park Memorial Institute 1640 (RPMI 1640) cell medium (supplemented with 10% foetal calf serum, penicillin (100 units mL^{-1})/streptomycin (100 μg mL^{-1}), 10 mM HEPES buffer, 1% sodium pyruvate, and 0.05 mM ß-mercaptoethanol). The cell medium was renewed every 3 days. For uptake studies, THP-1 cells were seeded at a density of 5×10^4 cells per well onto poly-d-lysine-coated 8-Well μ-Slides (Ibidi, Martinsried, Germany). Differentiation to macrophages was induced by addition of 200 nM phorbol 12-myristate 13-acetate (PMA) for 72 h. For uptake studies, cells were incubated with fluorescent labeled SPIONs (48 μg mL^{-1} iron oxide concentration) in cell culture medium. Cells were washed with PBS buffer, cell nuclei were counterstained using Hoechst 33342 (2.5 μg mL^{-1}) for 10 min and cell membranes were counterstained using CellMask Deep Red Plasma membrane stain (0.5 μL mL^{-1}) for 5 min (both Thermo Fisher Scientific Inc., Waltham, MA, USA). Cells were washed with cell culture medium and analyzed by confocal laser scanning microscopy (see below).

Quantitative analysis of cellular uptake was performed by flow cytometry (FACS) using a BD FACSCanto II RUO Special Order System (BD Biosciences, Allschwil, BL, Switzerland). Cells were incubated with fluorescent labeled lipid-(PEG-)SPIONs as described above, washed with PBS, and collected by trypsinization (5 min at 37 °C). After centrifugation in Eppendorf tubes, the pellets were resuspended in PBS and measured in the flow cytometer (10 000 counts, FL-6 laser).

Cytotoxicity: To determine cell viability, MTT,[50] and Alamar blue[51] assays were used in combination with THP-1 and Hep G2 cells.[50] For the Alamar blue assay, fluorescence was measured with an excitation at 560 nm and an emission at 580 nm (Spectramax M2 plate reader, Molecular Devices, Sunnyvale, CA) 4 h after addition of a 10% of Alamar blue solution. Cytotoxicity was expressed as the percentage of viable cells, where untreated cells were defined to be 100% viable. Each time point had its own 100% viability control. Since high concentrations of SPIONs were known to interfere with the MTT or Alamar blue assays, control experiments were carried out to exclude catalytic or optical interference of SPIONs (up to 96 μg mL^{-1}) in incubations of up to 48 h.

Zebrafish Barge Culture: Experiments were conducted using zebrafish embryos (Danio rerio) from the wildtype strain AB/Tübingen (AB/Tu) and transgenic strain mpeg:kaede (Tg(mpeg1:Gal4-VP16/UAS:Kaede)) with fluorescent macrophages.[52] Adult zebrafish were kept in 20 L aerated tanks at a temperature of 28 °C and a 10/14 h light/dark cycle. Mating was carried out in breeding baskets. Eggs were collected the next morning, cleaned, sorted, and transferred into petri dishes containing 25 mL of embryo-medium E2 as described previously.[43] A maximum of 100 eggs were transferred into one petri dish and stored in an incubator (Aqualytic, Dortmund, Germany) at 28 °C. E2 medium was renewed daily after egg sorting. 24 h post fertilization (hpf) the embryos were bleached with 200 μM 1-phenyl 2-thiourea (PTU) to inhibit melanization. Zebrafish embryos were dechorionated 48 hpf.

Bright-Field or Phase-Contrast Microscopy: The zebrafish embryos were fixed in 4% PFA for 30 min and dehydrated with increasing ethanol dilutions series from 25, 50, 75, and >96 vol% for 15 min each and stored in analytical ethanol (>96 vol%). Each embryo was embedded using Euparal embedding medium (Carl Roth, Karlsruhe, Germany) on microscope slides and dried for 3 days. For analyzing and imaging, a Leica DM6000 microscope (Leica Microsystems, Heerbrugg, Switzerland) was used.

Confocal Laser Scanning Microscopy: 48 hpf zebrafish embryos were sedated, immobilized and injected with lipoSPIONs as described below and were placed on glass bottom petri dishes for imaging. Confocal scanning microscopy was done with a ZEISS LSM 880 inverted microscope (Carl Zeiss, Oberkochen, Germany). Z-stacks were recorded at a step size of 100 μm using a 40 × objective (N.A. 1.1). Excitation wavelength was 488 nm (mpeg:kaede), and 561 nm (DiI) in combination with bright-field microscopy. The emission wavelength covered ranges from 500 to 535 nm and 575 to 636 nm, respectively. Image stacks were processed using the open source Fiji software (ImageJ, Version 1.52p, Wayne Rasband, Research Services Branch, National Institute of Mental Health, Bethesda, Maryland, USA).[53]

Zebrafish Injection and Fixation: For the experiments, the embryos were anaesthetized with 25 mL of tricaine methanesulfonate (612 μM) in E2 fish media. They were immobilized in 0.3% agarose containing tricaine methanesulfonate (612 μM) and placed on glass bottom petri dishes (MatTek, Ashland, MA, USA), each laying on the left side. Microinjections of NP were conducted as described previously.[43] Injected nanoparticle volumes were 3 nL for all types of SPIONs (4.8 mg mL^{-1}).

For micro-tomography experiments, embryos (1 and 24 h post injection (hpi) of SPIONs) were euthanized with tricaine methanesulfonate containing 0.612 mM trisaminomethane. Subsequently, embryos were fixed at room temperature for 1 hin 4.0% paraformaldehyde. Fixed specimens were dehydrated using ethanol at increasing concentrations (25%, 50%, 70%, and ≥99.8%) for 15 min each under gentle agitation and stored at 4 °C.

Sample Preparation for X-Ray Tomography: Embryos fixed in ethanol were placed within sample holders consisting of plastic pipette tips filled with ethanol. Using ethanol as a solvent (in contrast to an aqueous buffer or UV sensitive polymers[54]) avoided formation of gas bubbles during X-ray irradiation.

SRμCT: Single-distance phase-contrast SRμCT was used for 3D visualization of nanoparticles injected into zebrafish embryos. Experiments were performed at the Swiss Light Source (Villigen, Switzerland) TOMCAT X02DA beamline. Here, a superbending magnet source combined with a Si(111) double crystal monochromator produced a monochromatic beam with a photon energy of 10.25 keV ($\Delta E/E \approx 10^{-4}$). For single-distance phase retrieval, the sample-detector distance was 12 mm. The source size was ≈140 μm × 45 μm (h × v), corresponding to a projected source size of 64 nm × 21 nm. Thus, the spatial resolution was limited by other factors such as detector pixel size and scintillator thickness. This setup provides significantly higher transverse and longitudinal coherence compared to laboratory X-ray sources. Projections were recorded using a LuAG:Ce scintillator coupled to a pco.EDGE 5.5 camera (2560 × 2160 pixel array and 16 bit depth) with the UPLAPO10x (effective pixel size 0.65 μm) and UPLAPO20x (effective pixel size 0.325 μm) objectives. In order to visualize the entire specimen, three to five height steps per specimen were acquired depending on the post fertilization stage. An exposure time of 240 ms was selected (around 50 000 counts per flat field) for 1801 projections recorded around 180° resulting in total scan times of around 7 min.

Reconstruction of Micro-Tomograms: Phase retrieval for the SRμCT projections was performed with the single distance non-iterative method introduced by Paganin and co-workers[30] as implemented in AnkaPhase (Version 2.1).[55] Reconstruction was performed in TomoPy with ASTRA Toolbox 1.8, an open-source Python package for tomographic data processing and image reconstruction.[56,57] A δ/β value of 10^3 was used to obtain optimized contrast and to reduce edge enhancement for the monitoring of the SPIONs. It should be noted that data were acquired far from the criterion presented by Grodzins for optimized absorption contrast, which was a well-known rule-of-thumb although it was only strictly valid for single phase materials and the central point. Additionally, with photon energy of 10.25 keV and pixel size of 325 nm, the propagation distance of 12 mm was outside of the contact plane for a pure absorption measurement.

Analysis of the Reconstructed Data: Spatial resolution was estimated on reconstructed slices with the method proposed by Mizutani and co-workers as well as the method proposed by Modregger and co-workers.[28,29] 3D surface renderings and maximum intensity projections were generated using the 3D visualization and analysis software Avizo (Version 9.5, FEI Visualization Sciences Group, Hillsboro, OR, USA). Specific regions of interest (e.g. whole zebrafish embryo, otoliths, nanoparticle agglomerates) were segmented by thresholding. Virtual histological sections were created by analyzing the ortho slices in each direction of the 3D volume. Free access to this data set in the form of collections of high resolution images is provided on a dedicated internet page (http://zebrafish.pharma-te.ch).

Statistical Analysis: Results were expressed as means of independent sets of experiments ± standard deviation (SD), $n \geq 3$. Wherever indicated, significance was determined by one-way analysis of variance (ANOVA). Tukey's post-hoc test was performed to compare the difference between treated groups and corresponding controls. Differences were considered to be significant at $p \leq 0.05$. Used software was Origin 9.1 (OriginLab, Northampton, MA, USA).

Supporting Information

Supporting Information is available from the Wiley Online Library or from the author.

Acknowledgements

This work was supported by grants from the Swiss Center for Applied Human Toxicology (SCAHT), the NanoReg2 program (European Union Horizon 2020 research agreement 646221, 15.0200-3), the Manfred Roth Foundation, Fürth, Germany and the Forschungsstiftung Medizin, University Hospital Erlangen, Germany. The authors thank Prof. Markus Affolter, Dr. Heinz Belting, and Dr. Susanne Schenk for support with zebrafish barge culturing. The authors acknowledge the Paul Scherrer

Institut, Villigen, Switzerland for provision of synchrotron radiation beamtime at the TOMCAT beamline X02DA of the SLS.

Conflict of Interest

The authors declare no conflict of interest.

Keywords

digital histology, nanoparticle detection, superparamagnetic iron oxide nanoparticles, synchrotron radiation-based micro computed tomography, zebrafish embryos

Received: March 11, 2020
Revised: May 26, 2020
Published online:

[1] R. Tietze, H. Rahn, S. Lyer, E. Schreiber, J. Mann, S. Odenbach, C. Alexiou, *Histochem. Cell Biol.* **2011**, *135*, 153.
[2] A. Wicki, D. Witzigmann, V. Balasubramanian, J. Huwyler, *J. Controlled Release* **2015**, *200*, 138.
[3] D. D. Jurašin, M. Ćurlin, I. Capjak, T. Crnković, M. Lovrić, M. Babič, D. Horák, I. V. Vrček, S. Gajović, *Beilstein J. Nanotechnol.* **2016**, *7*, 246.
[4] M. Bietenbeck, A. Florian, C. Faber, U. Sechtem, A. Yilmaz, *Int J Nanomed.* **2016**, *11*, 3191.
[5] R. Tietze, J. Zaloga, H. Unterweger, S. Lyer, R. P. Friedrich, C. Janko, M. Pöttler, S. Dürr, C. Alexiou, *Biochem. Biophys. Res. Commun.* **2015**, *468*, 463.
[6] L. Yildirimer, N. T. K. Thanh, M. Loizidou, A. M. Seifalian, *Nano Today* **2011**, *6*, 585.
[7] M. E. Samberg, S. J. Oldenburg, N. A. Monteiro-Riviere, *Environ. Health Perspect.* **2010**, *118*, 407.
[8] Y.-S. Chen, Y.-C. Hung, I. Liau, G. S. Huang, *Nanoscale Res. Lett.* **2009**, *4*, 858.
[9] C. C. Hanot, Y. S. Choi, T. B. Anani, D. Soundarrajan, A. E. David, *Int. J. Mol. Sci.* **2016**, *17*, 54.
[10] S. Siegrist, E. Cörek, P. Detampel, J. Sandström, P. Wick, J. Huwyler, *Nanotoxicology* **2018**, *13*, 73.
[11] G. D. Rubin, *Radiology* **2014**, *273*, S45.
[12] M. Shilo, T. Reuveni, M. Motiei, R. Popovtzer, *Nanomedicine.* **2012**, *7*, 257.
[13] J. R. Ashton, J. L. West, C. T. Badea, *Front. Pharmacol.* **2015**, *6*, 256.
[14] D. P. Clark, C. T. Badea, *Phys. Med.* **2014**, *30*, 619.
[15] D. P. Cormode, P. C. Naha, Z. A. Fayad, *Contrast Media Mol. Imaging* **2014**, *9*, 37.
[16] R. Meir, R. Popovtzer, *Wiley Interdiscip. Rev. Nanomed. Nanobiotechnol.* **2018**, *10*, 28544497.
[17] L. Y. Rizzo, S. K. Golombek, M. E. Mertens, Y. Pan, D. Laaf, J. Broda, J. Jayapaul, D. Möckel, V. Subr, W. E. Hennink, G. Storm, U. Simon, W. Jahnen-Dechent, F. Kiessling, T. Lammers, *J. Mater. Chem. B* **2013**, *1*, 3918.
[18] C. Chakraborty, A. R. Sharma, G. Sharma, S.-S. Lee, *J. Nanobiotechnol.* **2016**, *14*, 65.
[19] B. Novoa, A. Figueras, in *Curr. Top. Innate Immun. II* (Eds.: J. D. Lambris, G. Hajishengallis), Springer, New York, NY **2012**, pp. 253–275.
[20] S. Sieber, P. Grossen, J. Bussmann, F. Campbell, A. Kros, D. Witzigmann, J. Huwyler, *Adv. Drug Delivery Rev.* **2019**, *151–152*, 152.
[21] M. Dalstra, P. M. Cattaneo, F. Beckmann, *J. Craniofacial Genet. Dev. Biol.* **2006**, *9*, 199.
[22] M. D. Cuyper, M. Joniau, *Eur. Biophys. J.* **1988**, *15*, 311.
[23] J. Zaloga, M. Pöttler, G. Leitinger, R. P. Friedrich, G. Almer, S. Lyer, E. Baum, R. Tietze, R. Heimke-Brinck, H. Mangge, F. Dörje, G. Lee, C. Alexiou, *Eur. J. Pharm. Biopharm.* **2016**, *101*, 152.
[24] H. Unterweger, C. Janko, M. Schwarz, L. Dézsi, R. Urbanics, J. Matuszak, E. Őrfi, T. Fülöp, T. Bäuerle, J. Szebeni, C. Journé, A. R. Boccaccini, C. Alexiou, S. Lyer, I. Cicha, *Int. J. Nanomed.* **2017**, *12*, 5223.
[25] M. Sedighi, S. Sieber, F. Rahimi, M.-A. Shahbazi, A. H. Rezayan, J. Huwyler, D. Witzigmann, *Drug Delivery Transl. Res.* **2019**, *9*, 404.
[26] C. Haddon, J. Lewis, *J. Comp. Neurol.* **1996**, *365*, 113.
[27] B. Müller, R. Bernhardt, T. Weitkamp, F. Beckmann, R. Bräuer, U. Schurigt, A. Schrott-Fischer, R. Glueckert, M. Ney, T. Beleites, C. Jolly, D. Scharnweber, *Int. J. Mater. Res.* **2007**, *98*, 613.
[28] R. Mizutani, R. Saiga, S. Takekoshi, C. Inomoto, N. Nakamura, M. Itokawa, M. Arai, K. Oshima, A. Takeuchi, K. Uesugi, Y. Terada, Y. Suzuki, *J. Microsc.* **2016**, *261*, 57.
[29] P. Modregger, D. Lübbert, P. Schäfer, R. Köhler, *Phys. Status Solidi A* **2007**, *204*, 2746.
[30] D. Paganin, S. C. Mayo, T. E. Gureyev, P. R. Miller, S. W. Wilkins, *J Microsc.* **2002**, *206*, 33.
[31] S. S. Khiabani, M. Farshbaf, A. Akbarzadeh, S. Davaran, *Artif. Cells, Nanomed., Biotechnol.* **2017**, *45*, 6.
[32] E. J. Cho, H. Holback, K. C. Liu, S. A. Abouelmagd, J. Park, Y. Yeo, *Mol. Pharmaceutics* **2013**, *10*, 2093.
[33] D. E. Igartúa, P. L. Azcona, C. S. Martinez, S. delV. Alonso, V. L. Lassalle, M. J. Prieto, *Toxicol. Appl. Pharmacol.* **2018**, *358*, 23.
[34] M. Giannaccini, M. Giannini, M. P. Calatayud, G. F. Goya, A. Cuschieri, L. Dente, V. Raffa, *Int. J. Mol. Sci.* **2014**, *15*, 1590.
[35] L. C. Felix, V. A. Ortega, J. D. Ede, G. G. Goss, *Environ. Sci. Technol.* **2013**, *47*, 6589.
[36] G. Fu, S. T. Sanjay, X. Li, *Analyst* **2016**, *141*, 3883.
[37] L. Grodzins, *Nucl. Instrum. Methods Phys. Res.* **1983**, *206*, 541.
[38] T. Tuohimaa, M. Otendal, H. M. Hertz, *Appl. Phys. Lett.* **2007**, *91*, 074104.
[39] M. Bartels, V. H. Hernandez, M. Krenkel, T. Moser, T. Salditt, *Appl. Phys. Lett.* **2013**, *103*, 083703.
[40] J. Hu, S. Ni, Y. Cao, X. Wang, S. Liao, H. Lu, *SPINE* **2017**, *42*, E883.
[41] M. Saccomano, J. Albers, G. Tromba, M. D. Radmilović, S. Gajović, F. Alves, C. Dullin, *J. Synchrotron Radiat.* **2018**, *25*, 1153.
[42] Y. C. Liyuan Jiang, Y. C. Liyuan Jiang, *Aging Dis.* **2020**, *11*, 1.
[43] S. Sieber, P. Grossen, P. Uhl, P. Detampel, W. Mier, D. Witzigmann, J. Huwyler, *Nanomedicine* **2019**, *17*, 82.
[44] G. Schulz, C. Waschkies, F. Pfeiffer, I. Zanette, T. Weitkamp, C. David, B. Müller, *Sci. Rep.* **2012**, *2*, 826.
[45] A. K. Stalder, B. Ilgenstein, N. Chicherova, H. Deyhle, F. Beckmann, B. Müller, S. E. Hieber, *Int. J. Mater. Res.* **2014**, *105*, 679.
[46] A. Khimchenko, C. Bikis, A. Pacureanu, S. E. Hieber, P. Thalmann, H. Deyhle, G. Schweighauser, J. Hench, S. Frank, M. Müller-Gerbl, G. Schulz, P. Cloetens, B. Müller, *Adv. Sci.* **2018**, *5*, 1700694.
[47] B. Müller, A. Lareida, F. Beckmann, G. M. Diakov, F. Kral, F. Schwarm, R. Stoffner, A. R. Gunkel, R. Glueckert, A. Schrott-Fischer, J. Fischer, A. Andronache, W. Freysinger, in *Developments in X-Ray Tomography V* (Ed:. U. Bonse), SPIE, Bellingham, WA **2006**, p. 631805.
[48] F. Wilde, M. Ogurreck, I. Greving, J. U. Hammel, F. Beckmann, A. Hipp, L. Lottermoser, I. Khokhriakov, P. Lytaev, T. Dose, H. Burmester, M. Müller, A. Schreyer, *AIP Conf. Proc.* **2016**, *1741*, 030035.
[49] S. Siegrist, H. Kettiger, E. Fasler-Kan, J. Huwyler, *Toxicol. In Vitro* **2017**, *42*, 308.
[50] H. Kettiger, D. Sen Karaman, L. Schiesser, J. M. Rosenholm, J. Huwyler, *Toxicol. In Vitro* **2015**, *30*, 355.
[51] R. Hamid, Y. Rotshteyn, L. Rabadi, R. Parikh, P. Bullock, *Toxicol. In Vitro* **2004**, *18*, 703.
[52] F. Ellett, L. Pase, J. W. Hayman, A. Andrianopoulos, G. J. Lieschke, *Blood* **2011**, *117*, e49.

[53] J. Schindelin, I. Arganda-Carreras, E. Frise, V. Kaynig, M. Longair, T. Pietzsch, S. Preibisch, C. Rueden, S. Saalfeld, B. Schmid, J.-Y. Tinevez, D. J. White, V. Hartenstein, K. Eliceiri, P. Tomancak, A. Cardona, *Nat. Methods* **2012**, *9*, 676.
[54] J. Wang, A. Goyanes, S. Gaisford, A. W. Basit, *Int. J. Pharm.* **2016**, *503*, 207.
[55] T. Weitkamp, D. Haas, D. Wegrzynek, A. Rack, *J. Synchrotron Radiat.* **2013**, *20*, 205.
[56] D. Gürsoy, F. De Carlo, X. Xiao, C. Jacobsen, *J. Synchrotron Radiat.* **2014**, *21*, 1188.
[57] D. M. Pelt, D. Gürsoy, W. J. Palenstijn, J. Sijbers, F. De Carlo, K. J. Batenburg, *J. Synchrotron Radiat.* **2016**, *23*, 842.

NANO MICRO small

Supporting Information

for *Small,* DOI: 10.1002/smll.202000746

Shedding Light on Metal-Based Nanoparticles in Zebrafish by Computed Tomography with Micrometer Resolution

*Emre Cörek, Griffin Rodgers, Stefan Siegrist, Tomaz Einfalt, Pascal Detampel, Christian M. Schlepütz, Sandro Sieber, Pascal Fluder, Georg Schulz, Harald Unterweger, Christoph Alexiou, Bert Müller, Maxim Puchkov, and Jörg Huwyler**

1. Supporting Information

Shedding Light on Metal-Based Nanoparticles in Zebrafish by Computed Tomography with Micrometer Resolution

Emre Cörek[1], Griffin Rodgers[3], Stefan Siegrist[1], Tomaz Einfalt[1], Pascal Detampel[1], Christian M. Schlepütz[2], Sandro Sieber[1], Pascal Fluder[1], Georg Schulz[3], Harald Unterweger[4], Christoph Alexiou[4], Bert Müller[3], Maxim Puchkov[1], Jörg Huwyler[1]*

[1]Department of Pharmaceutical Technology, University of Basel, Klingelbergstrasse. 50, 4056 Basel, Switzerland;

[2]Swiss Light Source, Paul Scherrer Institute, Forschungsstrasse 111, 5232 Villigen, Switzerland;

[3]Biomaterials Science Center, Department of Biomedical Engineering, University of Basel, Gewerbestrasse 14, 4123 Allschwil, Switzerland;

[4] Department of Otorhinolaryngology, Head and Neck Surgery, Section for Experimental Oncology and Nanomedicine (SEON), Else Kröner-Fresenius Stiftung Professorship, Waldstraße 1,91054 Erlangen University of Erlangen, Germany

*Correspondence: Prof. Dr. Jörg Huwyler, Pharmaceutical Technology, Pharmacenter, University of Basel, Klingelbergstrasse. 50, 4056 Basel, Switzerland. Tel: +41(0)612071513. E-mail: joerg.huwyler@unibas.ch

Zebrafish viability after injection

To ensure that the used doses do not affect the zebrafish embryo until reaching its larval stage (144 hpf), we monitored viability and malformation occurrence in 48 hpf zebrafish embryos injected with various doses of SPIONs. Embryos were monitored over a period of 96 hours post injection (**Error! Reference source not found.**). To avoid toxic effects, injected doses were limited to 15 ng of SPIONs in the following studies.

Table S 1 – Zebrafish embryo viability post injection. Comparison of the viability of zebrafish embryos treated with iron oxide ENPs (HSA-SPIONs) with untreated controls. n=30 animals were injected 48 hpf in each experiment. Values represent the number of specimens 96 hours after injection of 1, 3, 5, and 8 nL of a 5.6 mg/mL solution. *: significant difference as compared to negative control (analysis of variance (ANOVA) and Tukey's post-hoc test, $p < 0.05$). Values are means ± S.D., n=3.

Dose [ng]	Viable embryos	Visible malformations
0	29.3 ± 0.2	0
5.6	27.3 ± 2.1	0
17	28.7 ± 0.6	0
28	28.3 ± 1.2	0
45	25.3 ± 1.5 *	4

Absorption-contrast micro-computed tomography (µCT)

Laboratory-based absorption contrast measurements were performed using a Phoenix nanotom® m (Universal Systems, Wunstorf, Germany) equipped with a 180.0 kV / 15.0 W nanofocus X-ray source. The experiments were performed using an acceleration voltage of 60.0 kV and a beam current of 240.0 µA. Taking advantage of the cone beam geometry, a pixel length of 1.0 µm was

selected. 1440 equiangular projections over 360° were acquired. After reconstruction, the 3D data sets were visualized using VG Studio Max 2.1 software (Volume Graphics, Heidelberg, Germany). ENPs in zebrafish embryos could not be visualized due to limited density resolution.

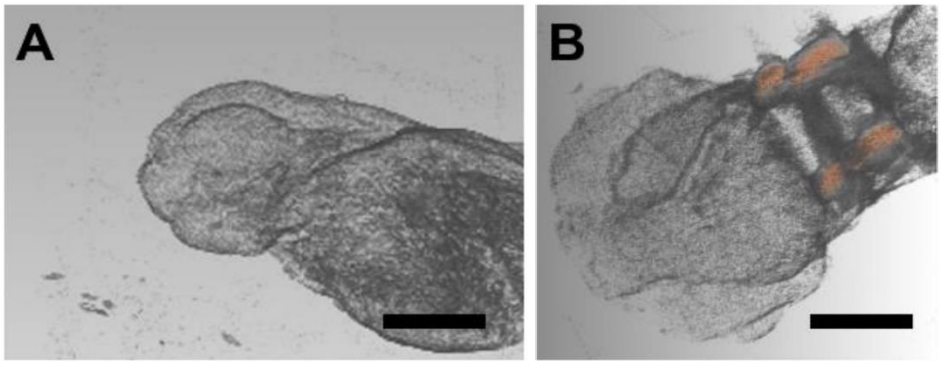

Figure S 1 – µCT analysis of zebrafish embryos (48 hpf). Visualization of a zebrafish embryo using an x-ray tube equipped nanotom®m instrument. (A) Lateral view of the head section. Scale bar: 100 µm. (B) Dorsal view of the head section. Otoliths are marked in red. Scale bar: 50 µm.

III. MAGNETIC FIELD INDUCED PHAGOCYTOSIS OF IRON OXIDE NANOPARTICLES IN ZEBRAFISH EMBRYO (DANIO RERIO)

Emre Cörek, Tomaz Einfalt, Jan Stephan Bolten, Jörg Huwyler

Journal: will be submitted a journal as a short communication paper

Magnetic field induced phagocytosis of iron oxide nanoparticles in zebrafish embryo (*Danio rerio*)

*Emre Cörek[1], Tomaz Einfalt[1], Jan Stephan Bolten[1], Jörg Huwyler[1]**

[1]Department of Pharmaceutical Technology, University of Basel, Klingelbergstrasse. 50, 4056 Basel, Switzerland;

[*]Correspondence: Prof. Jörg Huwyler, Pharmaceutical Technology, Pharmacenter, University of Basel, Klingelbergstrasse. 50, 4056 Basel, Switzerland. Tel: +41(0)612071513. E-mail: joerg.huwyler@unibas.ch

Keywords:

superparamagnetic iron oxide nanoparticles (SPIONs), zebrafish embryos, phagocytosis, magnetic uptake, targeting

Abstract

Introduction: Superparamagnetic iron oxide nanoparticles (SPIONs) are used for targeting and imaging. Depending on their physicochemical properties they show different biodistribution profiles. Controlling them *in vivo* by magnetic manipulation remains a challenge and can be done by different methods.

Methods: In this study, phospholipid-coated SPIONs were prepared using microfluidics and injected into zebrafish embryos as a vertebrate model organism. *In vivo* phagocytosis and accumulation of SPIONs were studied under manipulation by magnetic forces.

Results: We show that phagocytosis and accumulation of different SPIONs can be influenced by magnetic forces. Magnets were used to enhance phagocytosis and control the accumulation of SPIONs injected into living zebrafish embryos significantly without harming the model organism.

Conclusion: It was proved, that magnetic forces can be used to enhance phagocytosis of SPIONs *in vivo* in a living vertebrate model organism significantly and that agglomerates can be trapped in the blood flow by a magnet.

1. Introduction

The use of nanoparticulate materials has become mainstream in both academic and industrial settings. One of the nanoparticle types which are frequently applied are metal nanoparticles.[1,2] Consisting of a metal or metal oxide core (e.g. gold or iron oxide), their characteristic size range is between 1-100 nm. To prevent the particles from agglomeration, to decrease their polydispersity index (PDI) and their applicability, the particles can be coated with different materials such as phospholipids modified with polyethyleneglycol (PEG).[3] A prominent representative of metal nanoparticles are superparamagnetic iron oxide nanoparticles (SPIONs) which are used as imaging or targeting agents with a variety of different surface modifications.[4,5] While surface modifications and small size allow SPIONs to present favorable circulation profiles, their dense electromagnetic core allows them to be non-invasively controlled *in vivo* by an external magnetic field.[6,7] Magnetic manipulation can be used to induce hyperthermia, agglomerations or for targeting of specific anatomical structures.[8]

The aim of the present study was to synthesize and coat SPIONs using a microfluidic manufacturing in order to achieve different blood circulation profiles and to analyze their behaviour in a magnetic field in a living vertebrate model organism. It was important to elucidate, whether the injected phospholipid-PEG-SPIONs alter their characteristics when induced to magnetic forces and how this might alter their interactions on cellular level compared to the control group which was not induced to magnetic forces.

2. Results and discussion

2.1 Synthesis of SPIONs

The iron oxide core of the SPIONs was synthesized by co-precipitation in an one-pot synthesis with a narrow particle distribution and an oleic acid coating to make them lipophilic as described previously by Cörek et al. Subsequently, the surface was modified with a benchtop instrument in a microfluidics mixing chamber (NanoAssemblr, Precision Nanosystems, Vancouver, Canada). Particles were embedded within an enhanced lipid shell containing a phospholipid bilayer (POPC) with additional phospholipids modified with PEG (DSPE-PEG) of molecular weight (MW) 5000.[9] All particles were fluorescently labelled with DiI stain (1 %) to make them visible by fluorescent microscopy (Figure 1).

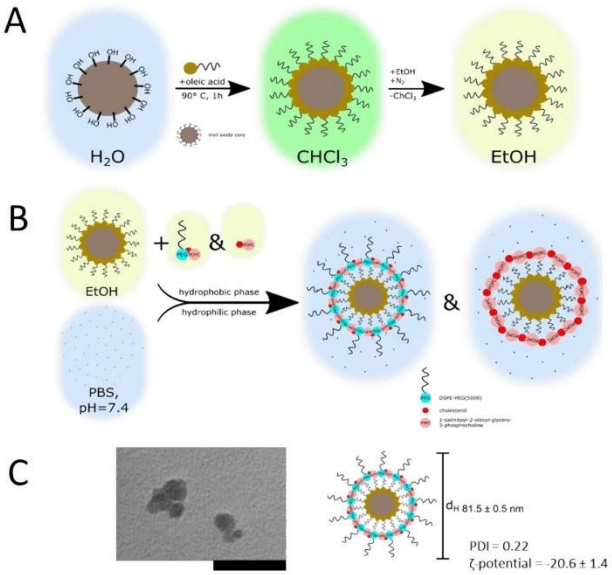

Figure 1: Synthesis and characterization of SPIONs. Scheme shows the one-pot-synthesis of lipophilic SPIONs coated with oleic acid (A), and the mechanism of coating the lipophilic SPIONs with

phospholipids (B). SPIONs coated with phospholipids containing PEG of MW 5000 (Lipid-PEG-SPIONs) (C) with the corresponding schematic representation of the nanoparticle. Hydrodynamic diameter (d_H) in C was determined using phosphate-buffered saline as a diluent. Polydispersity index (PDI) and zeta -potential (ζ-potential, mV) are mentioned. All measurements were done in triplicate. Scale bars correspond to 50 nm.

2.2 Physico-chemical characterization of SPIONs

The physico-chemical characterization of manufactured SPIONs **(Table 1)** was based on dynamic light scattering, electrophoretic light scattering (ζ-potential determination), and transmission electron microscopy.

Long circulating phospholipid-SPIONs with pegylation of MW 5000 used in the present study had a hydrodynamic diameter below 100 nm and a monodisperse size distribution (PDI ≈ 0.2, Table 1). The particles were anionic with a ζ-potential of at least -20 mV.

Size and morphology of coated SPIONs was visualized by transmission electron microscopy **(Figure 1)**.

2.3 Cellular uptake and cytotoxicity

After intravenous injection, uncoated SPIONs are recognized by the reticuloendothelial system (RES) quickly.[10,11] This reduces their half-life in blood circulation strongly and therefore it is advantageous to prevent this kind of reactions.[12] For this purpose, SPIONS have previously been reported to get coated with half-life prolonging modifications such as PEG or dextran.[13] As an outcome, tissue resident macrophages cannot remove those modified nanoparticles from the circulation and cellular interactions

are reduced drastically.[14] In our previous experiments we showed that phospholipid SPIONs coated with PEG of MW of 5000 circulate much longer *in vivo* and that they are not cytotoxic to the model organism.

2.4 Fluorescence microscopy-based visualization of magnet induced SPION phagocytosis in zebrafish embryos

In vivo experiments were done using zebrafish embryos as a vertebrate screening model. Minute amounts of SPIONs (3 nl of a 4.8 mg/ml solution corresponding to a dose of less than 15 ng) were intravenously injected into the Duct of Cuvier of 48 hours post fertilization (hpf) zebrafish embryos. Circulation and biodistribution of fluorescent nanoparticles was visualized by confocal microscopy 24 and 48 hours post injection (hpi) **(Figure 2)**. Lipid-PEG-SPIONs were fluorescently labeled using the fluorescent, lipophilic indocarbocyanine stain DiI (Figure 2, red signal). Co-localization of nanoparticles was done by using a transgenic zebrafish line (mpeg:kaede) expressing a green fluorescent protein within macrophages (Figure 2, green signal). *In vivo* phagocytosis was detectable 24 and 48 hpi all over the embryo (Figure 2, yellow signal). In combination with a magnet, all particles had a short half-life in the blood circulation and were rapidly taken up by macrophages in high amounts which is shown by colocalization analysis with the Pearson's correlation factor R (Figure 2). Control group without a magnet (Figure 2 A) and with a weak magnet (Figure 2 D) have a correlation below R= 0.3. Group with a magnet after 24 hpi (R= 0.51) and after 48 hpi (R= 0.9) show significant increase in phagocytosis induced by the magnetic forces.

The SPIONs were characterized after standardized protocols and methods.[15–17] Phagocytosis of SPIONs was analyzed by confocal laser scanning microscopy (CLSM).

The analysis by CLSM showed, that the zebrafish embryos injected with lipid-PEG-SPIONs in the magnetic field (Figure 2 B, C) showed significantly increased phagocytic uptake compared to the control embryos without a magnetic field (Figure 2 A). The difference in uptake could be seen after 24 hpi (Figure 2 B) and even increased after 48 hpi (Figure 2 C). With a weaker magnet, it was not possible to see the same effect (Figure 2 D). This is also proved by the colocalization data (Figure 2, R-values).

With that, it was possible to enhance the phagocytic uptake of SPIONs in macrophages *in vivo* by help of a magnet significantly because of possible slowing down of the nanoparticles in the blood stream so that they could easier and faster get phagocyted. This effect was shown with similar experiments beforehand by injecting bigger fluorescent labeled SPIONs (size approx. around 1 µm) and watching them under a fluorescent stereo microscope. As soon as the magnet was placed in the near of the embryo, the particles completely stopped flowing around in the blood stream.

Combinations of SPIONs and phagocytosis were already used *in vitro* for example in a study in which they showed a magnet-based phenotypic screening strategy[18], and for separating granulocytes and monocytes by phagocytosis of bacterial magnetite[19].

It was also shown, that the viability of macrophages is not changed by phagocytosis of SPIONs.[20,21]

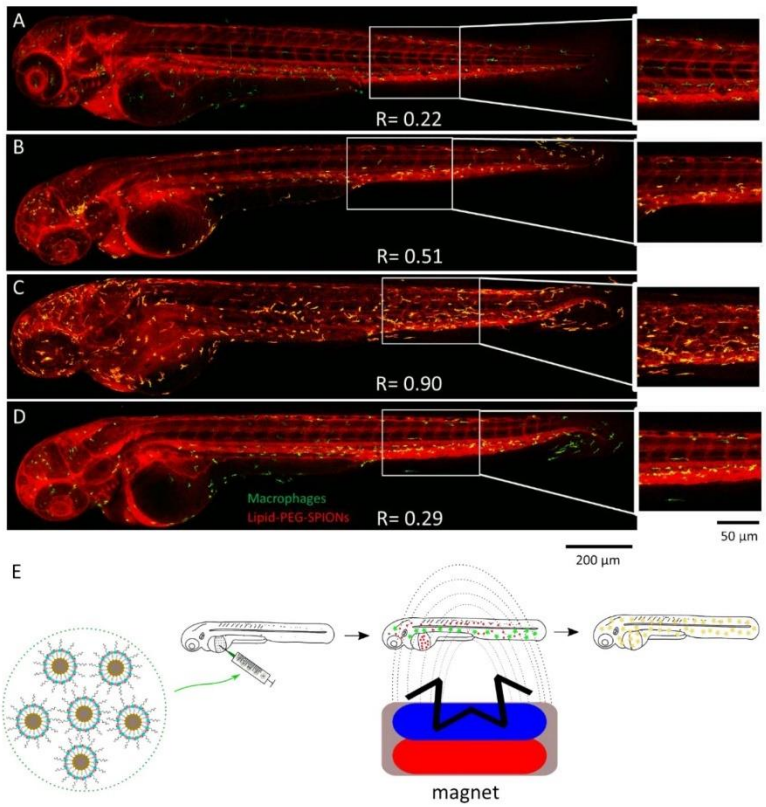

Figure 2 – Cellular uptake of fluorescent labeled SPIONs by phagocytic THP-1 cells. Uptake of (A) Lipid-PEG-SPIONs without a magnet, 24 hpi; (B) Lipid-PEG-SPIONs with a strong magnet, 24 hpi; and Lipid-PEG-SPIONs with a strong magnet, 48 hpi by phagocytic THP-1 cells; and (D) Lipid-PEG-SPIONs with a weak magnet, 24 hpi. Injection followed by confocal microscopy reveals *in vivo* location of SPIONs (red signal: DiI labeled SPIONs, green signal: mpeg:kaede expressing phagocytic THP-1 cells, yellow-signal: SPIONs taken up by THP-1 cells). Tail section used for visual inspection of particle distribution is highlighted. Embryos were analyzed 24 (A, B, D) and 48 (C) hours post injection. Bottom line represents the experiment scheme. The nanoparticles are injected into the Duct of Cuvier of the zebrafish embryo (left scheme) and then get induced to a magnetic field with the red dots representing

the nanoparticles and the green stars representing the macrophages (middle scheme). After 24 and 48 hpi, the particles get phagocyted by the macrophages and they appear to be yellow (right scheme). Colocalization between macrophages (green) and SPIONs (red) was done and is shown by the Pearson's correlation factor R on each image (R= 1.0 means maximal co-localization of green and red channels). Scale bars correspond to 200 µm (overview) and 50 µm (zoom-box). Images are one example of n=3 each.

In recent years, macrophage targeting is getting more and more important in drug delivery for a lot of different diseases. Novel methods even aim to target hepatic macrophages to treat hepatic diseases[22] or in cardiovascular diseases to use macrophages as a therapeutic target for healing after for example a myocardial infarct[23]. This could be achieved by inducing a local magnetic field on the dedicated organ, in this case the liver or heart, to maximize loading efficiency of macrophages by phagocytosis of SPIONs which can be modified which specific compounds for drug therapy which can be even used in cancer for tumor-associated macrophages (TAM) or inflammation.[24,25]

As a consequence, this method can be used to rapidly target and maximize the loading of macrophages with metal-based nanoparticles *in vivo*. Variety of modified nanoparticles are possible to make targeted drug delivery, e.g. toxic agents in the coating of the nanoparticles to kill the macrophages or to enhance uptake only by physical forces without using biological surface modification of the SPIONs and for a variety of different diseases.[26,27]

3. Conclusion

An easy and fast targeting of macrophages was done in this work in order to maximize the macrophage uptake in vivo. Together with the easy modifiable phospholipid-PEG-SPIONs, this method reveals new

insights of macrophage targeting and analysis in a small vertebrate model and probably also in higher vertebrates such as mice or rats.

4. Experimental Section

Synthesis of iron oxide nanoparticles (SPIONs)

SPIONs were synthesized as described previously.[28] Iron(II) chloride ($FeCl_2$) and iron(III) chloride ($FeCl_3$) aqueous solutions (0.024 M $FeCl_2$, 0.037 M $FeCl_3$ in 20 ml milliQ water) were mixed in a molar ratio of 3:2 and the mixture was filtered through a 0.22 µm polycarbonate membrane. At room temperature concentrated ammonia (30% aqueous solution) started the co-precipitation resulted in a black precipitate. After washing three times with diluted ammonia (1.5% aqueous solution), oleic acid (1 g) was added. The solution was heated for 5-10 minutes to 90 °C and after cooling down, the particles were transferred to trichloromethane with a magnet.

Microfluidics based preparation of coated SPIONs

Lipid-PEG-SPIONs were prepared using a microfluidics benchtop instrument (NanoAssemblr, Precision Nanosystems, Vancouver, Canada). By evaporation, SPIONs (5 mg) in trichloromethane were dried and dissolved in a mixture of 60:40 (v/v, ethanol:tetrahydrofurane) of the same volume. This mixture contained 1.3 µM cholesterol and 1.63 µM POPC (Avanti Polar Lipids, Alabaster, AL, USA). A part of the POPC was replaced by indocarbocyanine fluorescent dye (DiI) (0.03 µM). DSPE modified with PEG of molecular weight 5000 (0.33 µM) (Avanti Polar Lipids) was added. Phosphate buffered saline (10 mM phosphate, 150 mM NaCl, pH of 7.4) was used as the hydrophilic phase. The flow rate ratio was 2:1 (organic phase:aqueous phase), and the flow rate 10 mL/min. The resulting coated SPIONs were dialyzed overnight against PBS with a Spectra/Por2 dialysis membrane (MW cut-off of 12-14 kDa, Spectrum

Europe BV., DG Breda, The Netherlands). Purification was done by size exclusion chromatography (NAP-10 Sephadex G25 column (Sigma Aldrich, St. Louis, MO, USA). SPION concentration was measured at 520 nm by optical density (OD) in trichloromethane. Stock solutions of uncoated SPIONS in trichloromethane (see above) were used as a reference.

Physicochemical characterization of nanoparticles

By dynamic and electrophoretic light scattering (Delsa Nano C, Beckman Coulter Inc., Nyon, Switzerland), and transmission electron microscopy (CM-100, Philips, Amsterdam, Netherlands), particle size, hydrodynamic diameter, polydispersity index, and ζ potential of lipid-PEG-SPIONs were measured.[29]

Zebrafish barge culture

Zebrafish embryos (Danio rerio) from the transgenic strain mpeg:kaede (Tg(mpeg1:Gal4-VP16/UAS:Kaede)) with fluorescent macrophages were used.[30] Adult zebrafish were kept in aerated tanks of 20 L at 28 °C and 10/14 hour light/dark cycle. Mating was done in breeding baskets and the next morning eggs were collected, cleaned, sorted and transferred into petri dishes with 25 ml of embryo-medium E2.[31] One petri dish contained maximal 100 eggs and they were stored in an incubator (Aqualytic, Dortmund, Germany) at 28 °C. Eggs were sorted and E2 medium was renewed daily. Bleaching took place 24 hours post fertilization (hpf) with 200 µM 1-phenyl 2-thiourea (PTU) to inhibit embryo melanization. Dechorionation was done 48 hpf.

Confocal laser scanning microscopy

Zebrafish embryos were sedated and immobilized in 0.3 % agarose containing tricaine methanesulfonate (612 µM) and injected with lipid-PEG- or Dragon-Green-SPIONs. After injection, they were immediately placed on a neodymium magnet of 150 kg strength and size of 70 x 70 x 30 mm or 1 kg strength and size of 6 x 2 x 2 mm (Webcraft AG, Uster, Switzerland). ZEISS LSM 880 inverted

microscope (Carl Zeiss, Oberkochen, Germany) was used for imaging. Step size of z-stacks were 10 µm using a 40× objective (N.A. 1.1). Excitation wavelength was 488 nm (mpeg:kaede), and 561 nm (DiI) in combination with bright-field microscopy. The emission wavelength range was 500 to 535 nm and 575 to 636 nm respectively. Image stacks were processed with Fiji software (ImageJ, Version 1.52p, Wayne Rasband, Research Services Branch, National Institute of Mental Health, Bethesda, Maryland, USA).[32]

Colocalization of SPIONs and macrophages

Z-stacks were analyzed for colocalization using the open source Fiji software (ImageJ, Version 1.52p, Wayne Rasband, Research Services Branch, National Institute of Mental Health, Bethesda, Maryland, USA).[32] The colocalization was done with "coloc2" using the default values. The Pearson's correlation coefficient was given as the result to show the amount of co-localization between the red (SPIONs) and green (Macrophages) channels. The higher R, the more co-localization is given with R=1.0 as the maximum value.

5. Acknowledgement

This work was supported by grants from the Swiss Center for Applied Human Toxicology (SCAHT), the NanoReg2 program (European Union Horizon 2020 research agreement 646221, 15.0200-3. We thank Prof. Markus Affolter, Dr. Heinz Belting and Dr. Susanne Schenk for support with zebrafish barge culturing.

6. Declaration of Interest

The authors have no conflicts of interest to declare.

7. References

[1] R. Tietze, H. Rahn, S. Lyer, E. Schreiber, J. Mann, S. Odenbach, C. Alexiou, *Histochem Cell Biol* **2011**, *135*, 153.

[2] A. Wicki, D. Witzigmann, V. Balasubramanian, J. Huwyler, *Journal of Controlled Release* **2015**, *200*, 138.

[3] D. D. Jurašin, M. Ćurlin, I. Capjak, T. Crnković, M. Lovrić, M. Babič, D. Horák, I. V. Vrček, S. Gajović, *Beilstein Journal of Nanotechnology* **2016**, *7*, 246.

[4] M. Bietenbeck, A. Florian, C. Faber, U. Sechtem, A. Yilmaz, "Remote magnetic targeting of iron oxide nanoparticles for cardiovascular diagnosis and therapeutic drug delivery: where are we now?," DOI 10.2147/IJN.S110542can be found under https://www.dovepress.com/remote-magnetic-targeting-of-iron-oxide-nanoparticles-for-cardiovascul-peer-reviewed-article-IJN, **2016**.

[5] D. Bobo, K. J. Robinson, J. Islam, K. J. Thurecht, S. R. Corrie, *Pharmaceutical Research* **2016**, *33*, 2373.

[6] S. F. Hasany, N. H. Abdurahman, A. R. Sunarti, R. Jose, "Magnetic Iron Oxide Nanoparticles: Chemical Synthesis and Applications Review," can be found under https://www.ingentaconnect.com/content/ben/cnano/2013/00000009/00000005/art00002, **2013**.

[7] T. Vangijzegem, D. Stanicki, S. Laurent, *Expert Opinion on Drug Delivery* **2019**, *16*, 69.

[8] R. Tietze, J. Zaloga, H. Unterweger, S. Lyer, R. P. Friedrich, C. Janko, M. Pöttler, S. Dürr, C. Alexiou, *Biochemical and Biophysical Research Communications* **2015**, *468*, 463.

[9] M. Sedighi, S. Sieber, F. Rahimi, M.-A. Shahbazi, A. H. Rezayan, J. Huwyler, D. Witzigmann, *Drug Deliv. and Transl. Res.* **2019**, *9*, 404.

[10] A.-K. Steuer, M. Klinger, R. Pries, K. Lüdtke-Buzug, *Current Directions in Biomedical Engineering* **2018**, *4*, 271.

[11] C. F. Borgognoni, J. H. Kim, V. Zucolotto, H. Fuchs, K. Riehemann, *Artificial Cells, Nanomedicine, and Biotechnology* **2018**, *46*, 694.

[12] Y. C. Park, J. B. Smith, T. Pham, R. D. Whitaker, C. A. Sucato, J. A. Hamilton, E. Bartolak-Suki, J. Y. Wong, *Colloids Surf B Biointerfaces* **2014**, *119*, 106.

[13] Wahajuddin, S. Arora, *Int J Nanomedicine* **2012**, *7*, 3445.

[14] A. Orlando, M. Colombo, D. Prosperi, M. Gregori, A. Panariti, I. Rivolta, M. Masserini, E. Cazzaniga, *J Nanopart Res* **2015**, *17*, 351.

[15] S. Siegrist, E. Cörek, P. Detampel, J. Sandström, P. Wick, J. Huwyler, *Nanotoxicology* **2018**, *0*, 1.

[16] S. S. Khiabani, M. Farshbaf, A. Akbarzadeh, S. Davaran, *Artificial Cells, Nanomedicine, and Biotechnology* **2017**, *45*, 6.

[17] E. J. Cho, H. Holback, K. C. Liu, S. A. Abouelmagd, J. Park, Y. Yeo, *Mol Pharm* **2013**, *10*, DOI 10.1021/mp300697h.

[18] M. S. Haney, C. J. Bohlen, D. W. Morgens, J. A. Ousey, A. A. Barkal, C. K. Tsui, B. K. Ego, R. Levin, R. A. Kamber, H. Collins, A. Tucker, A. Li, D. Vorselen, L. Labitigan, E. Crane, E. Boyle, L. Jiang, J. Chan, E. Rincón, W. J. Greenleaf, B. Li, M. P. Snyder, I. L. Weissman, J. A. Theriot, S. R. Collins, B. A. Barres, M. C. Bassik, *Nat Genet* **2018**, *50*, 1716.

[19] T. Matsunaga, K. Hashimoto, N. Nakamura, K. Nakamura, S. Hashimoto, *Appl Microbiol Biotechnol* **1989**, *31*, 401.

[20] T.-C. Tseng, F.-Y. Hsieh, S. Hsu, *Biomater. Sci.* **2016**, *4*, 670.

[21] A. Laskar, M. Ghosh, S. I. Khattak, W. Li, X.-M. Yuan, *Nanomedicine* **2012**, *7*, 705.

[22] F. Tacke, *J. Hepatol.* **2017**, *66*, 1300.

[23] T. Ben-Mordechai, D. Palevski, Y. Glucksam-Galnoy, I. Elron-Gross, R. Margalit, J. Leor, *J. Cardiovasc. Pharmacol. Ther.* **2015**, *20*, 36.

[24] L. Cassetta, J. W. Pollard, *Nat Rev Drug Discov* **2018**, *17*, 887.

[25] G. Hu, M. Guo, J. Xu, F. Wu, J. Fan, Q. Huang, G. Yang, Z. Lv, X. Wang, Y. Jin, *Front Immunol* **2019**, *10*, DOI 10.3389/fimmu.2019.01998.

[26] W. He, N. Kapate, C. W. Shields, S. Mitragotri, *Advanced Drug Delivery Reviews* **2019**, DOI 10.1016/j.addr.2019.12.001.

[27] J. M. Brown, L. Recht, S. Strober, *Clin Cancer Res* **2017**, *23*, 3241.

[28] M. D. Cuyper, M. Joniau, *Eur Biophys J* **1988**, *15*, 311.

[29] S. Siegrist, H. Kettiger, E. Fasler-Kan, J. Huwyler, *Toxicology in Vitro* **2017**, *42*, 308.

[30] F. Ellett, L. Pase, J. W. Hayman, A. Andrianopoulos, G. J. Lieschke, *Blood* **2011**, *117*, e49.

[31] S. Sieber, P. Grossen, P. Uhl, P. Detampel, W. Mier, D. Witzigmann, J. Huwyler, *Nanomedicine: Nanotechnology, Biology and Medicine* **2019**, *17*, 82.

[32] J. Schindelin, I. Arganda-Carreras, E. Frise, V. Kaynig, M. Longair, T. Pietzsch, S. Preibisch, C. Rueden, S. Saalfeld, B. Schmid, J.-Y. Tinevez, D. J. White, V. Hartenstein, K. Eliceiri, P. Tomancak, A. Cardona, *Nature Methods* **2012**, *9*, 676.

IV. FURTHER PUBLICATIONS

REMOVING RING ARTEFACTS FROM SYNCHROTRON RADIATION-BASED HARD X-RAY TOMOGRAPHY DATA

Peter Thalmann, Christos Bikis, Georg Schulz, Pierre Paleo, Alessandro Mirone, Alexander Rack, Stefan Siegrist, **Emre Cörek**, Jörg Huwyler, Bert Müller

Journal: SPIE Proceedings Volume 10391, Developments in X-Ray Tomography XI; 1039114 (2017)

DOI: https://doi.org/10.1117/12.2274236

PROCEEDINGS OF SPIE

SPIEDigitalLibrary.org/conference-proceedings-of-spie

Removing ring artefacts from synchrotron radiation-based hard x-ray tomography data

Peter Thalmann
Christos Bikis
Georg Schulz
Pierre Paleo
Alessandro Mirone
Alexander Rack
Stefan Siegrist
Emre Cörek
Jörg Huwyler
Bert Müller

SPIE.

Removing ring artefacts from synchrotron radiation-based hard X-ray tomography data

Peter Thalmann[a], Christos Bikis[a], Georg Schulz[a], Pierre Paleo[b], Alessandro Mirone[b], Alexander Rack[b], Stefan Siegrist[c], Emre Cörek[c], Jörg Huwyler[c], and Bert Müller

[a]Biomaterials Science Center, University of Basel, Allschwil, Switzerland;
[b]European Synchrotron Radiation Facility, Grenoble, France
[c]Department of Pharmaceutical Sciences, University of Basel, Basel, Switzerland

ABSTRACT

In hard X-ray microtomography, ring artefacts regularly originate from improperly functioning pixel elements on the detector or from particles and scratches on the scintillator. We show that due to the high sensitivity of contemporary beamline setups further causes inducing inhomogeneities in the impinging wavefronts have to be considered. We propose in this study a method to correct the thereby induced failure of simple flatfield approaches. The main steps of the pipeline are (i) registration of the reference images with the radiographs (projections), (ii) integration of the flat-field corrected projection over the acquisition angle, (iii) high-pass filtering of the integrated projection, (iv) subtraction of filtered data from the flat-field corrected projections. The performance of the protocol is tested on data sets acquired at the beamline ID19 at ESRF using single distance phase tomography.

Keywords: ring artefacts, tomography, 2D-2D registration, in-line tomography, high-pass filter, phase reconstruction

1. INTRODUCTION

In hard X-ray microtomography, ring artefacts are a common unwanted phenomenon that can severely decrease the obtained image quality. Frequently, they originate from indorrectly functioning pixel elements on the detector unit or from particles and scratches on the scintillator. The high level of sensitivity achieved by nowadays beamline setups does not only allow to be more sensitive to density variations within the specimen, but also turns the imaging setups more susceptible to inhomogeneities introduced on the impinging wavefronts. In detail, inadequacies of the X-ray optical elements like windows, attenuators and distortions of the wavefront by the sample itself can cause a partial failure of simple flatfield correction. Thus far, many ring artefacts removal algorithms are applied on the sinogram[1] or the reconstruction slice[2] itself. A better approach would be however to not only to remove the artefacts themselves, but also to maintain the radiographs true information.

All specimens investigated were composed of low-absorbing tissues, such that typical hard X-ray micro computed tomography in absorption contrast mode does not provide sufficient contrast to adequately resolve the inner structure of the specimen investigated. However, light propagation through a medium can be described by the complex refractive index

$$n(x, y, z) = 1 - \delta(x, y, z) + i\beta(x, y, z), \tag{1}$$

where the imaginary part, β, accounts for the attenuation and the refractive index decrement, δ, accounts for the phase shift of the impinging wave respectively.[3] It is well known, that for materials composed of low-Z elements, as is the case for the specimens investigated, the total phase-shift cross section can be up to three orders of magnitude higher then the total absorption cross section depending on the photon energy,[4,5] making phase tomography the preferential method for the tree-dimensional investigation of such specimens. There are several techniques for the phase retrieval, as for instance grating interferometry,[6,7] in-line single distance and holotomograhy.[8,9]

Further author information: (Send correspondence to Bert Müller)
Bert Müller: E-mail: bert.mueller@unibas.ch, Telephone: 0041 61 207 54 30

Developments in X-Ray Tomography XI, edited by Bert Müller, Ge Wang, Proc. of SPIE Vol. 10391, 1039114 · © 2017 SPIE · CCC code: 0277-786X/17/$18 · doi: 10.1117/12.2274236

The motivation behind developing such a ring-artefact removal approach lies on the fact that single-distance phase retrieval, i.e. our X-ray tomography modality of choice for the three-dimensional investigation of physically soft tissues, including nervous tissue, is more prone to such artefacts than its alternatives (e.g. grating interferometry). Nevertheless, the comparative advantages offered, as will be described in what follows, compensate for this specific shortcoming, which we now prove that can be tackled in an efficient manner.

The reason for single distance in-line, propagation-based tomography being the method of choice lies in the superior spatial resolution provided, simpler instrumentation and very efficient scanning times that are absolutely necessary for biomedical applications requiring several replicates to be scanned for a specific experiment. In in-line propagation-based phase tomography the recorded projections contain both absorption and phase information, where the phase information can be interpreted as the Laplacian of the phase of the wavefront after transversing the sample. In 2002, Paganin et al.[10] derived an algorithm based on the transport of intensity equation (TIE)[11] assuming a single-component specimen and that the object and the detector plane fulfill the near-field condition. and requiring only one single distance. Despite the violation of the single-component assumption, the algorithm has proven itself to be robust also for the case of biological specimens, and soft tissue in particular.[8,9] It also presents the advantage of requiring only one measurement at a single distance.

Here, we thus introduce an improved ring artefact removal algorithm for high-resolution micro computed tomography. The performance of the algorithm is illustrated using synchrotron radiation-based micro computed tomography (SRμCT) in phase contrast mode.

2. MATERIALS AND METHODS

2.1 Specimen preparation

2.1.1 Mouse brain tumor

For the experiment a nude mouse (CD-1-Foxn1nu, Charles River Laboratories, France) was used. A stereoactic frame for head fixation was used for the injection of murine glioma cells (2104 GL261 cells) into the right frontal lobe. *In-vivo* magnetic resonance experiments were performed using a PharmaScan 47/16 MRI system equipped with a 4.7 T magnet with 16 cm bore diameter and a cryogenic quadrature RF surface transmit/receive coil (Bruker BioSpin Ettlingen, Germany). During *in-vivo* experiments, the mouse was placed on a customized support equipped with a stereotactic system for head fixation and a face mask for anaesthetic administration (isofluorane (1.5 % to 2 %). For the administration of contrast agent a cannula was inserted into the right tail vein. All the experiments were approved by local authorities (license ZH 168/2010) and performed in strict adherence to the Swiss law for animal protection. The mouse was euthanized by cervical dislocation at day 15 following tumor inoculation. A specimen containing brain and tumor was explanted using augmented reality assistance[12] and was fixed in buffered formalin immediately after extraction. For the tomography measurements, a dedicated plastic container was used.

2.1.2 Human nerve

A human peripheral nerve was obtained post-mortem from a donated body, with informed consent for scientific use provided beforehand. All procedures were conducted in accordance with the Declaration of Helsinki and approved by the Ethikkommission Nordwestschweiz. Following standard pathology procedure, the peripheral nerve was extracted from the donated body and fixed in 4% histological-grade buffered formalin. It was subsequently dehydrated and finally embedded in a paraffin/plastic polymer mixture. For the tomography measurement, a cylindrical sample with a diameter of 6 mm was extracted from the paraffin block, using a metal punch.

2.1.3 Zebra fish embryo

Experiments were conducted using the zebrafish wild type strain AB/Tbingen (AB/TU). Adult zebrafish were kept in aerated tanks tempered to 28.0 °C at a 10:14 hour light/dark cycle. After collection, eggs were cleaned, sorted and transferred into petri dishes with 0.5 X embryo-medium (E2 medium,[13] 5.0 mM NaCl, 0.25 mM KCl, 0.5 mM $MgSO_4$, 0.15 mM KH_2PO_4, 0.05 mM Na_2HPO_4, 0.5 mM $CaCl_2$, 0.71 mM $NaHCO_3$, 1.0 l water (Millipore 18-textohm), 0.001 % (w/v) methylene blue, pH 7.4). Petri dish containing eggs were stored in an incubator

Table 1. Experimental and reconstruction parameters, where δ/β denotes the assumed ratio of refractive index decrement over the imaginary part of the refractive index for each specimen, d the sample-detector distance, N the total number of projections acquired, and t the exposure time per projection

Specimen	Pixel size [µm]	δ/β	d [mm]	N	t [s]	off-axis	preparation	camera
Brain tumor	1.87	1546	202	2000	0.2	no	formalin	FReLoN 2K
Human nerve	0.66	1500	30	5120	0.1	yes	paraffin	PCO Edge
Zebrafish	0.33	2000	10	5120	0.1	yes	paraffin	PCO Edge

(Aqualytic, Dortmund, Germany) at 28.0 °C. E2 medium was renewed daily. Zebrafish embryos were dechorionated 24 h post fertilization (hpf) by removal of the chorion with acupuncture needles (0.20 mm × 15 mm, Wandrey, Berlin, Germany). The dechorionated embryos were immobilized 48 hpf by adding 1 ml 25 X tricaine stock solution to the medium (400.0 mg tricaine methanesulfonate, 97.9 ml water (Millipore 18-textohm), 2.1 ml trisaminomethane, pH=9). Immobilized zebrafish embryos were fixed in 4.0 % paraformaldehyde and dehydrated in ethanol. Fixed zebrafish embryos were aligned in the channel (diameter 0.8 mm) of a two-pieced custom-made aluminum mold (3.0 cm x 2.0 cm x 2.0 cm). Aligned embryos were air dried for one minute to ensure complete evaporation of excess ethanol. Thereafter, the mold was placed vertically into liquid paraffin wax (80.0°, Sigma-Aldrich, Buchs, Switzerland) allowing the channel containing the zebrafish embryo to fill with paraffin due to capillary forces. After cooling, the newly formed paraffin rod containing the embedded embryo was removed from the socket of the mold with a blunt syringe. The paraffin rods were stored at 4.0 °C until further use.

2.2 Single-distance phase retrieval

All specimens were measured using in-line single distance phase tomography with the experiments being carried out at the ID19 beamline (ESRF, Grenoble, France). Phase retrieval was performed using the algorithm proposed by Paganin *et al.*[10] using ANKAphase.[14] A list of the acquisition and reconstruction parameters is given in Table 1. The phase projections were reconstructed using the standard filtered back-projection algorithm[15] implemented in MATLAB (2016a, The MathWorks, Inc., Natick, Massachusetts USA).

3. RESULTS AND DISCUSSION

Figure 1 shows selected phase reconstruction slices for for the three specimen, before ring artefact correction. The slices contain severe ring artifacts. As already stated, usually, these artefacts arise from improperly working scintillator or pixel elements. In such cases they can be removed by using a stripe removing filter on the

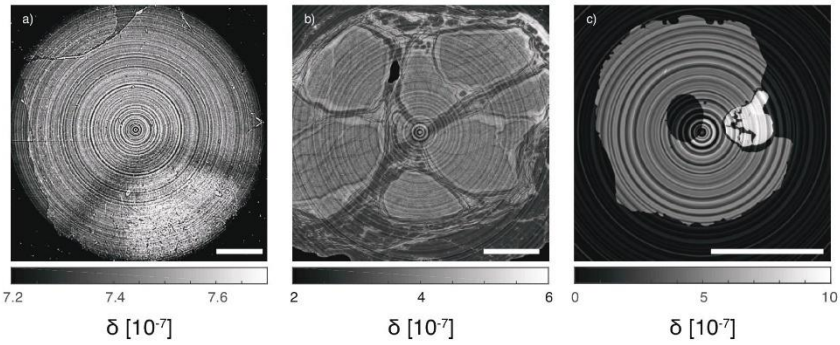

Figure 1. The images show characteristic slices of the phase-reconstructed specimens with standard flat-field correction applied: (a) brain tumor, (b) human nerve and (c) zebra fish embryo. All slices contain more or less strong ring artifacts. Scale bar length is 500 μm.

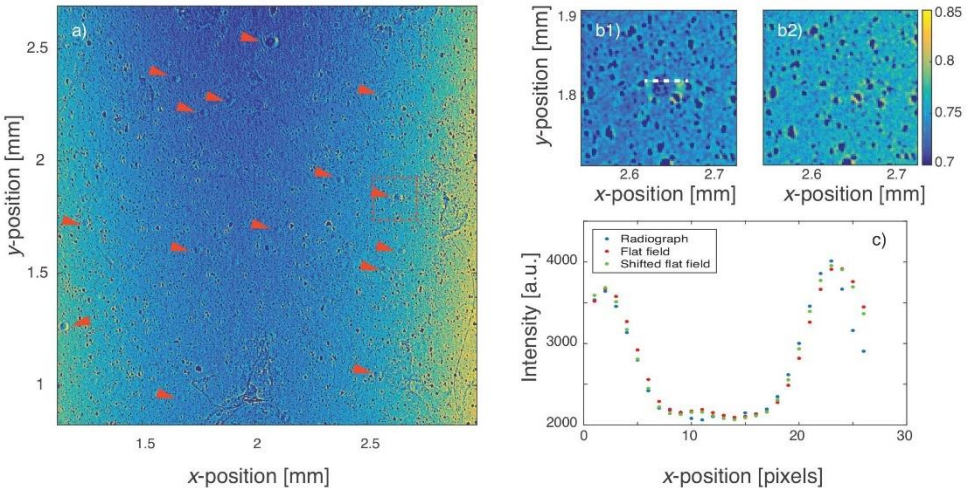

Figure 2. (a) The image shows a selected region of interest (ROI) of a representative projection of the mouse brain tumor specimen. The read arrowheads indicate the prominent donut-like artefacts that persist after standard flat-field correction. A zoom-in of the region inside the dashed box containing such a donut-like structure prior to and after having shifted the flat-field appropriately is given in (b1) and (b2) respectively. (c) A line plot through the donut-like artefact indicated by the red line in figure (b1) clearly shows the sub-pixel mismatch that occurs when simple flat-field correction is used.

sinogram[1] or directly on the reconstruction slice.[2] However, measuring low-absorbing specimens in phase-contrast mode requires high sensitivity, provided by nowadays beamline setups. The high sensitivity achieved makes the system also more prone to disturbances of the impinging wavefronts. Under these circumstances simple flat-field correction is insufficient.

To better elucidate why this happens, consider for example the projection of the mouse brain tumor, given in Figure 2(a). Numerous donut-like artefacts can be observed, that are clearly artificial. Having a closer look on the line plot through such a structure given in 2(b) reveals a sub-pixel mismatch of the flat-field (red) with its projection (blue), as the plots slightly deviate where the curve is falling and rising. Shifting the flat-field to its corresponding projection (green) resulted in almost precise match of the two images as can also be seen in Figure 2(b), while the shift in x-direction was around 0.2 pixels and in the y-direction less than 0.1 pixels.

The effect of using translation registration to correct for the mismatch is also illustrated in Figure 3. While for the mouse brain specimen measured with a pixel size of 1.87 µm translation registration mainly resulted in the removal of several donut-like structures, its effect with decreasing pixel size was much more pronounced. For example, for the zebra fish embryo measurement, a translation over a pixel resulted in the removal of prominent cloud-like structures on the projection and thereby resulted in projection containing many more details. However, for all measurements, image registration alone could not remove all ring artefacts, as can be seen in the sinogram comparison Figure 3 (c) as well as the corresponding reconstructed slices in Figure 4(b).

It should also not be overlooked that image registration can readily increase reconstruction time. For instance, finding the best out of 100 flat-field images for 5120 radiographs would require 512000 registrations, which is an extremely computation-intensive task and can be immensely time-consuming for commercialy available

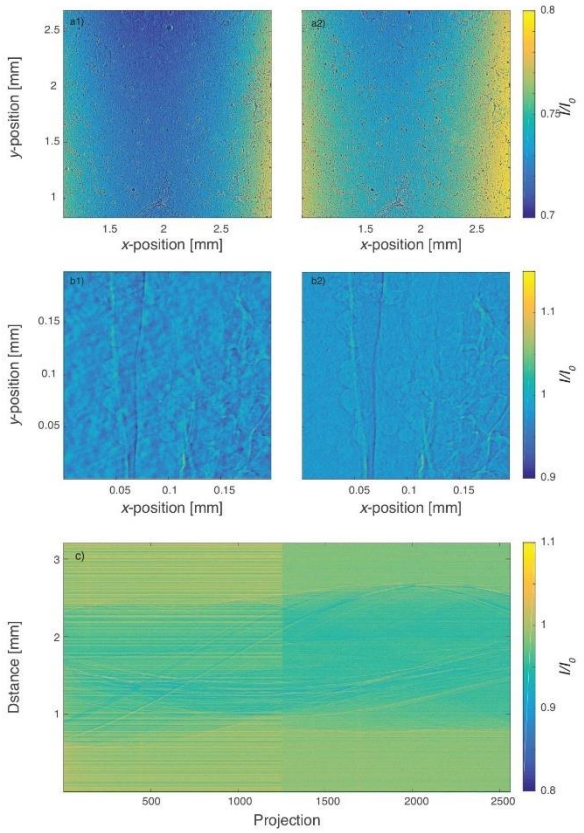

Figure 3. This figure illustrates the beneficial effect of flat-field registration on the projection quality. For the mouse brain tumour (a) most of the donut-like artifacts were removed and for the zebra fish embryo (b) flat-field registration was able to remove the dominant cloud-like artefacts, resulting in a much more detailed projection. A representative sinogram of the zebra fish embryo, given in (c), shows the improved efficiency of flat-field registration in removing all but the thinnest sinogram artefact lines. The first 1260 projections were produced using simple flat-field correction and the second 1260 projections were achieved using flat-field registration prior to the standard correction.

workstations. Therefore, we tested different registration approaches, in an effort to decrease computation time. The parameters investigated were the registration method itself, the metric, the optimizer as well as the number of registrations per radiograph. All registrations were performed using the Insight Segmentation and Registration Toolkit (ITK).[16] In terms of method, neither the affine nor the similarity registration yielded better results than the Translation registration in terms of the obtained similarity. For instance, the final rotation after Similarity registration remained below 0.001°. In terms of speed and quality the Mattes mutual information in combination with the Powell optimizer was found to be the most suitable choice. Furthermore, taking the median over a flat-field block to register to any given projection resulted in an increase of the similarity value, compared to taking a random flat-field. Additionally, the weighting of nearest flat-field blocks can increase similarity, but the optimal weighting did not necessarily correlate with the theoretical one. With the suggested parameters

one single registration took about 1 s on a workstation using six Intel(R) Xeon(R) CPU E5-2620 v3 @ 2.40GHz processors. Hence, assuming five registrations per projection to find the optimal weighting, the entire process takes about 8 h to 24 h, depending on the projection contrast, for 5120 radiographs. So far non-rigid registration has not been tested. The same holds for finding the optimally acquired flat-field as the algorithm has not been yet adapted for a cluster.

As already mentioned, registration by itself was insufficient to completely remove the ring artifacts. Thus, in a second step, we applied a frequency filter approach proposed by Mirone *et al.*[17] For every single projection the median over a user-defined number of nearest projections is calculated. Then a high frequency filter is applied to the median averaged projection. The resulting high frequency image is then finally subtracted from the registration-corrected projection.

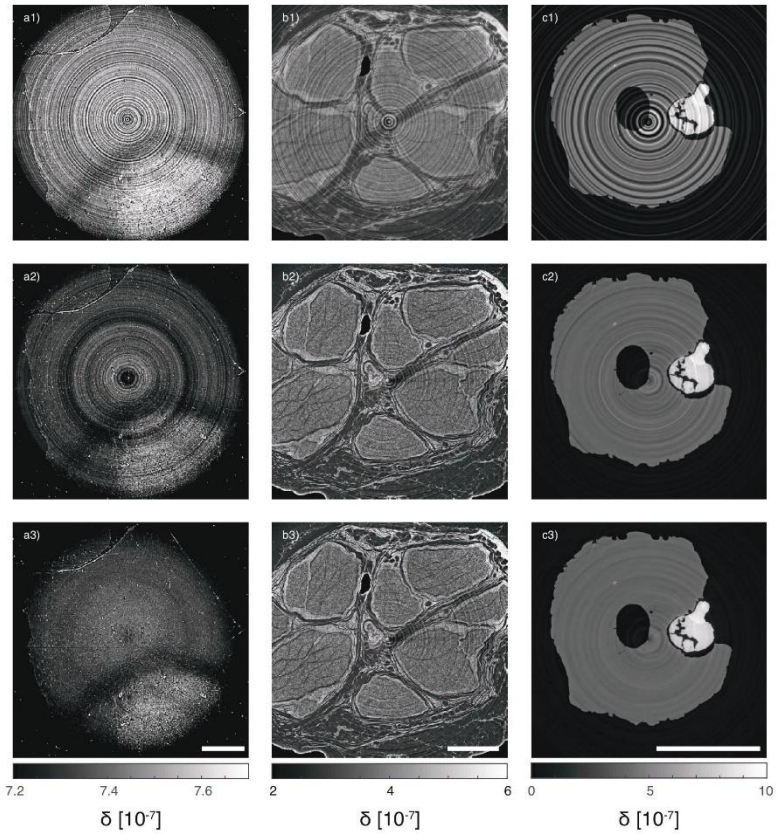

Figure 4. The effects of the ring artifact removal steps applied for (a) the mouse brain tumor, (b) the human nerve and (c) the zebra fish embryo, respectively. The top row shows representative slices for the specimens using simple flat-field correction. The middle row shows the same slices using translation registration prior to the flat-field correction and the bottom row shows the reconstructed slices obtained after the added step of high-pass filtering the flat-field corrected projections. Scale bar length is 500 μm.

Our proposed algorithm exploits the complementarity between the registration process and the high frequency filter subtraction. In detail, the former is particularly efficient for removing thicker rings caused by bigger artefacts in the projection, while the later is especially effective for removing the remaining, thinner, ring artefacts.

4. CONCLUSION

We have implemented and tested a two-step procedure for ring artefact removal, based on the combination of flat-field translation registration and high-pass filtering of projections. This approach has been proven particularly effective for the visualization of several types of low absorbing samples, even using phase tomography modalities such as single distance phase retrieval, which are generally prone to ring artefacts. The implementation is both robust and time-efficient, allowing reconstruction of up to one dataset per day on a standard workstation. The main remaining challenge is optimizing the process to decrease computation time, as well as develop a user-friendly interface to allow for processing large series of datasets required for biomedical experiments with several specimen replicates.

ACKNOWLEDGMENTS

The authors thank Prof. Michele Bernasconi and Dr. Zsofia Kovacs from the University Children's Hospital in Zurich for providing the mouse brain tumor sample. The authors also thank Gabriel Schweighauser, Jürgen Hench and Stephan Frank from the Neuropathology Department of the Basel University Hospital for providing the human peripheral nerve sample and assisting in the special preparation required for the tomography measuremts. The authors also acknowledge the support of Dr. Irene Zanette from the Diamond Light Source during beamtime.

FUNDING

The financial contribution of the Swiss National Science Foundation (Project Nos. 144535 and 147172) and NanoReg2 (European Union Horizon 2020 research agreement 646221, 15.0200-3) is gratefully acknowledged as well as the provision of beamtime at beamline ID19 under experiment number MD-860 and MD-981 from the European Synchrotron Radiation Facility (ESRF).

REFERENCES

[1] Münch, B., Trtik, P., Marone, F., and Stampanoni, M., "Stripe and ring artifact removal with combined wavelet — fourier filtering," *Opt. Express* **17**(10), 8567–8591 (2009).

[2] Sadi, F., Lee, S. Y., and Hasan, M. K., "Removal of ring artifacts in computed tomographic imaging using iterative center weighted median filter," *Comput. Biol. Med.* **40**(1), 109–118 (2010).

[3] Attwood, D. T., [*Soft X-Rays and Extreme Ultraviolet Radiation: Principles and Applications*], Cambridge University Press (1999).

[4] Momose, A., "Phase-contrast X-ray imaging based on interferometry," *J. Synchrotron Radiat.* **9**(3), 136–142 (2002).

[5] Als-Nielson, J. and McMorrow, D., [*Elements of Modern X-ray Physics (2nd Edition)*], John Wiley & Sons Ltd. (2011).

[6] Weitkamp, T., Diaz, A., David, C., Pfeiffer, F., Stampanoni, M., Cloetens, P., and Ziegler, E., "X-ray phase imaging with a grating interferometer," *Opt. Express* **13**(16), 6296–6304 (2005).

[7] Thalmann, P., Bikis, C., Hipp, A., Müller, B., Hieber, S. E., and Schulz, G., "Single and double grating-based x-ray microtomography using synchrotron radiation," *Appl. Phys. Lett.* **110**(6), 061103 (2017).

[8] Zanette, I., Lang, S., Rack, A., Dominietto, M., Langer, M., Pfeiffer, F., Weitkamp, T., and Müller, B., "Holotomography versus x-ray grating interferometry: A comparative study," *Appl. Phys. Lett.* **103**(24), 244105 (2013).

[9] Lang, S., Zanette, I., Dominietto, M., Langer, M., Rack, A., Schulz, G., Le Duc, G., David, C., Mohr, J., Pfeiffer, F., Müller, B., and Weitkamp, T., "Experimental comparison of grating- and propagation-based hard x-ray phase tomography of soft tissue," *J. Appl. Phys.* **116**(15), 154903 (2014).

[10] Paganin, D., Mayo, S. C., Gureyev, T. E., Miller, P. R., and Wilkins, S. W., "Simultaneous phase and amplitude extraction from a single defocused image of a homogeneous object," *J. Microsc.* **206**(1), 33–40 (2002).
[11] Teague, M. R., "Deterministic phase retrieval: a green's function solution," *J. Opt. Soc. Am.* **73**(11), 1434–1441 (1983).
[12] Schneider, A., Thalmann, P., Pezold, S., Hieber, S. E., and Cattin, P. C., "Augmented reality assisted brain tumor extraction in mice," *Lect. Notes Comput. Sci.* , 255–264 (2015).
[13] Sieber, S., Siegrist, S., Schwarz, S., Porta, F., Schenk, S. H., and Huwyler, J., "Immobilization of enzymes on plga sub-micrometer particles by crosslinked layer-by-layer deposition," *Macromol. Biosci.* **17**(8), 1700015 (2017).
[14] Weitkamp, T., Haas, D., Wegrzynek, D., and Rack, A., "*ANKAphase*: software for single-distance phase retrieval from inline X-ray phase-contrast radiographs," *J. Synchrotron Radiat.* **18**(4), 617–629 (2011).
[15] Kak, A. C. and Slaney, M., [*Principles of computerized tomographic imaging*], IEEE Press (1988).
[16] ITK. (2016). The Insight Segmentation and Registration Toolkit (ITK). Available online at: http://www.itk.org.
[17] Mirone, A., Brun, E., Gouillart, E., Tafforeau, P., and Kieffer, J., "The pyhst2 hybrid distributed code for high speed tomographic reconstruction with iterative reconstruction and a priori knowledge capabilities," *1st International Conference on Tomography of Materials and Structures* **324**, 41–48 (2014).

PROPAGATION-BASED X-RAY PHASE CONTRAST MICROTOMOGRAPHY OF ZEBRAFISH EMBRYOS TO UNDERSTAND DRUG DELIVERY

G. Schulz, **E. Cörek**, S. Siegrist, P. Thalmann, H. Deyhle, A. Rack, J. Huwyler, B. Müller

Journal: Microscopy and Microanalysis Volume 24, Supplement S2 (Proceedings of the 14th International Conference on X-ray Microscopy (XRM2018)), 406-407 (2018)

DOI: https://doi.org/10.1017/S1431927618014319

doi:10.1017/S1431927618014319
Microsc. Microanal. 24 (Suppl 2), 2018

Propagation-based X-ray Phase Contrast Microtomography of Zebrafish Embryos to Understand Drug Delivery

G. Schulz[1,*], E. Cörek[2], S. Siegrist[2], P. Thalmann[1], H. Deyhle[1], A. Rack[3], J. Huwyler[2], and B. Müller[1]

[1.] University of Basel, Allschwil, Switzerland.

[2.] University of Basel, Basel, Switzerland.

[3.] ESRF – The European Synchrotron, Grenoble, France.

* Corresponding author, georg.schulz@unibas.ch

The zebrafish embryo has been widely discussed as an *in vivo* screening model for nanotoxicology [1,2], mainly for studying host-pathogen interactions, innate immune responses, and inflammation. The vertebrate model is convenient because of its transparency, rapid life cycle, a high similarity of the innate immune system to humans, easy husbandry, and size, i.e. 0.5 to 0.7 mm in diameter and 5 to 7 mm long. Furthermore, no animal permission is needed up to 120 hours post fertilization. Nowadays, the investigations of the zebrafish embryos are mainly based on visible light and confocal microscopy. Nanoparticles are widely used to investigate a plethora of phenomena. For the localization of the nanoparticle distribution within the embryo, a non-destructive 3D method is beneficial. Conventional hard X-ray microtomography shows marginal contrast within soft tissues. Having a resolution below the wavelength of visible light [3], adequate contrast within soft tissues and reasonable scan times as required for imaging large numbers of specimens, single-distance phase contrast (SDPC) microtomography using ANKAphase phase retrieval [4,5] was chosen for our study.

Zebrafish embryos were euthanized 48 hours post fertilization and one hour post nanoparticle injection, fixed in 4.0 % paraformaldehyde (PFA), and dehydrated in an increasing ethanol dilution series. The dehydrated zebrafish embryo was stored in 100 % ethanol at atemperature of 4.0 °C. After air-drying, the embryo was placed into an aluminum mold channel. The mold was immersed vertically into liquid paraffin wax allowing filling with paraffin due to capillary forces. After cooling, the mold was opened and the paraffin rod containing the embedded embryo was removed. Intravenous microinjections of e.g. nanoparticles was done into the Duct of Cuvier which is a temporary circulation channel until 72 hours post fertilization. The SDPC measurements were carried out at the beamline ID19 (ESRF, Grenoble, France) with a mean photon energy of 19.6 keV at a sample-detector distance of 10 mm. For the detection, a pco.5.5 camera (PCO AG, Kelheim, Germany) with an effective pixel size of 0.3 µm was applied. Exposure time per radiograph was set to 0.1 s, resulting in a total acquisition time of around 15 minutes per height step. Using asymmetric rotation axis position, 5120 projections were recorded over 360°. Due to the field of view of 0.83 × 0.70 mm^2, four height steps were necessary to image the entire zebrafish embryo. The phase retrieval was performed in ANKAphase [4] with a δ/β ratio of 1,000. The phase projections were reconstructed using a standard filtered back-projection algorithm implemented in MATLAB R2017b (Simulink, The MathWorks, Inc., USA). For the visualization of the tomograms VGStudio MAX 2.2 (Volume Graphics GmbH, Heidelberg, Germany) was used.

The 3D rendering of the reconstructed data set in Figure 1 (a) shows zebrafish embryo anatomy. SDPC is sufficient to reveal the smallest structures e.g. the eye lens measuring around 35 µm in diameter (Figure 1 (b)). After making the soft tissue virtually transparent (Figure 1 (c)), otoliths, which are stony accretions consisting of crystalline calcium carbonate and protein in the ear of the embryo [6], could be uncovered. The otoliths are also illustrated in the selected virtual cut through the data set (Figure 1 (d)). In addition, the reconstructed slice demonstrates the high contrast of SDPC showing differences within soft tissue.

SDPC microtomography with a sub-cellular resolution allows the non-destructive visualization of paraffin-embedded zebrafish embryos without the use of any contrast agent. It detects electron density differences within the soft tissues and simultaneously visualizes soft and hard tissues (otoliths). Both spatial resolution and contrast are sufficient to investigate the 3D distribution of injected nanoparticles.

References:

[1] H Fischer *et al*. Current Opinion in Biotechnology **18** (2007), 565–571
[2] Z Clemente *et al*. Science of the Total Environment **463** (2013), 647–656
[3] A Khimchenko *et al*, Advanced Science (2018), 1700694
[4] T Weitkamp *et al*, Journal of Synchrotron Radiation **18** (2011), 617
[5] D Paganin *et al*, Journal of Microscopy **206** (2002), 33
[6] B Müller *et al*, International Journal of Materials Research **98** (2007), 613-621
[6] The project was supported by allocation of beamtime at ESRF (MD1017). The financial contribution of Swiss National Science Foundation project 144535 and R'Equip project 133802 is acknowledged.

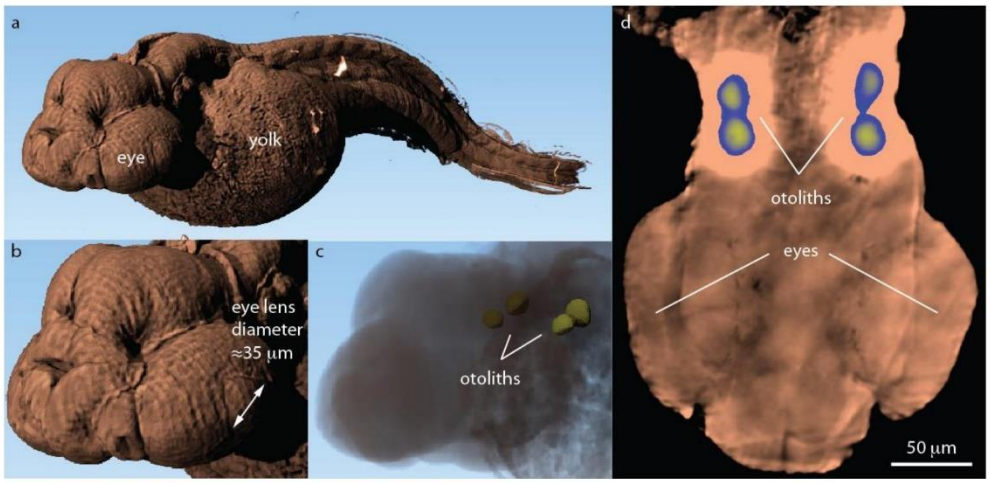

Figure. 1. 3D rendering of the entire fish embryo (a) and a zoom of the head reveal external structures of the zebra fish embryo. Transparent representation of the zoom in (c) uncovers internal features of the specimen. A selected virtual cut through the head of the specimens (d) shows the internal microstructures.

AN INTRODUCTION TO SYNCHROTRON RADIATION: TECHNIQUES AND APPLICATIONS, SECOND EDITION

Philip Willmott, PhD

Book: publisher John Wiley & Sons, 2019, page 382

DOI: https://doi.org/10.1002/9781119280453

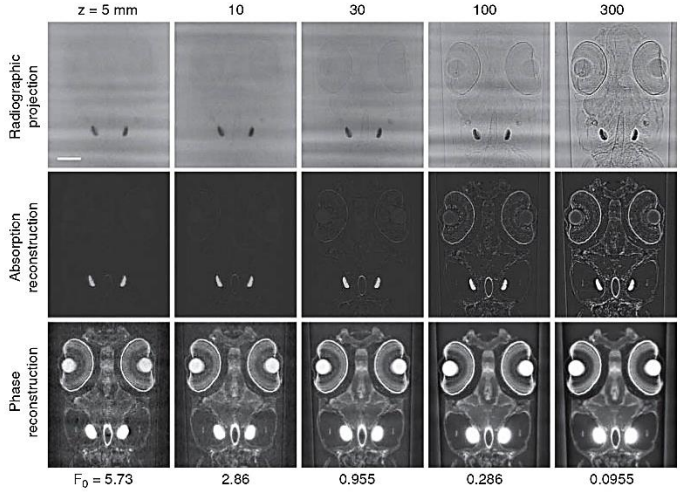

Figure 8.18 Propagation-based tomography of a zebrafish embryo recorded using 21 keV x-rays and a detector with a pixel size of $\Delta = 0.65$ μm. Zebrafish embryos are popular vertebrate models for developmental biology, toxicology, and pharmacokinetics; importantly, they exhibit good biofunctional correlations to higher vertebrates [13]. The pair of absorbing features seen in all the images are calcium carbonate-based inner-ear otoliths (Greek for 'ear stones'), which are sensitive to gravity and acceleration and are required by zebrafish for maintaining equilibrium. As the fish–detector distance z is increased, edge enhancement becomes progressively evident. At $F_0 = (2\Delta)^2/z\lambda \sim 1$, edge enhancement is clearly visible, but not so pronounced that intensity-oscillation artefacts (such as seen at 300 mm) begin to dominate. Even for very short distances, the phase shifts at the boundaries between distinct features are sufficient to produce clear phase reconstructions, in contrast to both the radiographic projections and absorption reconstructions, which can only identify the otoliths. Scale bar in top-left image = 100 μm. Courtesy Christian Schlepütz, Paul Scherrer Institute, and Jörg Huwyler and Emre Cörek, Institute of Pharmaceutical Sciences, University of Basel.

In zoom tomography, the sample is positioned a distance z_1 downstream of the focus and the detector a distance z_2 from the sample. Because the act of focussing generates a spherical-wave illumination of the sample, the propagation distance differs from the plane-wave case. The equivalent propagation distance for the magnified Fresnel image is

$$z = \frac{z_1 z_2}{z_1 + z_2}, \tag{8.12}$$

while the degree of magnification is

$$M = \frac{z_1 + z_2}{z_1}. \tag{8.13}$$

For large magnifications ($z_1 \ll z_2$), $z \approx z_1$, while for near-unity magnification ($z_1 \gg z_2$), it is approximately z_2, as in 'standard' PBT.

CHAPTER 5: DISCUSSION AND CONCLUSION

The first goal of this PhD thesis was the implementation of a hazard evaluation assessment strategy for nanoparticles in cooperation with the Swiss Centre for Applied Human Toxicology (SCAHT) and the Swiss Federal Laboratories for Materials Science and Technology (EMPA) that was part of the NanoREG II European Union's Horizon 2020 research and innovation program (Chapter 4: Results, I). To fill the gap of missing regulatory guidelines for IV applied nanoparticles for drug delivery, imaging and theranostics, "Preclinical hazard evaluation strategy for nanomedicines"[79] was written and published. Further on, as a second goal, implementation of a hybrid nanoparticle tool box was determined (Chapter 4: Results, II). A small vertebrate animal model (*Danio rerio*) was used for *in vivo* analysis of the fate of IV applied nanoparticles by imaging with various methods and comparing thereof. The main steps before the application were nanoparticle synthesis, modification, and characterization. In two beamtimes at the European Synchrotron Radiation Facility (ESRF) and Paul Scherrer Institut (PSI), nanoparticle imaging in zebrafish embryos was carried out by synchrotron radiation X-ray µCT. The results were analyzed and evaluated with 3D data visualization and analysis software to have insights into the digital 3D volume of the specimen and the nanoparticle biodistribution *in vivo* including digital histology. Finished was the thesis with experiments on magnetic manipulation of hybrid nanoparticles *in vivo* for macrophage targeting and increasing phagocytosis (Chapter 4: Results, III). Also, the possibility of controlling those nanoparticles *in vivo* was shown with electromagnetic accumulation and acoustic wave rotation.

I. IMPLEMENTATION OF A HAZARD EVALUATION STRATEGY FOR INJECTABLE NANOPARTICLES

As an introduction into the world of nanomaterials, a detailed analysis and evaluation of different nanoparticle testing strategies was done. The common approaches are trying to group nanomaterials based i.e. on their characteristics, dosimetry, functionality, and other factors[154–158]. Those concepts were not specified to certain nanoparticle types but more to specific scenarios like workplace exposure via inhalation. The purpose was to screen and make risk assessment to a broad range of nanoparticles by categorizing them into different groups or simply to be able to tell, if they are safe or not for usage. This should help to make i.e. easier predictions in the future in terms of workplace safety. For the injectable nanoparticles used in the clinics, there was no specific guideline. One of the most important issues in research is the implementation of the 3R principle for animal welfare[159]. To fulfil these criteria and improve existing guidelines, the hazard evaluation strategy for injectable nanoparticles (HES) was proposed (Chapter 4: Results, I). This approach should serve as a good alternative to existing approaches especially in terms of nanomedicines. To show the potential, a theoretical comparison between selected grouping approaches was done. This showed, that HES is testing the highest number of experimental parameters (Table 5) and is the only approach which is based on cellular uptake and cellular persistence, in case of injectable nanomedicines the most important factors. At the same time, HES is not a screening approach but uses decision pathways to minimize needed experiments. In future, this testing approach needs to be practically tested by different independent research groups and evaluated to have a statistical proof, that it is really easing up i.e. preclinical safety evaluations and helping as a basis protocol to group nanoparticles. For this goal, the

existing HES guideline can be further improved and extended to other nanoparticle types or combined with new approaches to implement a whole cascade which ideally gets the new international testing standard accepted by the regulatory authorities.

Table 5 – Comparison of the Hazard Evaluation Strategy for injectable nanoparticles (HES) with other concepts.

Parameters	QSAR-based concept	Dosimetry concept	DF4Nano concept	HES
Physicochemical properties (tier I)				
Chemical identity				X
Shape		X	X	X
Size	X	X	X	X
Aspect ratio		X	X	X
PDI		X	X	X
ζ-potential	X	X	X	X
Agglomeration size	X			
Surface area		X	X	
Surface texture		X		
pH	X			X
Solubility/Stability		X	X	X
Suspension age	X			
Contamination/Impurity			X	X
System-dependent properties (tier II)				
Exposure		X		
Biopersistence			X	
Intracellular persistence				X
Systemic uptake		X	X	
Cell specific uptake				X
Cellular effects			X	X
Concentration/Dosimetry	X	X		X
Bioactivity		X		
Biodistribution			X	
Toxic endpoints (tier III)				
Complement activation				X
Platelet aggregation				X
Hemolysis				X
Oxidative stress	X	X	X	X
Cytotoxicity	X	X	X	X
Cell viability			X	X
Phagocytosis		X	X	X
DNA damage				X
Inflammation			X	X

Comparison between the HES and three alternative hazard evaluation approaches.
The four discussed strategies use different combinations of experimental parameters, which cover physicochemical properties (tier I), system-dependent properties (tier II), and toxic endpoints (tier III).

II. DEVELOPMENT OF A HYBRID NANOPARTICLE TOOLBOX FOR *IN VIVO* EXPERIMENTS

Nanoparticles can be used for a variety of different purposes because of their broad range of properties and advantages. The selection of the most suitable nanoparticle is getting easier with the amount of publications increasing every day. One faction,

the hybrid nanoparticles, are used since years to combine different characteristics and improve the application properties i.e. for cancer treatment[160]. Instead of having two different steps for imaging and treatment, it is possible to combine those methods with the right hybrid nanoparticles to a single approach, called theranostics[161]. Usually, metal nanoparticles are used for the purpose of imaging with their dense cores coated with i.e. liposomes[162]. This has the advantage, that the coating serves as a protective layer that will stealth the nanoparticles *in vivo* from the immune system and at the same time gives a lot of possibilities to modify them i.e. by drug loading for therapy purposes[163]. SPIONs were chosen as metal cores because of their proven properties in literature as contrast agents with the ability for manipulation i.e. by magnetically direct them towards a target, and also induce hyperthermia at the target site for temperature-controlled drug release or physical therapy of tumors[164–166]. Compared to other nanoparticles, SPIONs are cheap and straight forward to synthesize, have a narrow size distribution and excellent properties such as superparamagnetism. To use them as injectables and prevent agglomeration, they need to be coated with protective layers like citric acid or in this case liposomes. In this work, a new coating method was analyzed and implemented by using microfluidics. As a result, SPIONs coated with liposomes were generated which had good physicochemical properties. This new method proved itself to be stable and served therefore as a “tool box” for a variety of modifications i.e. by pegylation with different molecular weight PEG chains from 350 to 5000 and folic acid for renal targeting by binding to the folate receptor. Disadvantages of this method could be the need of a microfluidics system (i.e. NanoAssemblr®) which needs to be bought first. For future research, this tool box can be further validated by generating new hybrid nanoparticles by modifying the coating and loading them also with different drugs for theranostic purposes.

III. CHARACTERIZATION AND *IN VIVO* EXPERIMENTS WITH HYBRID NANOPARTICLES IN A SMALL ANIMAL VERTEBRATE MODEL (*DANIO RERIO*)

Physicochemical characterization was done for every used nanoparticle in this work by the basic methods such as transmission electron microscopy, dynamic light scattering, and electrophoretic light scattering[167]. Core size, hydrodynamic size, polydispersity index (PDI), and zeta potential were determined as a qualitative control and to gather statistically solid results (Table 6, Figure 9).

Table 6 – Some physicochemical characterization results of nanoparticles used throughout of this PhD thesis. AuNP are gold nanoparticles, SPIONs are iron oxide nanoparticles coated with human serum albumin, lipoSP are hybrid nanoparticles made out of SPIONs and liposomes with the polyethyleneglycol peg chain length given in molecular weight as a number (350, 2000, 5000). All measurements were done in triplicate in water and FCS.

Engineered Nanoparticles	*Hydrodynamic diameter [nm]*	*PDI*	*Zeta potential [mV]*
AuNP	29.6 ± 0.1	0.19 ± 0.2	-29.4 ± 0.8
AuNP in FCS	94.9 ± 2.1	0.31 ± 0.5	-10.6 ± 0.9
SPIONs	61.0 ± 0.3	0.13 ± 0.01	-24.9 ± 1.0
SPIONs in FCS	60.7 ± 0.3	0.19 ± 0.02	-14.38 ± 0.9
lipoSP w/o PEG	122.3 ± 1.9	0.29 ± 0	-23.4 ± 0.8
lipoSP w/o PEG in FCS	126.5 ± 24.1	0.29 ± 0.01	-9.35 ± 0.8
lipoSP-PEG350	131.2 ± 4.5	0.21 ± 0.07	-29.6 ± 0.5
lipoSP-PEG350 in FCS	241.7 ± 88.6	0.20 ± 0.05	-34.4 ± 26.4
lipoSP-PEG2000	105.2 ± 0.7	0.30 ± 0.01	-4.0 ± 0.4
lipoSP-PEG2000 in FCS	173.1 ± 71.6	0.24 ± 0.06	-6.1 ± 0.5
lipoSP-PEG5000	122.0 ± 1.2	0.28 ± 0.01	0.4 ± 0.3
lipoSP-PEG5000 in FCS	97 ± 2.8	0.39 ± 0.03	4.6 ± 0.1

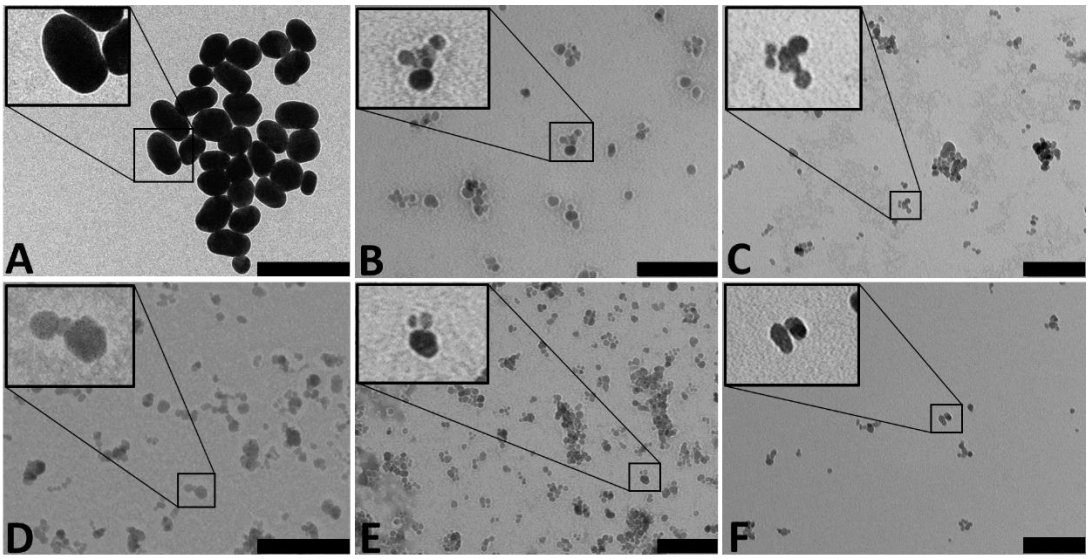

Figure 9 - Transmission electron microscope (TEM) images of ENPs. Figure 1 shows TEM images of different nanoparticles used in this work. Gold nanoparticles coated with citric acid (A), lipophilic iron oxide nanoparticles without PEG (B), lipophilic iron oxide nanoparticles with PEG 2000 (C), iron oxide nanoparticles coated with lauric acid and human serum albumin (D), lipophilic iron oxide nanoparticles with PEG 350 (E), and lipophilic iron oxide nanoparticles with PEG 5000 (F). The core of the nanoparticles is visible in black/dark grey and the surrounding lipid layer is visible as a bright hollow around the core. The nanoparticles were all synthesized as described in the Material and Methods section of this work. Scale bars = 100 nm each.

Methods such as dialysis for purification, UV-Vis for concentration determination, and multiple long-term measurements of size and PDI for long-time stability were used. Cytotoxicity measurements were conducted with different cancer and macrophage cell lines like HepG2 or THP-1 with MTT- or Alamar blue assays. Uptake was measured by flow cytometry and confocal laser scanning microscopy (CLSM) (Figure 10).

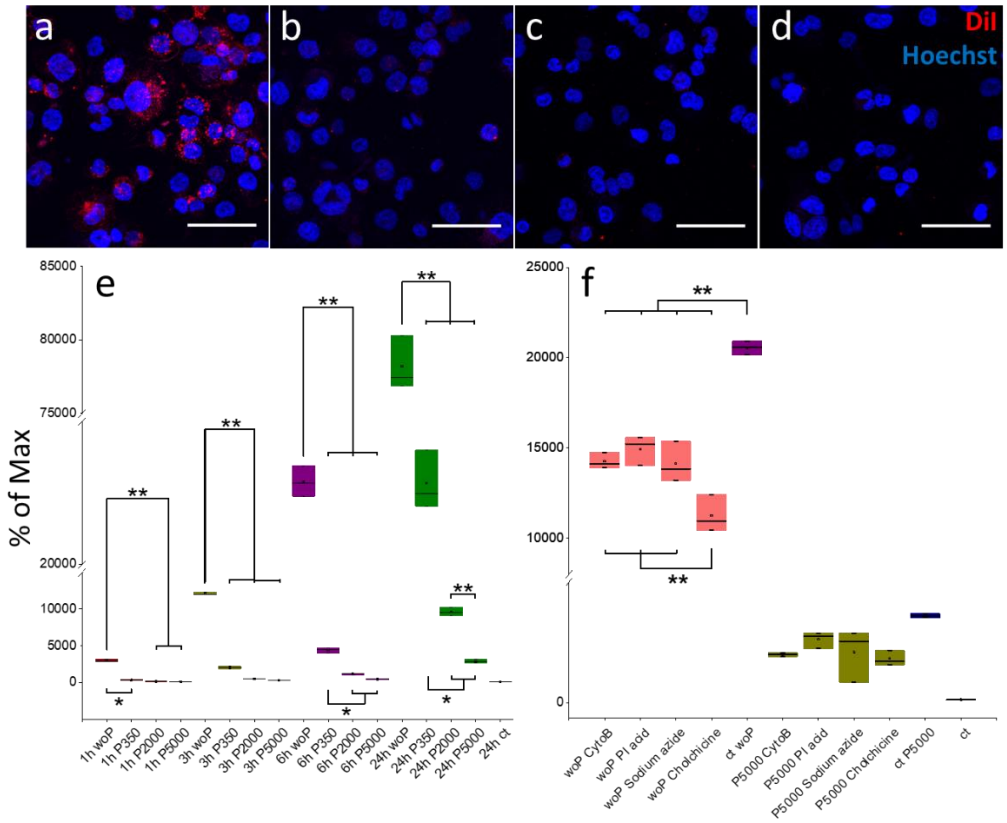

Figure 10 - CLSM uptake and FACS (inhibitory) uptake results of lipoSPIONs with THP-1 cells. Upper row shows the lipoSPIONs uptake into THP-1 cells after 3 hours by CLSM. From left to right are LipoSPIONs without PEG (a), lipoSPIONs with PEG 350 (B), lipoSPIONs with PEG 2000 (C) and lipoSPIONs with PEG 5000 (D). The fluorescent DiI lipoSPIONs are shown in red, the fluorescent Hoechst nuclei in blue. Uptake data analyzed by FACS is shown on the bottom row. Cells were incubated with lipoSPIONs without PEG, with PEG 350, PEG 2000, and PEG 5000 for 1, 3, 6 and 24 hours (e) and untreated controls. 1 hour uptake is shown in red, 3 hours uptake in yellow, 6 hours uptake in violet, and 24 hours uptake in green color and controls in black. Y-axis shows the amount of DiI positive cells. Inhibitory uptake experiments after 4 hours incubation with lipoSPIONs without PEG in pink and with lipoSPIONs with PEG 5000 in olive is shown in (f). Controls without inhibitors with lipoSPIONs without PEG is shown in violet and with lipoSPIONs with PEG 5000 in blue. Untreated controls are shown in black. Abbreviations: woP= without PEG; P350 = PEG 350; P2000= PEG 2000; P5000= PEG 5000; CytoB= Cytochalasin B; PI acid= Polyinosinic acid; ct= control. Statistically significance is given with one asterisk for p≤ 0.05 and with two asterisks for p≤ 0.01. Scale bars= 60 nanometer each.

To be able to detect the hybrid nanoparticles by fluorescence imaging, they were modified with the fluorescent dye DiI. Lower uptake was detected for pegylated nanoparticles with long molecular weight PEG chains fitting with the literature[168,169]. The nanoparticles were not cytotoxic in the used concentrations up to 180 ppm. For *in vivo* studies of those hybrid nanoparticles, zebrafish embryos (*Danio rerio*) were used as an established small vertebrate model common for toxicity, imaging, and drug delivery studies[170,171]. The results of the *in vitro* and *in vivo* studies correlated in terms of uptake and cytotoxicity imaged by light microscopy by dual injection of

Prussian blue mixed with nanoparticles. Dark-blue pigmentation showed an intact coating after a certain time probably by degradation inside macrophages. CLSM showed the co-localization of green fluorescent macrophages of the zebrafish embryo strain mpeg:kaede with the red fluorescent signal of the nanoparticles. Again, longer PEG chains lead to lower uptake after various timepoints up to 72 hours post injection which was detected by co-localization (Chapter 4: Results, II,III). Also, folic acid modified hybrid nanoparticles were used for renal targeting. First results can be seen in Figure 11. Because the access to a zebrafish strain with fluorescent renal system was not possible, no further co-localization analysis could be done. This can be repeated in the future, when access to such a strain is given.

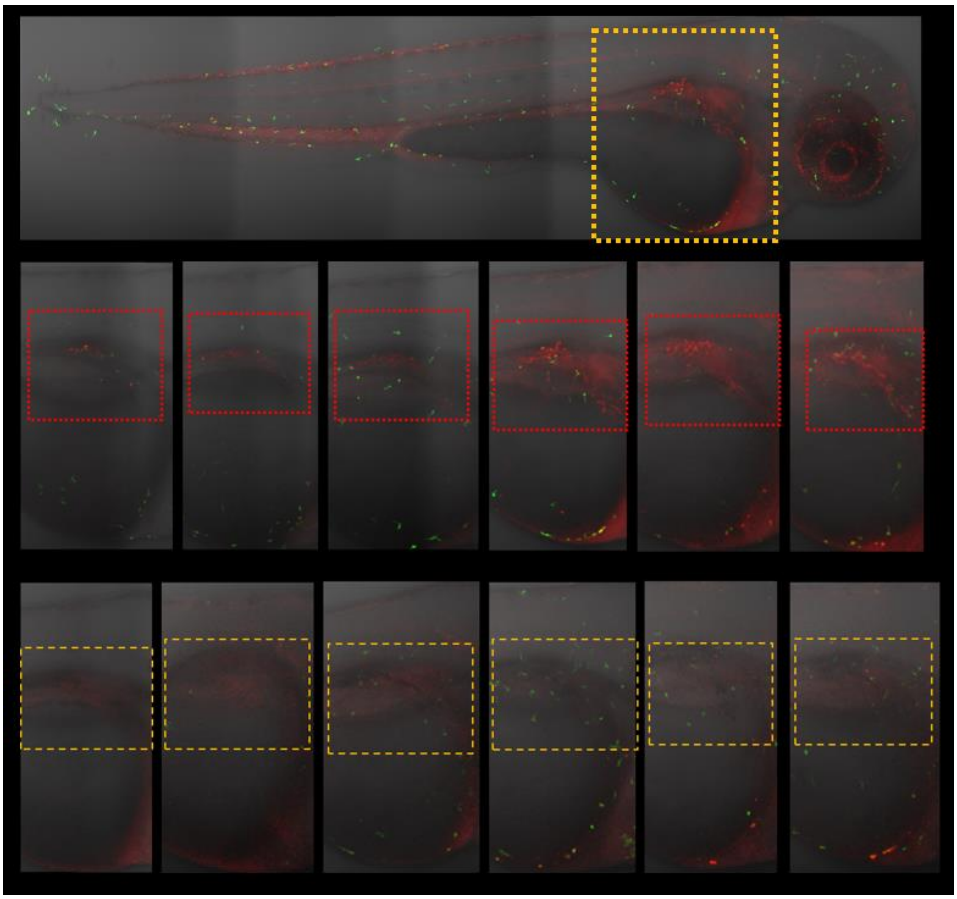

Figure 11 – Zebrafish embryo of the strain mpeg:kaede with fluorescent macrophages. Folic acid modified hybrid nanoparticles were injected into zebrafish embryos 48 hpf and analyzed by CLSM. Upper picture shows a whole zebrafish embryo with the cut out area marked in yellow dotted lines. Pictures in the middle section with the red dotted lines show embryos with injected folic acid nanoparticles with an accumulation in the renal region of the embryo. Lower images show embryos with injected control particles without folic acid with no agglomeration.

The whole results proved, that the nanoparticles are stable *in vitro* and *in vivo* and the tool box can be applied for future experiments. This was important for establishing one of the main goals in the beginning of the thesis because without this, all of the following experiments could not be done.

IV. TESTING VARIOUS IMAGING METHODS INCLUDING SYNCHROTRON X-RAY µCT

As mentioned in the earlier part, imaging with light and confocal laser scanning microscopy was possible with the hybrid nanoparticles. The idea was to have a full 3D distribution analysis of the nanoparticles *in vivo.* Although this is partly possible with CLSM (z-stacks), the z-axis resolution is not very satisfying because of the thickness of the embryos and also the nanoparticles need to be modified with fluorescent dyes. This leads to the situation that their physicochemical properties may be affected[172]. Fluorescent labeling is also not possible with nanomedicines because when particles are produced with GMP guidelines like the SPIONs coated with dextran or human serum albumine which we received from Prof. Dr. Alexiou's research group from Erlangen, the modification will not guarantee anymore the proper function. To overcome this problem, together in a collaboration with the group of Prof. Dr. Bert Müller, µCT was tested with the nanotom®m device. Detection of nanoparticles *ex vivo* was possible.

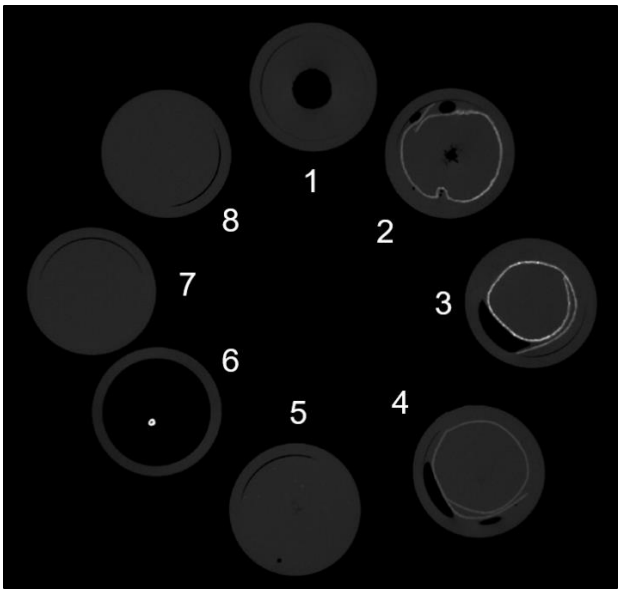

Figure 12 - Control experiments. To ensure detection of AuNP and SPIONs is possible in nanotom®m. The background is visible in black, the Eppendorf tubes in grey. White areas showing dense materials like the AuNP and SPIONs, whereby higher intensities are equal to higher densities. Eppendorf tubes containing: control with paraffin and water (1), gold nanoparticles c= 3.3 mg/ml (2), SPIONs c= 5.6 mg/ml (3), silica nanoparticles c= 20 mg/ml (4), silica nanoparticles c= 10 mg/ml (5), lyophilized gold nanoparticles (6), paraffin and filter paper (7), and paraffin (8).

Also, the imaging of zebrafish embryos was possible although with bad quality and resolution (Figure 13)[173].

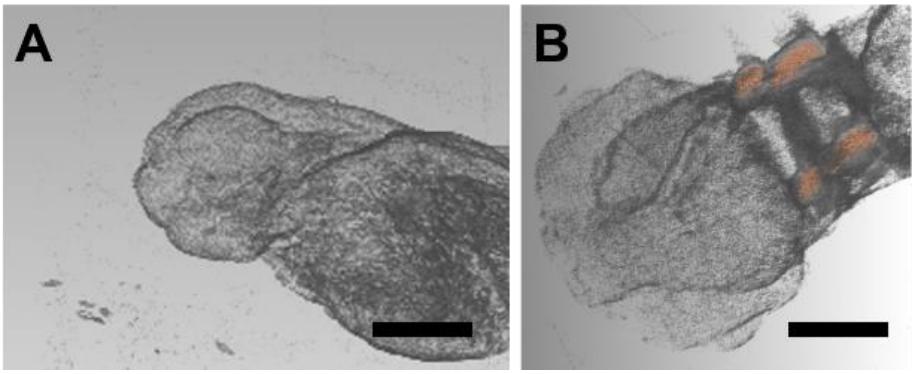

Figure 13 - µCT analysis of a 48 hpf zebrafish embryo. Nanoparticles could not be detected during trials performed with the nanotom®m. Otholits serve as orientation points (B, red structures), since zebrafish embryos did not develop any bony structures in this developmental stage. Scale bars: 100 µm (A) and 50 µm (B)

The idea to improve this situation was to use synchrotron radiation X-ray µCT with its higher X-ray flux[174]. Two beamtimes were used, ESRF and PSI. In the first round, various different nanoparticles like silica, gold and iron oxide in different concentrations were tested *in vivo* in zebrafish embryos which were *post mortem* analyzed at 24 and 48 hpi. Because of the known disadvantages of absorption contrast in soft tissue due to low contrast differences (Figure 14), phase-contrast phase retrieval imaging was used as a common method based on the refractive index[175].

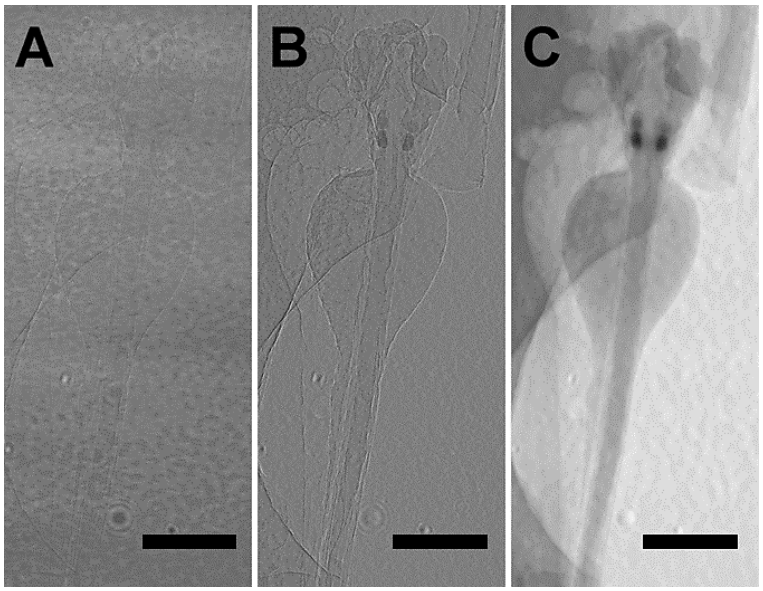

Figure 14 - Contrast differences in µCT. Uncorrected projection (A), flat- and dark-field corrected absorption contrast projection (B), and flat- and dark-field corrected phase contrast (C) images of a 96 hpf zebrafish embryo embedded in paraffin. Introducing flat- and dark-field corrections lead to the subtraction of background noise in the reconstructed projections. Absorption contrast images show higher sharpness and lower contrast. Phase contrast images show lower sharpness and higher contrast, which is more suitable for soft tissue imaging. Scale bars: 250 µm each

From the received projections of the samples, a reconstruction was done with different algorithms like the Paganin filter[176]. With help of the delta-beta value, the

contrast can be adjusted which can either be set by trial-and error or calculated depending on the experiment (Figure 15)[177].

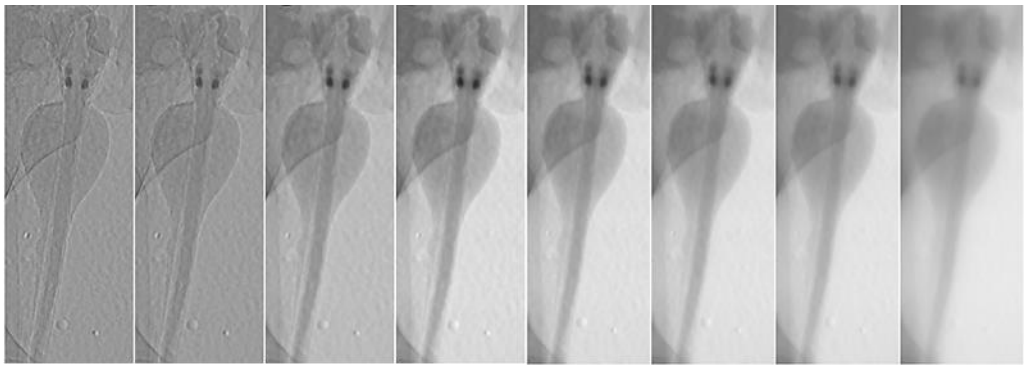

Figure 15 – Phase-contrast reconstruction phase-retrieval image of a 96 hpf zebrafish embryo with increasing delta-beta values from left to right showing the contrast change. Values are from left to right are: 100-200-300-500-800-1000-1500-2000.

The field-of-view during the imaging was not enough at 40x for the whole sample, so multiple height scans needed to be done to capture the whole embryo. After the reconstruction of all height steps, they were manually stitched together via Fiji imaging software. 3D digital volume analyses were done with reconstruction software Avizo. The results were evaluated and iron oxide nanoparticles were chosen because the other nanoparticles couldn't be detected or i.e. gold stick quickly to the injection side and showed no biodistribution. This was the successful proof-of-concept study, that detection of iron oxide nanoparticles in zebrafish embryos, which was not shown in this combination before, was possible (Figure 16).

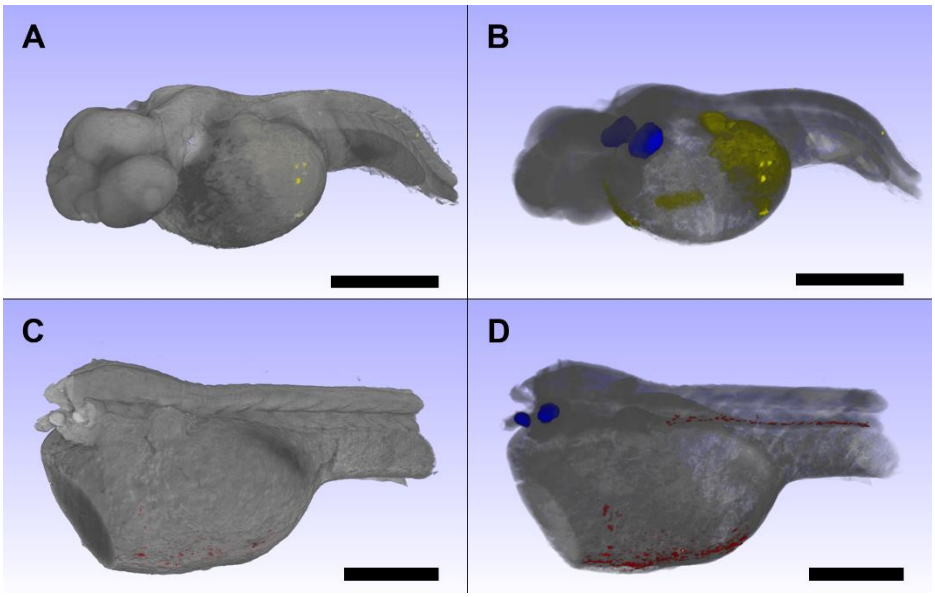

Figure 16 - 3D reconstructions of zebrafish embryos showing the biodistribution of AuNP and SPIONs. 3D reconstructions of synchrotron phase contrast projections of 1 hpi zebrafish embryos. Injections of 5 nl AuNP (c= 3.3 mg/ml, RI: 0.2) and 5 nl SPIONs (c= 5.6 mg/ml: RI: 2.93) were performed into the Duct of Cuvier (DoC). The depictions show the zebrafish embryos (grey), AuNP (yellow), SPIONs (red), and Otoliths (blue). Opaque embryos with body surface (A, C) and transparent embryos with inner structures (B, D) highlight that both ENP reside inside the specimens. AuNP adhere to the surrounding tissue of the injection side (DoC). SPIONs are found to adhere less to the same tissue. However, they are clearly visible in the areas of the anterior cardinal vein (ACV), posterior cardinal vein (PCV), and the dorsal aorta (DA). Scale bars = 100 µm (A, B); 50 µm (C, D).

For the next beamtime, PSI was chosen because of a maintenance shutdown of the ESRF. Now, only differently pegylated hybrid nanoparticles were injected at the same dose and embryos were 24 and 48 hpi post mortem fixed. Dextran and human serum albumine coated SPIONs were used as long- and short circulating controls[178–180]. It was possible to show, that there is a strong accumulation of short peg chain nanoparticles and human serum albumine coated SPIONs in the vasculature, opposite of the Dextran coated SPIONs and long chain nanoparticles that is also described in the literature[181]. It was shown, that the results (maximal intensity on the x-y axis) of CLSM and synchrotron are consistent.

Advantages of the synchrotron were:

- outrageous resolutions in all three axes,
- simultaneous analysis of nanoparticle biodistribution and histology,
- faster imaging speed,
- full digital histology qualitatively comparable to classical histology methods by slicing and staining of the fixed specimen but with the advantage of not destroying the sample which can be further used for additional experiments.

Disadvantages are difficulties to get beamtimes because of limited resources and time-consuming analysis of the results with requirement of high-end computers. Nevertheless, for the future, it is possible to further tune this whole set up i.e. for tissue biopsy analysis. If done right, computer scientists can help by automating the whole reconstruction and analysis process, so that only a mouse-click is needed after loading in the data to receive the results. Also, it is possible that with modern developments in the future, high-flux devices can be also available as compact light sources for scientists[182] (Chapter 4: Results, II).

V. MAGNETIC AND ACOUSTIC MANIPULATION OF NANOPARTICLES *IN VIVO*

One of the advantages of SPIONs is their characteristics allowing magnetic manipulation *in vivo*. By using external magnetic fields such as bar magnets, the behavior of the particles will change and this will i.e. lead to higher uptake in cells. In this work, we used an external magnetic field to increase phagocytic uptake. The long circulating hybrid nanoparticles with PEG chains of molecular weight 5000 were injected and manipulated in zebrafish embryos with help of a strong bar magnet. As

a result, the phagocytic uptake increased significantly compared to control group without magnetic manipulation. Macrophage targeting was described in the literature as a treatment method for various diseases[183]. With help of the zebrafish embryo, the hybrid nanoparticle tool box, and magnetic manipulation, those effects can be further analyzed i.e. by loading the particles with different drugs for treatment of the respective diseases like inflammation and cancer. Addiitonally, electromagnetic fields and acoustic waves were used in a further unpublished experiment, in which it was possible to agglomerate fluorescent SPIONs *in vivo* and rotate them with help of acoustic waves (Figure 17). Studies with nanorobots were already done *ex vivo*[184–186] but in an animal model, this was not shown before and opens possibilities to use i.e. nanorobots in zebrafish embryos in proof-of-concept studies in the future[187,188].

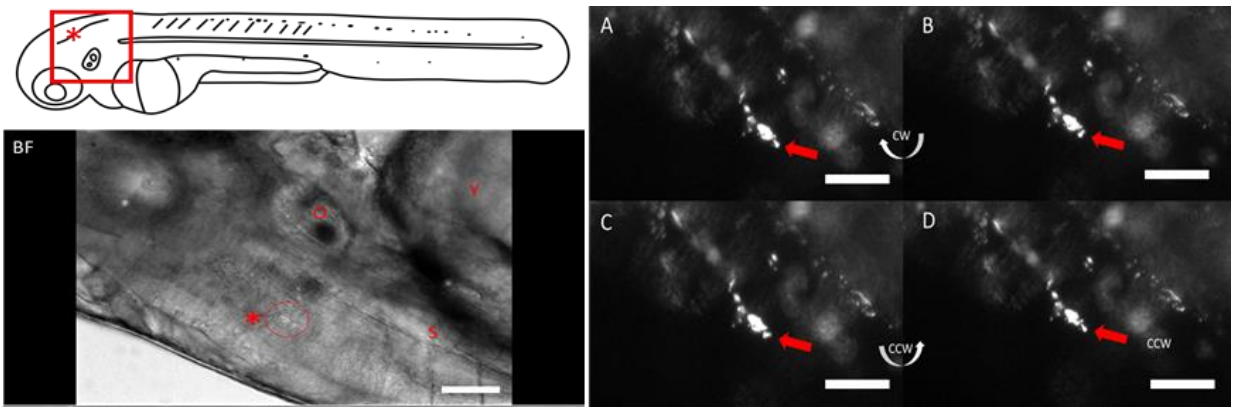

Figure 17 - Trapping and rotation of SPIONs in vivo. Schematic overview of a 50 hpf zebrafish embryo on upper image with the position of the trapped SPIONs marked with a red star. Brightfield image of the zebrafish embryo with the trapped SPIONs marked with a red star in circle (BF) with the otholits (O), spine (S), and yolk (Y). Images A to D show snapshots from the video with the trapped SPIONs marked with a red arrow (2 hpi) rotating first in the clockwise direction (from A to B) and later in the counterclockwise direction (from C to D). The trapping and rotation of the SPIONs is controlled by an electro magnet and acoustics chamber which is possible with a special addition to the confocal microscope. Scale bars 150 µm (BF), and 100 µm (A-D).

CHAPTER 6: OUTLOOK

For the future, different aspects of this thesis can be extended. Because the subject with nanoparticle safety will also be important in the future, our HES approach can be further analyzed, evaluated, and combined with new or existing approaches to further improve the outcomes. Also the hybrid nanoparticle tool box offers possibilities for many different new particles which can be created easily in laboratories as described in the methods of Chapter 4: Results, II for future research. Evaluation of the targeting possibilities *in vivo* by continuing the renal targeting with the folic acid particles can be done or new ligands or antibodies can be used i.e. for blood brain barrier targeting. Another aspect would be to continue with magnetic manipulation experiments for macrophage targeting or even electromagnetic aiming of different anatomical structures which was also not shown yet in zebrafish embryos as a model organism yet. This would fill the gap between *in vitro* experiments and *in vivo* studies in higher vertebrates. More futuristic is the idea of using nanorobots inside vertebrates for drug delivery and targeting with tremendous possibilities for what this experiment made the basis as a first proof-of-concept result.

REFERENCES

1. Faraday, M. X. The Bakerian Lecture. —Experimental relations of gold (and other metals) to light. *Philos. Trans. R. Soc. Lond.* **147**, 145–181 (1857).
2. Leonhardt, U. Invisibility cup. *Nat. Photonics* **1**, 207–208 (2007).
3. Caiger-Smith, A. *Lustre pottery: technique, tradition, and innovation in Islam and the Western world*. (Faber and Faber, 1985).
4. From Nanotech to Nanoscience. *Science History Institute* https://www.sciencehistory.org/distillations/magazine/from-nanotech-to-nanoscience (2016).
5. Knoll, M. & Ruska, E. Das Elektronenmikroskop. *Z. Für Phys.* **78**, 318–339 (1932).
6. Hawkes, P. W. *The Beginnings of Electron Microscopy*. (Academic Press, 2013).
7. Heiligtag, F. J. & Niederberger, M. The fascinating world of nanoparticle research. *Mater. Today* **16**, 262–271 (2013).
8. Hartland, A., Lead, J. R., Slaveykova, V., O'Carroll, D. & Valsami-Jones, E. The Environmental Significance of Natural Nanoparticles. *Nat. Educ. Knowl.* **4**, 7 (2013).
9. Shi, Z., Shao, L., Jones, T. P. & Lu, S. Microscopy and mineralogy of airborne particles collected during severe dust storm episodes in Beijing, China. *J. Geophys. Res. Atmospheres* **110**, (2005).
10. Fedotov, P. & Ermolin, M. Nanoparticles of volcanic ash as a carrier for toxic elements on the global scale. *EGU Gen. Assem. Conf. Abstr.* 2373 (2018).
11. Sapkota, A. *et al.* Impact of the 2002 Canadian Forest Fires on Particulate Matter Air Quality in Baltimore City. *Environ. Sci. Technol.* **39**, 24–32 (2005).
12. Buseck, P. R. & Pósfai, M. Airborne minerals and related aerosol particles: Effects on climate and the environment. *Proc. Natl. Acad. Sci.* **96**, 3372–3379 (1999).

13. Jeevanandam, J., Barhoum, A., Chan, Y. S., Dufresne, A. & Danquah, M. K. Review on nanoparticles and nanostructured materials: history, sources, toxicity and regulations. *Beilstein J. Nanotechnol.* **9**, 1050–1074 (2018).

14. Kagawa, J. Health effects of diesel exhaust emissions—a mixture of air pollutants of worldwide concern. *Toxicology* **181–182**, 349–353 (2002).

15. Ning, Z., Cheung, C. S., Fu, J., Liu, M. A. & Schnell, M. A. Experimental study of environmental tobacco smoke particles under actual indoor environment. *Sci. Total Environ.* **367**, 822–830 (2006).

16. Stefani, D., Wardman, D. & Lambert, T. The Implosion of the Calgary General Hospital: Ambient Air Quality Issues. *J. Air Waste Manag. Assoc.* **55**, 52–59 (2005).

17. Tan, M.-H., Commens, C. A., Burnett, L. & Snitch, P. J. A pilot study on the percutaneous absorption of microfine titanium dioxide from sunscreens. *Australas. J. Dermatol.* **37**, 185–187 (1996).

18. Radwan, I. M., Gitipour, A., Potter, P. M., Dionysiou, D. D. & Al-Abed, S. R. Dissolution of silver nanoparticles in colloidal consumer products: effects of particle size and capping agent. *J. Nanoparticle Res.* **21**, 155 (2019).

19. Hochella, M. F. *et al.* Natural, incidental, and engineered nanomaterials and their impacts on the Earth system. *Science* **363**, (2019).

20. ISO/TS 80004-2:2015(en), Nanotechnologies — Vocabulary — Part 2: Nano-objects. https://www.iso.org/obp/ui/#iso:std:iso:ts:80004:-2:ed-1:v1:en.

21. Khan, I., Saeed, K. & Khan, I. Nanoparticles: Properties, applications and toxicities. *Arab. J. Chem.* **12**, 908–931 (2019).

22. Caldorera-Moore, M., Guimard, N., Shi, L. & Roy, K. Designer nanoparticles: incorporating size, shape and triggered release into nanoscale drug carriers. *Expert Opin. Drug Deliv.* **7**, 479–495 (2010).

23. Bhatia, S. Nanoparticles Types, Classification, Characterization, Fabrication Methods and Drug Delivery Applications. in *Natural Polymer Drug Delivery Systems: Nanoparticles, Plants, and Algae* (ed. Bhatia, S.) 33–93 (Springer International Publishing, 2016). doi:10.1007/978-3-319-41129-3_2.

24. Hasany, S. F., Ahmed, I., J, R. & Rehman, A. Systematic Review of the Preparation Techniques of Iron Oxide Magnetic Nanoparticles. *Nanosci. Nanotechnol.* **2**, 148–158 (2012).

25. Huber, D. L. Synthesis, Properties, and Applications of Iron Nanoparticles. *Small* **1**, 482–501 (2005).

26. Cuyper, M. D. & Joniau, M. Magnetoliposomes. *Eur. Biophys. J.* **15**, 311–319 (1988).

27. Cuyper, M. D., Müller, P., Lueken, H. & Hodenius, M. Synthesis of magnetic Fe 3 O 4 particles covered with a modifiable phospholipid coat. *J. Phys. Condens. Matter* **15**, S1425 (2003).

28. Bloemen, M. *et al.* Improved functionalization of oleic acid-coated iron oxide nanoparticles for biomedical applications. *J. Nanoparticle Res.* **14**, (2012).

29. Mahmoudi, M., Sant, S., Wang, B., Laurent, S. & Sen, T. Superparamagnetic iron oxide nanoparticles (SPIONs): Development, surface modification and applications in chemotherapy. *Adv. Drug Deliv. Rev.* **63**, 24–46 (2011).

30. Freeman, M. W., Arrott, A. & Watson, J. H. L. Magnetism in Medicine. *J. Appl. Phys.* **31**, S404–S405 (1960).

31. Cunningham, C. H. *et al.* Positive contrast magnetic resonance imaging of cells labeled with magnetic nanoparticles. *Magn. Reson. Med.* **53**, 999–1005 (2005).

32. Meng, J. *et al.* LHRH-functionalized superparamagnetic iron oxide nanoparticles for breast cancer targeting and contrast enhancement in MRI. *Mater. Sci. Eng. C* **29**, 1467–1479 (2009).

33. Kim, J., Piao, Y. & Hyeon, T. Multifunctional nanostructured materials for multimodal imaging, and simultaneous imaging and therapy. *Chem. Soc. Rev.* **38**, 372–390 (2009).

34. Salaheldin, T. A. Magnetite-vitamin C nanoparticles as a potent route for treatment of iron deficiency anemia. *J. Nanomedicine Nanotechnol.* doi:10.4172/2157-7439-C1-056.

35. Schwenk, M. H. Ferumoxytol: a new intravenous iron preparation for the treatment of iron deficiency anemia in patients with chronic kidney disease. *Pharmacotherapy* **30**, 70–79 (2010).

36. Lu, M., Cohen, M. H., Rieves, D. & Pazdur, R. FDA report: Ferumoxytol for intravenous iron therapy in adult patients with chronic kidney disease. *Am. J. Hematol.* **85**, 315–319 (2010).

37. McCormack, P. L. Ferumoxytol: in iron deficiency anaemia in adults with chronic kidney disease. *Drugs* **72**, 2013–2022 (2012).

38. Anselmo, A. C. & Mitragotri, S. A Review of Clinical Translation of Inorganic Nanoparticles. *AAPS J.* **17**, 1041–1054 (2015).

39. Puri, A. *et al.* Lipid-Based Nanoparticles as Pharmaceutical Drug Carriers: From Concepts to Clinic. *Crit. Rev. Ther. Drug Carrier Syst.* **26**, 523–580 (2009).

40. Yang, F. *et al.* Advanced biomaterials for cancer immunotherapy. *Acta Pharmacol. Sin.* 1–17 (2020) doi:10.1038/s41401-020-0372-z.

41. Pottoo, F. H. *et al.* Lipid-based nanoformulations in the treatment of neurological disorders. *Drug Metab. Rev.* **0**, 1–20 (2020).

42. Shankar, R. & Pathak*, M. J. and K. Lipid Nanoparticles: A Novel Approach for Brain Targeting. *Pharmaceutical Nanotechnology* vol. 6 81–93 http://www.eurekaselect.com/162969/article (2018).

43. Forssen, E. A. & Tőkés, Z. A. Invitro and invivo studies with adriamycin liposomes. *Biochem. Biophys. Res. Commun.* **91**, 1295–1301 (1979).

44. Blum, R. H. Adriamycin: A New Anticancer Drug with Significant Clinical Activity. *Ann. Intern. Med.* **80**, 249 (1974).

45. Barenholz, Y. (Chezy). Doxil® — The first FDA-approved nano-drug: Lessons learned. *J. Controlled Release* **160**, 117–134 (2012).

46. Zucker, D., Marcus, D., Barenholz, Y. & Goldblum, A. Liposome drugs' loading efficiency: A working model based on loading conditions and drug's physicochemical properties. *J. Controlled Release* **139**, 73–80 (2009).

47. Fan, Y. & Zhang, Q. Development of liposomal formulations: From concept to clinical investigations. *Asian J. Pharm. Sci.* **8**, 81–87 (2013).

48. Carugo, D., Bottaro, E., Owen, J., Stride, E. & Nastruzzi, C. Liposome production by microfluidics: potential and limiting factors. *Sci. Rep.* **6**, 1–15 (2016).

49. Kastner, E. *et al.* High-throughput manufacturing of size-tuned liposomes by a new microfluidics method using enhanced statistical tools for characterization. *Int. J. Pharm.* **477**, 361–368 (2014).

50. Michelon, M., Oliveira, D. R. B., de Figueiredo Furtado, G., Gaziola de la Torre, L. & Cunha, R. L. High-throughput continuous production of liposomes using hydrodynamic flow-focusing microfluidic devices. *Colloids Surf. B Biointerfaces* **156**, 349–357 (2017).

51. Svenson, S. Clinical translation of nanomedicines. *Curr. Opin. Solid State Mater. Sci.* **16**, 287–294 (2012).

52. Nguyen Tri, P., Ouellet-Plamondon, C., Rtimi, S., Assadi, A. A. & Nguyen, T. A. Chapter 3 - Methods for Synthesis of Hybrid Nanoparticles. in *Noble Metal-Metal Oxide Hybrid Nanoparticles* (eds. Mohapatra, S., Nguyen, T. A. & Nguyen-Tri, P.) 51–63 (Woodhead Publishing, 2019). doi:10.1016/B978-0-12-814134-2.00003-6.

53. Toro-Cordova, A. *et al.* Liposomes Loaded with Cisplatin and Magnetic Nanoparticles: Physicochemical Characterization, Pharmacokinetics, and In-Vitro Efficacy. *Mol. J. Synth. Chem. Nat. Prod. Chem.* **23**, (2018).

54. Ye, H. *et al.* Combination of gemcitabine-containing magnetoliposome and oxaliplatin-containing magnetoliposome in breast cancer treatment: A possible mechanism with potential for clinical application. *Oncotarget* **7**, 43762–43778 (2016).

55. Zhu, L. *et al.* Targeted delivery of methotrexate to skeletal muscular tissue by thermosensitive magnetoliposomes. *Int. J. Pharm.* **370**, 136–143 (2009).

56. Qiu, D. & An, X. Controllable release from magnetoliposomes by magnetic stimulation and thermal stimulation. *Colloids Surf. B Biointerfaces* **104**, 326–329 (2013).

57. Gonzales, M. & Krishnan, K. M. Synthesis of magnetoliposomes with monodisperse iron oxide nanocrystal cores for hyperthermia. *J. Magn. Magn. Mater.* **293**, 265–270 (2005).

58. Huang, H. S. & Hainfeld, J. F. Intravenous magnetic nanoparticle cancer hyperthermia. *Int. J. Nanomedicine* **8**, 2521–2532 (2013).

59. Huang, H.-C., Barua, S., Sharma, G., Dey, S. K. & Rege, K. Inorganic nanoparticles for cancer imaging and therapy. *J. Controlled Release* **155**, 344–357 (2011).

60. Torchilin, V. P. Multifunctional, stimuli-sensitive nanoparticulate systems for drug delivery. *Nat. Rev. Drug Discov.* **13**, 813–827 (2014).

61. Nel, A., Xia, T., Mädler, L. & Li, N. Toxic Potential of Materials at the Nanolevel. *Science* **311**, 622–627 (2006).

62. Shvedova, A. A., Kagan, V. E. & Fadeel, B. Close Encounters of the Small Kind: Adverse Effects of Man-Made Materials Interfacing with the Nano-Cosmos of Biological Systems. *Annu. Rev. Pharmacol. Toxicol.* **50**, 63–88 (2010).

63. Yildirimer, L., Thanh, N. T. K., Loizidou, M. & Seifalian, A. M. Toxicology and clinical potential of nanoparticles. *Nano Today* **6**, 585–607 (2011).

64. Feliu, N. & Fadeel, B. Nanotoxicology: no small matter. *Nanoscale* **2**, 2514–2520 (2010).

65. Wolfram, J. *et al.* Safety of nanoparticles in medicine. *Curr. Drug Targets* **16**, 1671–1681 (2015).

66. Dusinska, M. *et al.* Testing strategies for the safety of nanoparticles used in medical applications. *Nanomed.* **4**, 605–607 (2009).

67. Seaton, A., Tran, L., Aitken, R. & Donaldson, K. Nanoparticles, human health hazard and regulation. *J. R. Soc. Interface* **7**, S119–S129 (2010).

68. Gebel, T. *et al.* Manufactured nanomaterials: categorization and approaches to hazard assessment. *Arch. Toxicol.* **88**, 2191–2211 (2014).

69. Mühlebach, S., Borchard, G. & Yildiz, S. Regulatory challenges and approaches to characterize nanomedicines and their follow-on similars. *Nanomed.* **10**, 659–674 (2015).

70. Scott-Fordsmand, J. J. *et al.* A unified framework for nanosafety is needed. *Nano Today* **9**, 546–549 (2014).

71. Stone, V. *et al.* ITS-NANO - Prioritising nanosafety research to develop a stakeholder driven intelligent testing strategy. *Part. Fibre Toxicol.* **11**, 9 (2014).

72. NANoREG, a common European approach to the regulatory testing of nanomaterials | RIVM. https://www.rivm.nl/documenten/nanoreg-a-common-european-approach-to-regulatory-testing-of-nanomaterials.

73. Chang, H.-I. & Yeh, M.-K. Clinical development of liposome-based drugs: formulation, characterization, and therapeutic efficacy. *Int. J. Nanomedicine* **7**, 49–60 (2012).

74. Chen, C., Han, D., Cai, C. & Tang, X. An overview of liposome lyophilization and its future potential. *J. Controlled Release* **142**, 299–311 (2010).

75. Monopoli, M. P., Åberg, C., Salvati, A. & Dawson, K. A. Biomolecular coronas provide the biological identity of nanosized materials. *Nat. Nanotechnol.* **7**, 779–786 (2012).

76. Wolfram, J. *et al.* The nano-plasma interface: Implications of the protein corona. *Colloids Surf. B Biointerfaces* **124**, 17–24 (2014).

77. Tenzer, S. *et al.* Rapid formation of plasma protein corona critically affects nanoparticle pathophysiology. *Nat. Nanotechnol.* **8**, 772–781 (2013).

78. Casals, E., Pfaller, T., Duschl, A., Oostingh, G. J. & Puntes, V. Time Evolution of the Nanoparticle Protein Corona. *ACS Nano* **4**, 3623–3632 (2010).

79. Siegrist, S. *et al.* Preclinical hazard evaluation strategy for nanomedicines. *Nanotoxicology* **13**, 73–99 (2019).

80. Hamilton, F. & Swaine, J. *An account of the fishes found in the river Ganges and its branches*. 1–426 (Hurst, Robinson, and Co., 1822). doi:10.5962/bhl.title.59540.

81. Spence, R., Gerlach, G., Lawrence, C. & Smith, C. The behaviour and ecology of the zebrafish, Danio rerio. *Biol. Rev. Camb. Philos. Soc.* (2008) doi:10.1111/j.1469-185X.2007.00030.x.

82. Engeszer, R. E., Patterson, L. B., Rao, A. A. & Parichy, D. M. Zebrafish in the wild: a review of natural history and new notes from the field. *Zebrafish* **4**, 21–40 (2007).

83. Gerhard, G. S. *et al.* Life spans and senescent phenotypes in two strains of Zebrafish (Danio rerio). *Exp. Gerontol.* **37**, 1055–1068 (2002).

84. Howe, K. *et al.* The zebrafish reference genome sequence and its relationship to the human genome. *Nature* **496**, 498–503 (2013).

85. McCluskey, B. M. & Postlethwait, J. H. Phylogeny of Zebrafish, a “Model Species,” within Danio, a “Model Genus”. *Mol. Biol. Evol.* **32**, 635–652 (2015).

86. Meyers, J. R. Zebrafish: Development of a Vertebrate Model Organism. *Curr. Protoc. Essent. Lab. Tech.* **16**, e19 (2018).

87. Fang, F. Phylogenetic Analysis of the Asian Cyprinid Genus Danio (Teleostei, Cyprinidae). *Copeia* **2003**, 714–728 (2003).

88. Van Slyke, C. E., Bradford, Y. M., Westerfield, M. & Haendel, M. A. The zebrafish anatomy and stage ontologies: representing the anatomy and development of Danio rerio. *J. Biomed. Semant.* **5**, 12 (2014).

89. Rosenthal, G. G. & Ryan, M. J. Assortative preferences for stripes in danios. *Anim. Behav.* **70**, 1063–1066 (2005).

90. Parichy, D. M. Evolution of danio pigment pattern development. *Heredity* **97**, 200–210 (2006).

91. White, R. M. *et al.* Transparent adult zebrafish as a tool for in vivo transplantation analysis. *Cell Stem Cell* **2**, 183–189 (2008).

92. Menke, A. L., Spitsbergen, J. M., Wolterbeek, A. P. M. & Woutersen, R. A. Normal Anatomy and Histology of the Adult Zebrafish. *Toxicol. Pathol.* **39**, 759–775 (2011).

93. Ellett, F. & Lieschke, G. J. Zebrafish as a model for vertebrate hematopoiesis. *Curr. Opin. Pharmacol.* **10**, 563–570 (2010).

94. Roberts, R. J. & Ellis, A. E. The Anatomy and Physiology of Teleosts. in *Fish Pathology* 17–61 (John Wiley & Sons, Ltd, 2012). doi:10.1002/9781118222942.ch2.

95. Lieschke, G. J., Oates, A. C., Crowhurst, M. O., Ward, A. C. & Layton, J. E. Morphologic and functional characterization of granulocytes and macrophages in embryonic and adult zebrafish. *Blood* **98**, 3087–3096 (2001).

96. Bennett, C. M. *et al.* Myelopoiesis in the zebrafish, Danio rerio. *Blood* **98**, 643–651 (2001).

97. Murtha, J. M., Qi, W. & Keller, E. T. Hematologic and serum biochemical values for zebrafish (Danio rerio). *Comp. Med.* **53**, 37–41 (2003).

98. Humphrey, J. D. Systemic Pathology of Fish: A Text and Atlas of Normal Tissues in Teleosts and their Response in Disease. *J. Fish Dis.* **30**, 381–382 (2007).

99. Wulliman, M. F., Rupp, B. & Reichert, H. *Neuroanatomy of the Zebrafish Brain: A Topological Atlas*. (Birkhäuser Basel, 1996). doi:10.1007/978-3-0348-8979-7.

100. Lieschke, G. J. & Currie, P. D. Animal models of human disease: zebrafish swim into view. *Nat. Rev. Genet.* **8**, 353–367 (2007).

101. *Directive 2010/63/EU of the European Parliament and of the Council of 22 September 2010 on the protection of animals used for scientific purposes Text with EEA relevance*. *276* vol. OJ L (2010).

102. Strähle, U. *et al.* Zebrafish embryos as an alternative to animal experiments—A commentary on the definition of the onset of protected life stages in animal welfare regulations. *Reprod. Toxicol.* **33**, 128–132 (2012).

103. Aleström, P. *et al.* Zebrafish: Housing and husbandry recommendations. *Lab. Anim.* 0023677219869037 (2019) doi:10.1177/0023677219869037.

104. Kimmel, C. B., Ballard, W. W., Kimmel, S. R., Ullmann, B. & Schilling, T. F. Stages of embryonic development of the zebrafish. *Dev. Dyn.* **203**, 253–310 (1995).

105. Lajis, A. F. B. A Zebrafish Embryo as an Animal Model for the Treatment of Hyperpigmentation in Cosmetic Dermatology Medicine. *Medicina (Mex.)* **54**, 35 (2018).

106. Creaser, C. W. The Technic of Handling the Zebra Fish (Brachydanio rerio) for the Production of Eggs Which Are Favorable for Embryological Research and Are Available at Any Specified Time Throughout the Year. *Copeia* **1934**, 159–161 (1934).

107. Streisinger, G., Coale, F., Taggart, C., Walker, C. & Grunwald, D. J. Clonal origins of cells in the pigmented retina of the zebrafish eye. *Dev. Biol.* **131**, 60–69 (1989).

108. Streisinger, G., Walker, C., Dower, N., Knauber, D. & Singer, F. Production of clones of homozygous diploid zebra fish (Brachydanio rerio). *Nature* **291**, 293–296 (1981).

109. Chakrabarti, S., Streisinger, G., Singer, F. & Walker, C. FREQUENCY OF γ-RAY INDUCED SPECIFIC LOCUS AND RECESSIVE LETHAL MUTATIONS IN MATURE GERM CELLS OF THE ZEBRAFISH, BRACHYDANIO RERIO. *Genetics* **103**, 109–123 (1983).

110. Kimmel, C. B. Genetics and early development of zebrafish. *Trends Genet.* **5**, 283–288 (1989).

111. Haffter, P. *et al.* Mutations affecting pigmentation and shape of the adult zebrafish. *Dev. Genes Evol.* **206**, 260–276 (1996).

112. Davidson, A. E. *et al.* Efficient gene delivery and gene expression in zebrafish using the Sleeping Beauty transposon. *Dev. Biol.* **263**, 191–202 (2003).

113. Kwan, K. M. *et al.* The Tol2kit: A multisite gateway-based construction kit for Tol2 transposon transgenesis constructs. *Dev. Dyn.* **236**, 3088–3099 (2007).

114. Ellett, F., Pase, L., Hayman, J. W., Andrianopoulos, A. & Lieschke, G. J. mpeg1 promoter transgenes direct macrophage-lineage expression in zebrafish. *Blood* **117**, e49–e56 (2011).

115. Pliss, G. B. & Khudoley, V. V. Tumor Induction by Carcinogenic Agents in Aquarium Fish. *JNCI J. Natl. Cancer Inst.* **55**, 129–136 (1975).

116. de Soysa, T. Y. *et al.* Macondo crude oil from the Deepwater Horizon oil spill disrupts specific developmental processes during zebrafish embryogenesis. *BMC Biol.* **10**, 40 (2012).

117. Sieber, S. *et al.* Zebrafish as a predictive screening model to assess macrophage clearance of liposomes in vivo. *Nanomedicine Nanotechnol. Biol. Med.* **17**, 82–93 (2019).

118. Sieber, S. *et al.* Zebrafish as a preclinical in vivo screening model for nanomedicines. *Adv. Drug Deliv. Rev.* **151–152**, 152–168 (2019).

119. Strähle, U. & Grabher, C. The zebrafish embryo as a model for assessing off-target drug effects. *Dis. Model. Mech.* **3**, 689–692 (2010).

120. Geisler, R., Köhler, A., Dickmeis, T. & Strähle, U. Archiving of zebrafish lines can reduce animal experiments in biomedical research. *EMBO Rep.* **18**, 1–2 (2017).

121. BLV, B. für L. und V. 3R – Replace, Reduce, Refine – Tierversuche ersetzen, reduzieren, verbessern. https://www.blv.admin.ch/blv/de/home/tiere/tierversuche/3r-prinzipien.html.

122. Al-Khalili, J. In retrospect: Book of Optics. *Nature* **518**, 164–165 (2015).

123. Ockenga, W. A Brief History of Light Microscopy – From the Medieval Reading Stone to Super-Resolution. (2015).

124. Robert Hooke. *Micrographia, or some physiological descriptions of minute bodies made by magnifying glasses, with observations and inquiries thereupon. By R. Hooke.* (Printed by JoMartyn, and JaAllestry, printers to the Royal Society, 1665).

125. Leeuwenhoek, A. V. More observations from Mr. Leewenhook, in a letter of Sept. 7. 1674. sent to the publisher. *Philos. Trans. R. Soc. Lond.* **9**, 178–182 (1674).

126. History of Microscopes. *Microscope.com* https://www.microscope.com/education-center/microscopes-101/history-of-microscopes.

127. Kherlopian, A. R. *et al.* A review of imaging techniques for systems biology. *BMC Syst. Biol.* **2**, 74 (2008).

128. Thorn, K. A review of imaging techniques in scientific research/clinical diagnosis. *MOJ Anat. Physiol.* **Volume 6**, (2019).

129. Thorn, K. A quick guide to light microscopy in cell biology. *Mol. Biol. Cell* **27**, 219–222 (2016).

130. Masters, B. R. Fundamentals of Light Microscopy and Electronic Imaging, Second Edition. *J. Biomed. Opt.* **18**, 029901 (2013).

131. Day, R. N. & Davidson, M. W. The fluorescent protein palette: tools for cellular imaging. *Chem. Soc. Rev.* **38**, 2887–2921 (2009).

132. Reynolds, E. S. The use of lead citrate at high pH as an electron-opaque stain in electron microscopy. *J. Cell Biol.* **17**, 208–212 (1963).

133. Gordon, R. E. Electron Microscopy: A Brief History and Review of Current Clinical Application. in *Histopathology: Methods and Protocols* (ed. Day, C. E.) 119–135 (Springer, 2014). doi:10.1007/978-1-4939-1050-2_7.

134. Tang, C. Y. & Yang, Z. Chapter 8 - Transmission Electron Microscopy (TEM). in *Membrane Characterization* (eds. Hilal, N., Ismail, A. F., Matsuura, T. & Oatley-Radcliffe, D.) 145–159 (Elsevier, 2017). doi:10.1016/B978-0-444-63776-5.00008-5.

135. Mühlfeld, C. *et al.* Visualization and quantitative analysis of nanoparticles in the respiratory tract by transmission electron microscopy. *Part. Fibre Toxicol.* **4**, 11 (2007).

136. Saghi, Z. & Midgley, P. A. Electron Tomography in the (S)TEM: From Nanoscale Morphological Analysis to 3D Atomic Imaging. *Annu. Rev. Mater. Res.* **42**, 59–79 (2012).

137. Vernon-Parry, K. D. Scanning electron microscopy: an introduction. *III-Vs Rev.* **13**, 40–44 (2000).

138. Murata, K. & Wolf, M. Cryo-electron microscopy for structural analysis of dynamic biological macromolecules. *Biochim. Biophys. Acta BBA - Gen. Subj.* **1862**, 324–334 (2018).

139. Jonkman, J. & Brown, C. M. Any Way You Slice It—A Comparison of Confocal Microscopy Techniques. *J. Biomol. Tech. JBT* **26**, 54–65 (2015).

140. Jonkman, J., Brown, C. M. & Cole, R. W. Chapter 7 - Quantitative confocal microscopy: Beyond a pretty picture. in *Methods in Cell Biology* (eds. Waters, J. C. & Wittman, T.) vol. 123 113–134 (Academic Press, 2014).

141. Flannery, B. P., Deckman, H. W., Roberge, W. G. & D'amico, K. L. Three-Dimensional X-ray Microtomography. *Science* **237**, 1439–1444 (1987).

142. Sasov, A. Y. Microtomography. *J. Microsc.* **147**, 169–178 (1987).

143. Ritman, E. L. Current Status of Developments and Applications of Micro-CT. *Annu. Rev. Biomed. Eng.* **13**, 531–552 (2011).

144. Landis, E. N. & Keane, D. T. X-ray microtomography. *Mater. Charact.* **61**, 1305–1316 (2010).

145. Cengiz, I. F., Oliveira, J. M. & Reis, R. L. Micro-CT – a digital 3D microstructural voyage into scaffolds: a systematic review of the reported methods and results. *Biomater. Res.* **22**, (2018).

146. du Plessis, A., Yadroitsev, I., Yadroitsava, I. & Le Roux, S. G. X-Ray Microcomputed Tomography in Additive Manufacturing: A Review of the Current Technology and Applications. *3D Print. Addit. Manuf.* **5**, 227–247 (2018).

147. Rahimabadi, P. S., Khodaei, M. & Koswattage, K. R. Review on applications of synchrotron-based X-ray techniques in materials characterization. *X-Ray Spectrom.* **n/a**,.

148. What is a synchrotron? https://www.esrf.eu/about/synchrotron-science/synchrotron.

149. Swiss Light Source Accelerator Facility. *Paul Scherrer Institut (PSI)* https://www.psi.ch/en/sls/accelerator.

150. What is synchrotron light? https://www.esrf.eu/about/synchrotron-science/synchrotron-light.

151. Beamlines. *Paul Scherrer Institut (PSI)* https://www.psi.ch/en/sls/beamlines.

152. Li, Y.-F. *et al.* Synchrotron radiation techniques for nanotoxicology. *Nanomedicine Nanotechnol. Biol. Med.* **11**, 1531–1549 (2015).

153. Gao, Y. *et al.* Mapping technique for biodistribution of elements in a model organism, Caenorhabditis elegans, after exposure to copper nanoparticles with microbeam synchrotron radiation X-ray fluorescence. *J. Anal. At. Spectrom.* **23**, 1121–1124 (2008).

154. Ankley, G. T. *et al.* Adverse outcome pathways: A conceptual framework to support ecotoxicology research and risk assessment. *Environ. Toxicol. Chem.* **29**, 730–741 (2010).

155. Simkó, M., Nosske, D. & Kreyling, W. G. Metrics, Dose, and Dose Concept: The Need for a Proper Dose Concept in the Risk Assessment of Nanoparticles. *Int. J. Environ. Res. Public. Health* **11**, 4026–4048 (2014).

156. Sayes, C. M., Smith, P. A. & Ivanov, I. V. A framework for grouping nanoparticles based on their measurable characteristics. *Int. J. Nanomedicine* **8**, 45–56 (2013).

157. Lynch, I., Weiss, C. & Valsami-Jones, E. A strategy for grouping of nanomaterials based on key physico-chemical descriptors as a basis for safer-by-design NMs. *Nano Today* **9**, 266–270 (2014).

158. Lamon, L., Aschberger, K., Asturiol, D., Richarz, A. & Worth, A. Grouping of nanomaterials to read-across hazard endpoints: a review. *Nanotoxicology* **13**, 100–118 (2019).

159. Kirk, R. G. W. Recovering The Principles of Humane Experimental Technique. *Sci. Technol. Hum. Values* **43**, 622–648 (2018).

160. Sailor, M. J. & Park, J.-H. Hybrid Nanoparticles for Detection and Treatment of Cancer. *Adv. Mater. Deerfield Beach Fla* **24**, 3779–3802 (2012).

161. Bohara, R. A. & Thorat, N. D. *Hybrid Nanostructures for Cancer Theranostics*. (Elsevier, 2018).

162. Kim, D. K., Mikhaylova, M., Zhang, Y. & Muhammed, M. Protective Coating of Superparamagnetic Iron Oxide Nanoparticles. *Chem. Mater.* **15**, 1617–1627 (2003).

163. Arias, L. S. *et al.* Iron Oxide Nanoparticles for Biomedical Applications: A Perspective on Synthesis, Drugs, Antimicrobial Activity, and Toxicity. *Antibiotics* **7**, (2018).

164. Usov, N. A. Iron Oxide Nanoparticles for Magnetic Hyperthermia. *SPIN* **09**, 1940001 (2019).

165. Ferreira, R. V. *et al.* Thermosensitive gemcitabine-magnetoliposomes for combined hyperthermia and chemotherapy. *Nanotechnology* **27**, 085105 (2016).

166. Bietenbeck, M., Florian, A., Faber, C., Sechtem, U. & Yilmaz, A. Remote magnetic targeting of iron oxide nanoparticles for cardiovascular diagnosis and therapeutic drug delivery: where are we now? *Int J Nanomedicine* **11**, 3191–3203 (2016).

167. Mourdikoudis, S., Pallares, R. M. & Thanh, N. T. K. Characterization techniques for nanoparticles: comparison and complementarity upon studying nanoparticle properties. *Nanoscale* **10**, 12871–12934 (2018).

168. Suk, J. S., Xu, Q., Kim, N., Hanes, J. & Ensign, L. M. PEGylation as a strategy for improving nanoparticle-based drug and gene delivery. *Adv. Drug Deliv. Rev.* **99**, 28–51 (2016).

169. Li, Y., Kröger, M. & Liu, W. K. Shape effect in cellular uptake of PEGylated nanoparticles: comparison between sphere, rod, cube and disk. *Nanoscale* **7**, 16631–16646 (2015).

170. Lee, K. J., Nallathamby, P. D., Browning, L. M., Osgood, C. J. & Xu, X.-H. N. In Vivo Imaging of Transport and Biocompatibility of Single Silver Nanoparticles in Early Development of Zebrafish Embryos. *ACS Nano* **1**, 133–143 (2007).

171. Chakraborty, C., Sharma, A. R., Sharma, G. & Lee, S.-S. Zebrafish: A complete animal model to enumerate the nanoparticle toxicity. *J. Nanobiotechnology* **14**, 65 (2016).

172. Arms, L. *et al.* Advantages and Limitations of Current Techniques for Analyzing the Biodistribution of Nanoparticles. *Front. Pharmacol.* **9**, (2018).

173. du Plessis, A., Broeckhoven, C., Guelpa, A. & le Roux, S. G. Laboratory x-ray micro-computed tomography: a user guideline for biological samples. *GigaScience* **6**, 1–11 (2017).

174. Bharti, A. & Goyal, N. Fundamental of Synchrotron Radiations. *Synchrotron Radiat. - Useful Interes. Appl.* (2019) doi:10.5772/intechopen.82202.

175. Bagnell, C. R., Zernike, J. F. & Zernike, J. F. Chapter 10 Phase Contrast Types of Specimens for Phase Contrast Historical Background of Phase Contrast. https://www.semanticscholar.org/paper/Chapter-10-Phase-Contrast-Types-of-Specimens-for-of-Bagnell-Zernike/0a9384c83be33b6d3696f59ab0ad604193ba6326.

176. Paganin, D., Mayo, S. C., Gureyev, T. E., Miller, P. R. & Wilkins, S. W. Simultaneous phase and amplitude extraction from a single defocused image of a homogeneous object. *J. Microsc.* **206**, 33–40 (2002).

177. Gureyev, T. E. *et al.* Investigation of the imaging quality of synchrotron-based phase-contrast mammographic tomography. *J. Phys. Appl. Phys.* **47**, 365401 (2014).

178. Unterweger, H. *et al.* Development and characterization of magnetic iron oxide nanoparticles with a cisplatin-bearing polymer coating for targeted drug delivery. *International Journal of Nanomedicine* https://www.dovepress.com/development-and-characterization-of-magnetic-iron-oxide-nanoparticles--peer-reviewed-fulltext-article-IJN (2014) doi:10.2147/IJN.S63433.

179. Unterweger, H. *et al.* Non-immunogenic dextran-coated superparamagnetic iron oxide nanoparticles: a biocompatible, size-tunable contrast agent for magnetic resonance imaging. *International Journal of Nanomedicine*

https://www.dovepress.com/non-immunogenic-dextran-coated-superparamagnetic-iron-oxide-nanopartic-peer-reviewed-fulltext-article-IJN (2017) doi:10.2147/IJN.S138108.

180. Zaloga, J. *et al.* Pharmaceutical formulation of HSA hybrid coated iron oxide nanoparticles for magnetic drug targeting. *Eur. J. Pharm. Biopharm.* **101**, 152–162 (2016).

181. Chiu, C.-Y., Chung, T.-W., Chen, S.-Y. & Ma, Y.-H. Effects of PEGylation on capture of dextran-coated magnetic nanoparticles in microcirculation. *Int. J. Nanomedicine* **14**, 4767–4780 (2019).

182. Schlenvoigt, H.-P. *et al.* A compact synchrotron radiation source driven by a laser-plasma wakefield accelerator. *Nat. Phys.* **4**, 130–133 (2008).

183. Hu, G. *et al.* Nanoparticles Targeting Macrophages as Potential Clinical Therapeutic Agents Against Cancer and Inflammation. *Front. Immunol.* **10**, (2019).

184. Ahmed, D. *et al.* Rotational manipulation of single cells and organisms using acoustic waves. *Nat. Commun.* **7**, 1–11 (2016).

185. Ahmed, D. *et al.* Selectively manipulable acoustic-powered microswimmers. *Sci. Rep.* **5**, 1–8 (2015).

186. Ahmed, D. *et al.* Artificial Swimmers Propelled by Acoustically Activated Flagella. *Nano Lett.* **16**, 4968–4974 (2016).

187. Dolev, S. & Narayanan, R. Towards radio transceiving in-vivo nano-robots. *SN Appl. Sci.* **1**, 969 (2019).

188. Soto, F. & Chrostowski, R. Frontiers of Medical Micro/Nanorobotics: in vivo Applications and Commercialization Perspectives Toward Clinical Uses. *Front. Bioeng. Biotechnol.* **6**, (2018).

ACKNOWLEDGMENT

I want to express my deepest gratitude to Prof. Dr. Jörg Huwyler for giving me the opportunity to start and finish my PhD thesis in his laboratories of Pharmaceutical Technology. I had a great time, learned a lot, and made a huge amount of experience during my work. Jörg was a great mentor, supervisor and motivator. I am very grateful for this period of time in my life. Thank you, Jörg!

Also, I want to thank Prof. Dr. Alex Odermatt, Head of Molecular & Systems Toxicology group, for being my second supervisor. We know each other since my time during my Master's thesis in Toxicology at the University of Basel where he was my academic supervisor. I am happy to finish now another huge part of my career and that you are part of it again.

Special thanks goes out to Prof. Dr. Gert Fricker, Director and Dean of Studies, Institute of Pharmacy and Molecular Biotechnology, Group of Pharmaceutical Technology and Pharmacology at the University of Heidelberg for being my external expert.

I also want to thank Prof. Dr. Martin Wilks, Director of Swiss Centre for Applied Human Toxicology (SCAHT) in Basel for being my chairperson during my Ph.D. exam.

Besides of that, I want to thank Susanne Schenk for taking care of our lab. It was always perfectly organized and tidy for which I am very grateful. Further thanks goes out to the whole Pharmaceutical Technology group consisting of Denise Ruoff, Darryl Borland, Stefan Winzap, Maxim Puchkov, Pascal Detampel, Tomaz Einfalt, Stefan Siegrist, Sandro Sieber, Jana Kovac, Christina Häuser, Ilona Vollrath, Anna Pratsinis, Philip Grossen, Dominik Witzigmann, Jonas Buck, Claudio Luca Alter, Jan Stephan Bolten, Patrick Hauswirth, Andreas Shittny, Maryam Farzan, Tim Dreckmann, Nina Ariane Schmidt, Joachim Schuster, Viktoria Schreiner, Leonie Wagner-Hattler, Gaby Québatte, Klara Kiene, and Daniel Kullmann.

Also, many thanks to my collaboration partners from EMPA (Dr. Peter Wick), SCAHT (Prof. Dr. Martin Wilks, Dr. Lothar Aicher, Dr. Jenny Sandström), HEPIA Genf (Prof. Dr. Luc Stoppini, Prof. Dr. Adrien Roux), Biomaterials Science Center (Prof. Dr. Bert Müller, Dr. Georg Schulz, Dr. Peter Thalmann, Dr. Cristos Bikis, Dr. Griffin Rodgers), PSI (Dr. Christian Schlepütz), and of course ETH Zürich (Prof. Dr. Daniel Ahmed).

Finally, I want to thank my parents and my little brother.
You always supported me and without you, I would not be here today.
I can be happy that you raised me with great values and showed me what is important in life.